



TECHNISCHE
UNIVERSITÄT
WIEN

DISSERTATION

Design and study of organic-inorganic hybrids as photocatalysts for energy and environmental applications

ausgeführt zum Zwecke der Erlangung des akademischen Grades eines Doktors
der Naturwissenschaften unter der Leitung von

Asst. Prof. Alexey Cherevan

und

Univ. Prof. Dominik Eder

E165

Institut für Materialchemie

eingereicht an der Technischen Universität Wien
Fakultät für Technische Chemie

von

Stephen Nagaraju Myakala

12043108



Wien, am 12, August 2024

Table of Contents

Abstract.....	iii
Zusammenfassung.....	v
Chapter 1: Introduction and background.....	1
1.1 Energy and environmental challenges	2
1.2 Fundamentals of photocatalysis.....	4
1.3 Hybrid photosystems	7
1.3.1 Overview	7
1.3.2 Organic-inorganic hybrids (OIHs)	9
1.3.3 Organic-inorganic architectures (OIAs).....	10
Motivation and aims	13
Chapter 2: Methods and instrumentation.....	15
2.1 X-ray diffraction.....	15
2.2 Optical spectroscopy.....	16
2.2.1 UV-Vis spectroscopy	16
2.2.2 Diffuse reflectance spectroscopy	16
2.2.3 Photoluminescence spectroscopy	17
2.3 Thermogravimetric analysis	17
2.4 Total X-ray fluorescence spectroscopy.....	18
2.5 Electron microscopy.....	18
2.5.1 Scanning electron microscopy (SEM).....	18
2.5.2 Transmission electron microscopy (TEM).....	19
2.6 Raman spectroscopy	19
2.7 Attenuated total reflection Fourier transform infrared spectroscopy	19
2.8 X-ray photoelectron spectroscopy.....	20
Chapter 3: Ti-based MOFs as OIH photosystems for visible-light-driven water remediation ..	21
3.1 Introduction	22
3.2 Results and discussion	23
3.2.1 Structural and optoelectronic characterization	23
3.2.2 Adsorption studies	25
3.2.3 Photocatalytic degradation results	27
3.2.4 Photocatalytic degradation mechanism study	29
3.2.5 Stability and reusability	31
3.3 Conclusion.....	32
3.4 Experimental section.....	32
Chapter 4: MOCHAs: Ag-based OIHs as co-catalysts for photocatalytic H ₂ production	36
4.1 Introduction.....	37

4.2 Results and discussion	38
4.2.1 Structure and optoelectronic properties	38
4.2.2 Photocatalytic performance of MOCHA as a quasi-homogeneous photosystem...40	40
4.2.3 Photocatalytic performance of MOCHAs as a heterogenized photosystem	44
4.3 Conclusion	50
4.4 Experimental section.....	50
Chapter 5: TiO ₂ -based OIA: spherogels for photocatalytic H ₂ production.....	54
5.1 Introduction	55
5.2 Results and discussion	56
5.2.1 Structural and chemical characterization	56
5.2.2 Photocatalytic hydrogen evolution	60
5.3 Conclusion	62
5.4 Experimental section.....	63
Chapter 6: NiO-based OIAs: Dye sensitized photocathodes for photoelectrocatalytic H ₂ production.....	65
6.1 Introduction	66
6.2 Results and discussion	69
6.2.1 Photocathode optimization	69
6.2.2 Electrodeposition optimization and PEC tests.....	73
6.3 Conclusion	74
6.4 Experimental section.....	75
Chapter 7: Conclusions and outlook	77
References.....	81
Appendix	91
List of publications.....	93
Curriculum vitae	95
Acknowledgements	98

Abstract

The two global sustainability challenges of providing clean water and clean fuels are in dire need for alternative solutions to our current approaches and systems. Harnessing solar energy to convert unwanted chemicals and pollutants into useful, valuable products via photocatalytically driven chemical reactions is an excellent strategy to tackle both these problems. Therefore, photocatalytic materials that can degrade water pollutants and also produce clean H₂ fuel via water splitting, are attractive candidates. However, most photocatalyst materials, either organic or inorganic in nature, often suffer from several major drawbacks such as chemical instability, inefficient sunlight absorption, or poor catalytic reaction rates. Hybrid photocatalysts combining both organic and inorganic components provide complementary strengths to each other resulting in a chemically and structurally stable photocatalyst with improved optoelectronic properties and excellent photocatalytic performance. The aim of this thesis is to demonstrate representative examples of such hybrid photosystems as efficient photocatalytic systems for wastewater treatment and H₂ production.

The first example explores metal-organic frameworks – a class of materials that combine metal-oxygen inorganic clusters and organic linker molecules to form a 3-dimensional framework. Herein, we study a specific Ti-MOF called COK-47 for its potential as a visible light driven photocatalyst for dye degradation. We show its selective and fast photodegradation ability with high catalytic rates which are on par with some of the other widely studied Ti-based photocatalysts. We demonstrate the important role of the surface charge as the driving force behind its selective adsorption and show that O₂^{•-} radicals are the major reactive oxygen species responsible for dye degradation.

The second example introduces a set of Ag-based MOCHAs – a class of metal-organic-chalcogen hybrids – as photocatalysts for the hydrogen evolution reaction. Herein, we study a set of AgXC₆H₅ (X standing for S, Se, and Te chalcogens) MOCHAs and explore two photosensitization strategies, namely relying on inorganic TiO₂ and molecular [Ru(bpy)₃]²⁺. The study shows that while the AgSeC₆H₅ MOCHA gives the best performance across all photosystems, the activity of the remaining two MOCHAs, AgSC₆H₅ and AgTeC₆H₅, depends on the photosensitizer involved. Finally, we show that photocatalyst stability and reusability under turnover conditions is strongly correlated to the sensitization approach.

The third example studies a representative core-shell hybrid architecture made from inorganic TiO₂ (core) and carbon (shell) towards the photocatalytic hydrogen evolution reaction. Herein, we prepare a set of these hybrids with different carbon-to-TiO₂ ratios using a novel synthetic approach and explore their structural evolution as a function of post-synthetic modification. Based on our photocatalytic studies, we show the advantage of a homogenous interfacial contact between the core and shell for efficient charge transfer, while also revealing the importance of the surface morphology and porosity of the shell by controlling the mass diffusion of the reactant molecules.

The fourth example describes the development of a hybrid photocathode prepared by combining inorganic NiO, organic light absorbing dye molecules, and a molybdenum sulphide-based catalyst (MoS_x). We demonstrate the importance of the dye choice, loading and anchoring strategy on the ultimate photoresponse. Our results also show that the electrodeposition of MoS_x catalyst onto the NiO/dye architecture results in the most efficient and stable hybrid photosystem producing H₂ for over the span of few hours.

These results document that various hybrid photosystems can be developed to efficiently harness solar energy. Each of these examples not only provides insights into the advantages and working mechanisms of hybrid materials but also provides a glimpse into the challenges involved in preparing and optimizing inorganic-organic hybrid photosystems.

Zusammenfassung

Die beiden globalen Nachhaltigkeits Herausforderungen, sauberes Wasser und saubere Kraftstoffe bereitzustellen, erfordern dringend alternative Lösungen zu unseren derzeitigen Ansätzen und Systemen. Die Nutzung von Sonnenenergie zur Umwandlung unerwünschter Chemikalien und Schadstoffe in nützliche, wertvolle Produkte durch photokatalytisch angetriebene chemische Reaktionen ist eine hervorragende Strategie zur Bewältigung dieser beiden Probleme. Daher sind photokatalytische Materialien, die Wasserschadstoffe abbauen und durch Wasserspaltung auch sauberen H_2 -Kraftstoff produzieren können, attraktive Kandidaten. Die meisten Photokatalysatormaterialien, ob organischer oder anorganischer Natur, weisen jedoch häufig mehrere schwerwiegende Nachteile auf, wie chemische Instabilität, ineffiziente Sonnenlichtabsorption oder schlechte katalytische Reaktionsraten. Hybride Photokatalysatoren, die sowohl organische als auch anorganische Komponenten kombinieren, bieten einander ergänzende Stärken, was zu einem chemisch und strukturell stabilen Photokatalysator mit verbesserten optoelektronischen Eigenschaften und hervorragender photokatalytischer Leistung führt. Ziel der Arbeit ist es, repräsentative Beispiele solcher hybriden Photosysteme als effiziente photokatalytische Systeme für die Abwasserbehandlung und H_2 -Produktion aufzuzeigen.

Das erste Beispiel untersucht metallorganische Gerüstverbindungen – eine Klasse von Materialien, die anorganische Metall-Sauerstoff-Cluster und organische Linkermoleküle zu einem dreidimensionalen Gerüst kombinieren. Hier untersuchen wir ein spezielles Ti-MOF namens COK-47 auf sein Potenzial als Photokatalysator für den Farbstoffabbau. Wir zeigen seine selektive und schnelle Photoabbaufähigkeit mit hohen katalytischen Raten, die mit denen einiger anderer umfassend untersuchter Ti-basierter Photokatalysatoren vergleichbar sind. Wir demonstrieren die wichtige Rolle der Oberflächenladung als treibende Kraft hinter ihrer selektiven Adsorption und zeigen, dass $O_2^{\cdot-}$ -Radikale die wichtigsten reaktiven Sauerstoffspezies sind, die für den Farbstoffabbau verantwortlich sind.

Das zweite Beispiel stellt eine Reihe von Ag-basierten MOCHAs – eine Klasse von Metall-Organik-Chalkogen-Hybriden – als Photokatalysatoren für die Wasserstoffentwicklungsreaktion vor. Hier untersuchen wir eine Reihe von $AgXC_6H_5$ -MOCHAs (X steht für S-, Se- und Te-Chalkogene) und erforschen zwei Photosensibilisierungsstrategien, nämlich auf der Basis von anorganischem TiO_2 und molekularem $[Ru(bpy)_3]^{2+}$. Die Studie zeigt, dass $AgSeC_6H_5$ -MOCHA zwar die beste Leistung über alle Photosysteme hinweg bietet, die Aktivität der beiden verbleibenden MOCHAs, $AgSC_6H_5$ und $AgTeC_6H_5$, jedoch vom verwendeten Photosensibilisator abhängt. Schließlich zeigen wir, dass die Stabilität und Wiederverwendbarkeit des Photokatalysators unter Reaktionsbedingungen stark mit dem Sensibilisierungsansatz korreliert.

Das dritte Beispiel untersucht eine repräsentative Kern-Schale-Hybridarchitektur aus anorganischem TiO_2 (Kern) und Kohlenstoff (Schale) für die photokatalytische Wasserstoffentwicklungsreaktion. Hier stellen wir eine Reihe dieser Hybride mit unterschiedlichen Kohlenstoff- TiO_2 -Verhältnissen unter Verwendung eines neuartigen synthetischen Ansatzes her und erforschen ihre strukturelle Entwicklung als Funktion der postsynthetischen Modifikation. Basierend auf unseren photokatalytischen Studien zeigen wir den Vorteil eines homogenen Grenzflächenkontakts zwischen Kern und Schale für eine effiziente Ladungsübertragung und enthüllen gleichzeitig die Bedeutung der Oberflächenmorphologie und Porosität der Schale durch Kontrolle der Massendiffusion der Reaktantenmoleküle.

Das vierte Beispiel beschreibt die Entwicklung einer Hybrid-Photokathode, die durch die Kombination von anorganischem NiO, organischen lichtabsorbierenden Farbstoffmolekülen und einem Katalysator auf Molybdänsulfidbasis (MoS_x) hergestellt wird. Wir demonstrieren die Bedeutung der Farbstoffauswahl, der Beladung und der Verankerungsstrategie für die endgültige Photoreaktion. Unsere Ergebnisse zeigen auch, dass die galvanische Abscheidung des MoS_x -Katalysators auf der NiO/Farbstoffarchitektur zum effizientesten und stabilsten Hybrid-Photosystem führt, das über einen Zeitraum von einigen Stunden H_2 produziert.

Diese Ergebnisse dokumentieren, dass verschiedene Hybrid-Photosysteme entwickelt werden können, um Sonnenenergie effizient zu nutzen. Jedes dieser Beispiele bietet nicht nur Einblicke in die Vorteile und Arbeitsmechanismen von Hybridmaterialien, sondern auch einen Einblick in die Herausforderungen bei der Herstellung und Optimierung anorganisch-organischer Hybrid-Photosysteme.

Chapter 1: Introduction and background

This chapter is intended to provide the reader with an overview of the current major challenges in the worlds' energy and environmental sectors and the importance of finding an economical solution to tackle them. Following this, it describes the motivation behind the research carried out and presented in this thesis, beginning with an introduction of the advantages and feasibility of photocatalysis, documenting that using sunlight and cheap materials can be an attractive solution. Furthermore, it gives a general synopsis of the key processes involved and emphasizes the idea of designing hybrid materials to obtain best performance. The chapter thereby introduces four different approaches of preparing these hybrid materials and photosystems, with a short overview and their advantages. Finally, it provides a brief introduction of the four distinct hybrids prepared and studied in this thesis for their application in photocatalytic wastewater treatment and solar fuel generation.

1.1 Energy and environmental challenges

In today's global landscape, we are currently faced with two major challenges:

1. The increasing demand and thereby a lack of adequate amounts of clean water across the globe,¹ and
2. The ever-increasing energy demand – for the purposes of electricity generation, heat production (domestic and industrial), and transportation.

Both these issues can be tracked back to high population growth rates, especially in developing countries; and finding solutions to these challenges is key to prosperity and sustenance. The world population has more than doubled since the 1950s and is projected to additionally increase by 40% until 2050. Population growth, at such a high rate, coupled with economic development has led to a 600 % increase in global water needs over the past century, resulting in severe water scarcity with over 2 billion people lacking access to clean water.² This scarcity is further exacerbated by the diminishing water resources and declining water quality, predominantly due to industrial water pollution. Globally, almost 80% of polluted freshwater is released back into natural sources, deteriorating the freshwater quality, and having numerous harmful effects on the environment.³ According to the World Resources Institute (WRI), over 20% of the total polluted freshwater is released from textile dyeing. If this wastewater could be recycled and freed from dye effluents, it could help support the water demands especially in our agricultural sector, which accounts for the largest demand (70%) of our total water needs. Several studies have been performed to develop efficient methods for the removal of textile effluents, specifically targeting dyestuffs and other chemicals.⁴⁻⁶ For example, adsorption, ultrafiltration, reverse osmosis, and advanced oxidation processes (AOPs) like ozonation or Fenton oxidation are few of the many strategies employed for wastewater treatment that can then be reused for agricultural irrigation.⁷⁻¹¹ In addition to the high demand for water in the agricultural sector, more recently, industrial and domestic sector water demands have also grown at a much higher rate. In 2012, the world energy outlook report, for the first time reported a strong interdependence between the global energy and water sector. The industrial sector accounted for over 20% of the total water use, of which 75% was used by the energy production sector for power generation, extraction, transportation, and processing, while the rest was used in manufacturing processes.¹² Table 1.1 shows the different steps in the energy production that need water along with some of the impacts the discarded water has on the environment.¹² Therefore, wastewater treatment to safeguard sustainable water resources is not only an

Table 1.1 Key uses of water for energy production and potential impact on water quality¹²

	Water demand	Impact on water quality
Primary energy production		
Oil and gas	<ul style="list-style-type: none"> • Drilling and hydraulic fracturing • Upgrading and refining into products 	Contamination by seepage, fracturing fluids and flowback into groundwater
Coal	<ul style="list-style-type: none"> • Cutting and dust suppression in mining and hauling • Washing to improve coal quality • Long distance travel via coal slurry 	Contamination by mine drainage or produced water into surface or groundwater
Biofuels	<ul style="list-style-type: none"> • Irrigation for feedstock crop growth • Wet milling, washing, and cooling in the conversion process 	Contamination by fertilizers pesticides, and sediments
Power generation		
Thermal (Fossil, nuclear, bioenergy)	<ul style="list-style-type: none"> • Boiler feed for generating steam • Cooling for steam condensing 	Thermal pollution by cooling water discharge; Discharge of boiler feed with suspended pollutants
Hydropower	<ul style="list-style-type: none"> • Electricity generation 	Alteration of water temperatures

important step in alleviating our water demands but also a necessary step to support the energy production sector - which is also transforming and currently tackling major energy shortages and its adverse effects.

According to the International Energy Agency (IEA), the global energy consumption has tripled over the past 5 decades and is predicted to double in the coming 30 years. Such an energy demand has led the current system to heavily rely on, and overuse fossil fuels which produce over 85% of total energy needs. This overreliance has led to two major concerns – first, fossil fuels are finite resources and therefore unsustainable; and second, they produce a large amount of CO₂ emissions as a combustion byproduct, which, among other greenhouse gases has been a major leading cause for the temperatures rising globally - resulting in catastrophic natural calamities like floods, droughts, heat waves, etc. To offset this overuse, the United Nations (UN) introduced SDG 7 with a goal to substantially increase the renewable energy production share in the energy sector by 2030, thereby reducing the use of fossil fuels and limiting the global temperature rise to 1.5 °C compared to preindustrial levels as per the Paris agreement set in 2015.¹³ At present, practical renewable sources of energy typically include solar, wind, biomass, and geothermal energy with a total contribution of ~8% to the overall energy sector as of 2021.¹⁴ Among these, solar energy is the most attractive since it is abundant, cheap, and provides the cleanest pathway to renewable energy; because energy production from biomass and geothermal sources still risk producing significant amounts of greenhouse gas emissions. As of 2023, solar photovoltaics (PV) – converting solar energy to electricity – are the leading and only renewable energy method predicted to successfully achieve the goal of Net Zero Emissions (NZE) by 2050.¹⁵

While each of the renewable sources have their advantages, they are often only able to provide large amounts of energy intermittently with a significant amount of downtime. Therefore, all of the excess energy produced needs to have an efficient storage solution, which can later be used – as a secondary energy source – in the absence of the renewable source. Additionally, storing the excess energy also provides a great way to transport the energy to geographical locations with limited access to the renewable sources like the sunlight or wind. Drawing inspiration from fossil fuels, which have stored energy for centuries, in the form of chemical bonds (like hydrocarbons), that is then extracted whenever required by breaking these bonds is an excellent example for long term energy storage. However, developing systems and materials for converting solar or wind energy into hydrocarbons is firstly an extremely difficult task, and secondly only feasible in a carbon neutral economy – where the CO₂ produced from combustion is catalytically reduced back to hydrocarbon fuels. However, the added burden of capturing gaseous CO₂ acts as a major barrier towards achieving this goal. Alternatively, molecular hydrogen (H₂) is an attractive solution because unlike CO₂, it is light, non-toxic, has an abundance of sources like oceanic water, and most importantly, has the highest gravimetric energy density (~120 MJ/Kg) – almost thrice the capacity of traditional hydrocarbon fuels. Moreover, since its combustion only produces water as a byproduct which can be reused as a source for H₂ (via water splitting), it can be considered a sustainable and clean fuel. Lastly, H₂ is also used in other sectors like ammonia synthesis, steel and cement manufacturing, CO₂ reduction reaction, etc. Based on these factors, industrial production of H₂ is needed, not just for energy storage but also as a secondary energy source and has been carried out using steam methane reforming (SMR) since the 1930s.¹⁶ However, this process produces significant CO₂ emissions, currently accounting for ~3% of the global emissions, thereby producing H₂ categorized as grey hydrogen. PV panels, when coupled with efficient electrolyzer cells used for splitting water, can harness and store large amounts of solar energy

in H₂ bonds; such H₂ is categorized as green hydrogen. Unfortunately, the high production costs and challenges associated with the longevity makes PV panels economically unsustainable.¹⁷ On the other hand, photocatalysis, using solar energy to drive a chemical reaction, is a stronger alternative since it can directly use sunlight for splitting water into its individual components, producing green H₂. Furthermore, this approach can also be used to drive oxidative chemical reactions (in water) that produce reactive oxygen species (ROS) like, OH[•], O₂^{•-}, etc., leading to the degradation of pollutants (e.g. dye effluents) for industrial wastewater treatment. Consequently, photocatalysis or photocatalyst materials can provide a multifaceted solution to two of our major problems we currently face in the world.

In order to design and optimize materials that can efficiently use solar energy, it is crucial to understand the fundamental properties of a photocatalytic reaction process. The following section describes each of the fundamental processes leading to a successful photocatalytically driven reaction, and also summarizes some of the key characteristics for the materials widely used for photocatalysis.

1.2 Fundamentals of photocatalysis

Photocatalysis can be defined as the process where light energy (“Photo-”) is used to accelerate (“-catalysis”) an energetically favorable chemical reaction ($\Delta G < 0$). On the other hand, photosynthesis would aptly describe a process utilizing light energy to drive an energetically unfavorable reaction (like water splitting, $\Delta G > 0$), usually to produce desirable products (H₂/O₂). However, due to a widespread generalization within the community, the term “photosynthesis” is often used interchangeably with “photocatalysis” when referring to the general concept of “light energy being used to accelerate a chemical reaction”. Therefore, since many reference studies and examples mentioned throughout this thesis also use the terms equivalently, I will continue to use “photocatalysis” to refer to both the processes.

Deriving from before, a “photocatalyst” is therefore a material which can efficiently absorb light and convert it to charge carriers (electrons/holes) which then take part in a desired chemical reaction. While the final chemical reaction occurs at the interface between the material and surroundings (solid-gas or solid-liquid), three key processes occur prior to this, predominantly in the bulk of the material: first, light absorption resulting in the generation of an excited electron-hole pair (charge generation), followed by charge separation and migration, and lastly the charges are consumed, in which the electrons and holes are used for redox reactions respectively, as shown in Scheme 1.1. The ability to efficiently carry out each of these steps by a photocatalyst is determined by its characteristic optical, electronic, and structural features, as discussed below.

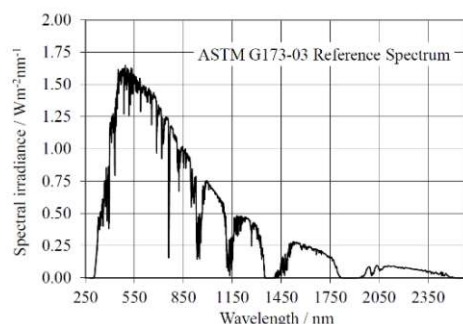
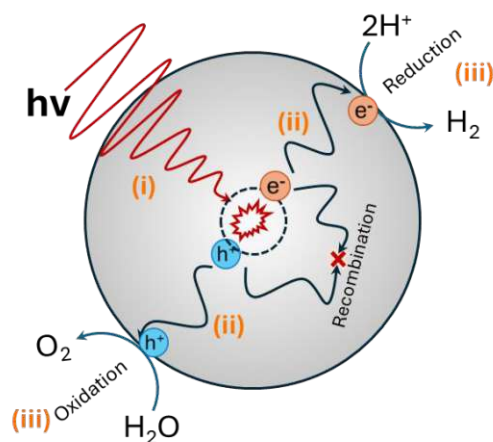


Figure 1.1 Solar light distribution at the sea level using ASTM G173-03 reference spectra derived from the Simple Model of the Atmospheric Radiative Transfer of Sunshine, SMARTS.

1. Light absorption and band gap: In order to maximize light absorption, the photocatalyst needs to have a bandgap suitable to absorb a large portion of natural sunlight. Figure 1.1 shows that almost 80% of the solar spectrum received by earth's surface lies in the visible (42%) and IR (53%) regions, while only a small portion of about 5% exists as UV light.¹⁸ This implies that the photocatalyst should be able to absorb at least light with a wavelength of 400 nm and above, corresponding to a bandgap lower than 3 eV. Typically, organic semiconductors like π -conjugated small molecules offer mechanical flexibility, low cost of production and have a low bandgap allowing them to absorb in the visible region, however, they often suffer from thermal instability and low charge mobility, thus limiting the second key process. In comparison, inorganic sulfides like CdS or ZnS, also have a comparably low bandgap (< 2.5 eV) but show a better charge carrier mobility along with good thermal and chemical stability; still they often suffer from photo-corrosion under illumination, releasing toxic metal ions, in the presence of oxygen and water.^{19,20} On the other hand, inorganic oxides like TiO₂ are resistant towards photo-corrosion, thermal degradation, and are chemically stable, but typically have a bandgap of over 3.2 eV limiting their absorption to the UV region. Since these benefits and challenges of the corresponding material classes are often inherent to their nature, combining complementary materials might result in an overall superior photocatalyst system. Several studies have shown that modifying wide bandgap materials, like TiO₂ and others, with inorganic dopants or organic functional groups can help lowering the bandgap, allowing it to absorb in the visible light.^{21,22} These modification strategies can not only lower bandgap values allowing the photocatalyst to absorb in the visible region, but also – when combined with organic molecules that typically have a higher absorption coefficient – can significantly improve the overall number of electron-hole pairs generated under illumination.

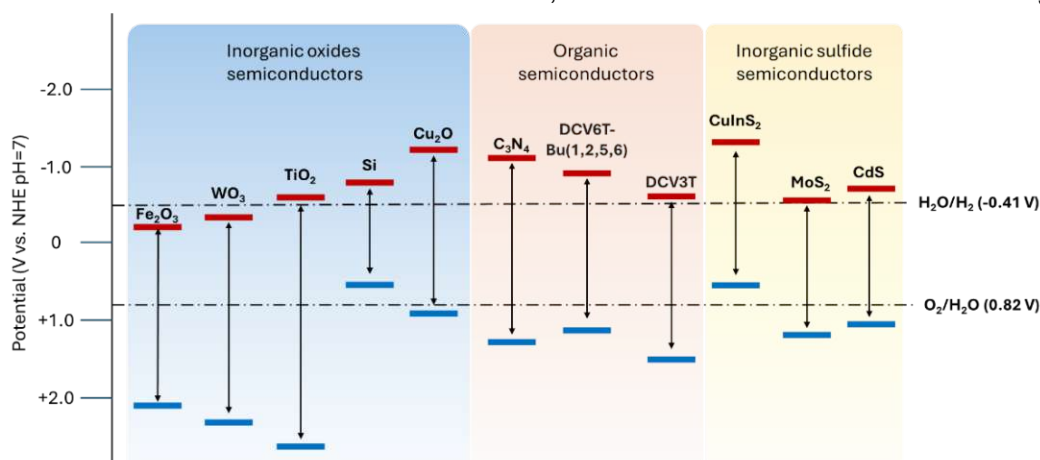
Once a photocatalyst absorbs light thereby generating an excited electron hole pair, in the absence of any other driving force, the coulombic attraction (excitonic binding energy) between the two often lead them to recombine either in the bulk or on the surface or the material as shown in Scheme 1.1. Therefore, the next important step is to ensure the separation of as-generated electron-hole pairs and migration of thus formed free-moving charge carriers to the active sites, usually at the photocatalyst surface. While there are several material properties like defect location and type, or the bonding nature, etc. that can affect the overall charge separation, when considering pristine material properties, the dielectric constant plays one of



Scheme 1.1 Photocatalytic steps in a semiconductor material: (i) photon absorption leading to generation of electron-hole pairs followed by (ii) charge carrier migration to the surface finally taking part in (iii) reduction or oxidation reactions like water splitting

the key roles in determining the ability of that material to effectively split the excitons and transport the photogenerated charge carriers to the active sites.

2. Dielectric constant and charge carrier mobility: The dielectric constant of any material can be correlated to its ability to mask the coulombic attraction between the photogenerated electrons and holes. Therefore, materials with higher dielectric constants tend to have better carrier mobility and higher lifetimes. Typically, inorganic semiconductors have a higher dielectric constant as compared to organic semiconductors due to their long-range order and strong bond formation. For example, BaTiO_3 , SrTiO_3 , and TiO_2 have some of the highest dielectric constants ranging from 86 to over a 1000 but each of these is a wide bandgap semiconductor, while low band gap organic semiconductors like graphitic carbon nitride (g-CN) have a much lower dielectric constant of 4 to 8. Nevertheless, recent studies showed that combining g-CN



Scheme 1.2 Conduction and valence band positions of different semiconductors showing the redox potentials required for splitting water into H_2 and O_2 . Reproduced from ref 16.

with TiO_2 , that has a higher (x1.5) dielectric constant, resulted in a visible-light-absorbing photosystem with enhanced charge separation compared to pure g-CN.²³ Furthermore, such a photosystem with $\text{TiO}_2/\text{g-CN}$ also acts as a bifunctional photocatalyst that is photoactive for both H_2 production and RhB-dye removal, reinforcing the idea of combining organic and inorganic materials for enhanced photocatalytic properties.

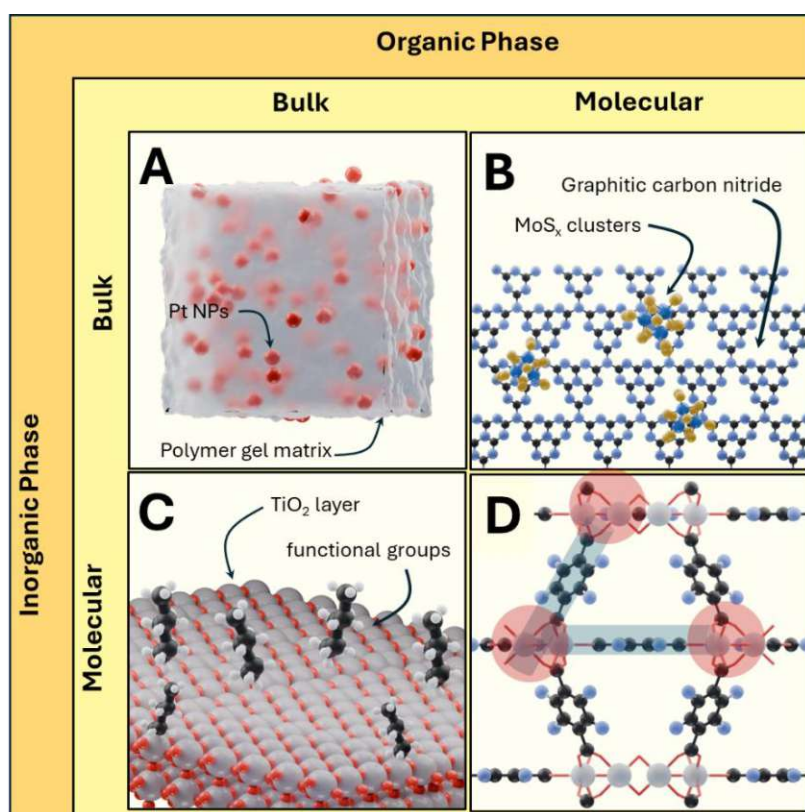
Once the charges reach the surface (active sites at the interface), the final important step is their utilization in a reduction or oxidation reaction. The ability of a semiconductor in facilitating a specific chemical reaction strongly depends on the alignment of its valence and conduction band edges with the oxidation and reduction potentials of the target reaction. For instance, to carry out the water splitting reaction, the materials' valence band edge must be higher (more positive) than 0.82 V and conduction band edge must be lower (more negative) than -0.41 V (vs normal hydrogen electrode, NHE, at pH 7, Scheme 1.2). Typically, photocatalysts which possess small bandgaps and favorable charge separation, often do not have the right band edge positions to carry out both half reactions for the overall water splitting reaction (like WO_3 , BiVO_4), and a selected few that do (g-CN, Cu_2O), often suffer from other issues such as surface defects – leading to charge trapping – and slow reaction kinetics. Therefore, to overcome this challenge, a strategy of combining these photocatalysts either with other inorganic materials or organic functional groups appears, resulting in a better (hybrid) photosystem that can efficiently split water to produce H_2 .

1.3 Hybrid photosystems

1.3.1 Overview

While a single photocatalyst material, like TiO_2 , BiVO_4 , or $\text{g-C}_3\text{N}_4$, can possess all the necessary properties to allow photocatalytic water splitting, their performance can be significantly enhanced by designing a multi-component photocatalytic system. Such a photosystem can be prepared with a combination of organic and inorganic parts, yielding new hybrid materials that not only retain their individual components' properties but enable synergistic effects at the interface, which strongly improve their overall photocatalytic activity. In 2020, Goodman et al., classified these hybrid photosystems based on the dimensions (atomic, molecular, or bulk) of the individual components, thereby resulting in four classes of hybrids, as shown in schematic 1.3.²⁴

Class A generally describes hybrid photosystems made by combining bulk phases of organic and inorganic materials, like polymer/inorganic composites. This class also represents the first ever hybrids emerging from polymer sol-gel chemistry as described by Judeinstein and Sanchez in 1996.²⁵ Following this, several studies started to appear on using hybrid materials for photocatalysis, like combining g-CN with $\text{TiO}_2/\text{TaON}/\text{CdS}$, for water splitting or CO_2 reduction reactions.^{26,27} They showed that each of these hybrids formed heterojunctions at their interface thereby enhancing the charge separation resulting in an overall enhanced catalytic performance.



Scheme 1.3 (a) Class A showing an example of Pt nanoparticles in a polymer gel forming a bulk-bulk combination hybrid (b) organic functional groups anchored onto TiO_2 surface (c) inorganic MoS_x clusters immobilized onto organic g-CN sheet (d) MIL-125 MOF formed with TiO_x inorganic nodes connected via terephthalic acid linker molecules representing hybrids combined using molecular components

Class B and class C photosystems are generally hybrids synthesized with one of the two phases is in their atomic or molecular form, for instance, decorating Pt atoms or molecular MoS_x clusters onto a g-CN or graphene surface (**class B**), or functionalizing the surface of TiO₂ with visible light absorbing molecules like Eosin Y (**class C**).^{28–31} Both these photosystems combine attractive visible light absorption, thermal and chemical stability, and fast reaction kinetics thereby resulting in enhanced photocatalytic performance. In addition to the advantages mentioned above, this approach can also be used to prepare a multi-component hybrid with more than two materials. For instance, Nandan et al. prepared a 3 component photosystem, TiO₂/(3-Aminopropyl)triethoxysilane/polyoxometalate hybrid for photocatalytic water oxidation, where they used the molecular organic groups (functionalized on the surface of TiO₂) as anchor points and charge transfer mediators to POM clusters – which carried out the water oxidation process.³² Such hybrids are also widely used in preparing dye-sensitized photoelectrocatalysts for hydrogen production.^{33,34} Most recently, Bourguignon et al. prepared a hybrid photoelectrode using NiO, molecular push-pull dye (pRK1) and cobalt tetrapyrrolyl catalyst, that was used for photoelectrochemical hydrogen production.³⁴

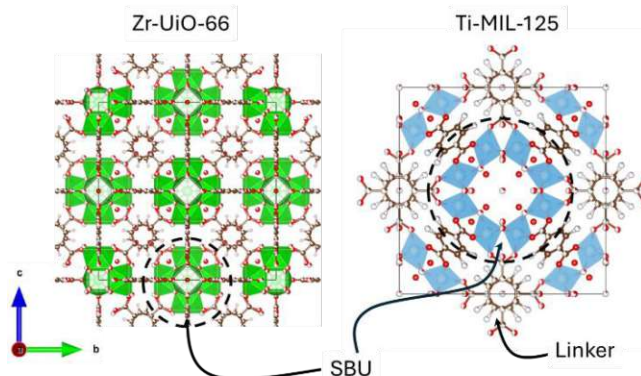
It is important to note that, while the hybrids classified above do not result in a fully new material that might have a unique unit cell as a building block, their interfacial interactions strongly influence the optoelectronic nature of both the components thereby resulting in positive synergistic effects towards its photocatalytic performance. For a simple case of Pt/TiO₂ hybrid, also called a hybrid semiconductor, the interfacial band bending of the TiO₂ conduction band minimum when in contact with Pt results in a strong driving force for the charge transfer to Pt (electron sink) resulting in an improved photocatalytic performance and better carrier mobility for TiO₂.^{35–37}

In contrast to hybrids discussed above, **class D** corresponds to hybrid photosystems prepared by combining atomic or molecular organic and inorganic components. Generally, these contain strong covalent bonding between the two components, resulting in an ordered multidimensional structure. Therefore, such a photosystem acts as a new material altogether, instead of a composite combination of two materials, as in the case of other classes. Metal organic frameworks (MOFs), where an organic molecule is linked to an inorganic metal/metal-oxo cluster (node) forming a 3-dimensional crystalline structure, are a stark example of such hybrids. These combine the benefit of the flexibility and versatility in the choice of different organic linkers – which allows to finetune the bandgap and other electronic properties – while the rigidity and favorable electronic properties of different metal-inorganic nodes allow to enhance the reaction kinetics and the overall performance. Since these hybrids are made by combining inorganic moieties bridged using organic molecules, they also tend to be extremely porous thereby having some of the highest surface areas and therefore a greater number of active sites, which can enhance their photocatalytic performance.

Building on Goodman's classification (Scheme 1.3), all photosystems designed and studied in this thesis can be categorized into two groups, namely, organic-inorganic hybrids (**OIHs**) and organic-inorganic architectures (**OIAs**). According to this, OIHs would be hybrid materials that fall under class D, while OIAs would be hybrid materials best described under the classes A, B, or C. The following section is dedicated to introducing the OIH and OIA photosystems studied in this thesis to provide an overview on the background motivation and strengths of each of them leading towards their potential in photocatalytic applications.

1.3.2 Organic-inorganic hybrids (OIHs)

1.3.2.1 Metal-organic Frameworks (MOFs)

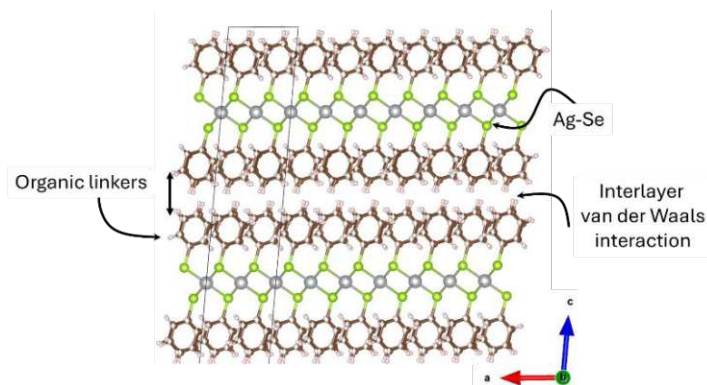


Scheme 1.4 Left showing the crystal structure of Zr-MOF (UiO-66) with $Zr_6O_4(OH)_4$ core and right showing the crystal structure of Ti-MOF (MIL-125) with $Ti_8O_8(OH)_4$ core, linked to 12 carboxylates groups from terephthalic acid linker

MOFs are a class of crystalline porous materials consisting of metal ions/metal clusters (as inorganic nodes) that are interconnected via organic linker molecules. These nodes are also called the secondary building units (SBUs) of the MOF since they are composed of polyhedral metal-oxygen structures, as shown in Scheme 1.4 for some of the widely known MOFs. One of the main strengths of MOFs is the versatility in the choice of organic linkers, which usually act as the light absorbing centers and therefore allow us to tailor the bandgap of the MOF. Furthermore, the use of large and flexible ligand molecules allows us to finetune the resulting porous structure, resulting in large surface areas, providing adequate anchoring sites for reactant molecules. Due to this modularity, MOFs have gained a lot of attention towards photocatalytic applications in solar fuel production and wastewater treatment. In 2007, Alvaro et al. reported for the first-time the usage of MOFs, namely MOF-5-Zn, for the photocatalytic degradation of phenol in aqueous solutions.³⁸ This field was then expanded by various other groups studying MOFs as photocatalysts for the degradation of harmful dye pollutants - such as methylene blue, methyl orange, and many more.³⁹⁻⁴¹ While there have been many advances in the field to improve their performance by synthesizing MOFs with higher surface areas for better adsorption, aqueous stability of the MOFs remains a major milestone since they are easily prone to hydrolysis in the presence of water, as water molecules can form bonds with the metal ions, slowly breaking down the MOF structure. Nonetheless, certain Ti- and Zr-based MOFs like the MIL-125 and UiO-66 families have shown to exhibit a relatively high water stability and therefore they have been widely studied for applications involving aqueous environments. Hence, inspired from these studies, Chapter 2 of this thesis explores a novel visible light absorbing Ti-based MOF for selective photodegradation of dye effluents, presenting a detailed study of the structure-function relationship further elucidating the underlying mechanism and pathways towards wastewater treatment.

1.3.2.2 Metal-organic-chalcogenolate assemblies (MOCHAs)

In comparison to MOFs, MOCHAs are a relatively new class of hybrid materials. These OIHs are typically made up of a network of 1D coordination polymers or stacked 2D coordination polymers – each consisting of metal chalcogen complexes held together via van der Waals attraction – as shown in Scheme 1.5. The study of metal chalcogen bond has been of huge interest since the 1990s, owing to its large application in the pharmaceutical industry, mainly due to their analogous structure to metalloproteins present in the human body. Since the first



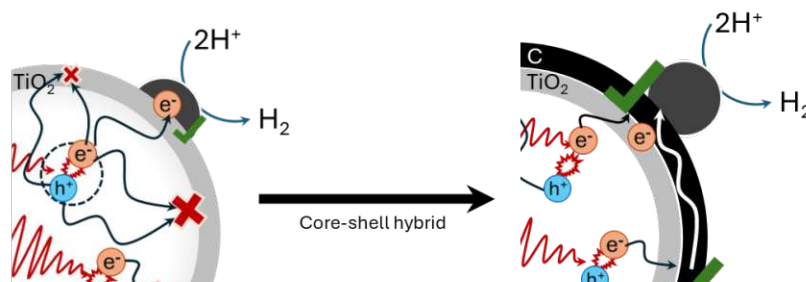
Scheme 1.5 Illustration of a 2D-Ag-based MOCHA of the formula [AgSe(C₆H₅)]

report of a 1D Ag-based MOCHA in 1983, there have been several major breakthroughs in their synthetic approach using a variety of organic-chalcogen-based ligands, with the objective to tune their physical and optical properties.⁴² While there has been some interest in 1D MOCHAs – specifically using Ag, Cu, and Au metal ions – 2D layered MOCHAs have gained a lot more interest due to the interlayer interactions resulting in interesting optical and electronic properties. For instance, in 2010, Che et al. reported a Cu-MOCHA displaying exceptional bulk conductivity of $\sim 120 \text{ S cm}^{-1}$, due to hydrogen bonding between the layers.⁴³ Recent perspectives on 2D-MOCHAs, have also compared them through the lens of layered transition-metal chalcogenides (like MoS₂, WS₂) and graphene, but with organic molecules attached on the surfaces through covalent interactions. This modification could provide improved dispersibility in various solvents and also modulate the electronic structure of these metal-chalcogenides by linker modifications. Furthermore, this view also provides an alternative approach towards exfoliating metal chalcogenides for catalytic applications, since the layers in 2D MOCHAs are only connected via weak van der Waals forces. Over the past two decades Ag-MOCHAs in particular have gained a lot of interest due to their photophysical properties. Recently, our group reported a major breakthrough in the synthetic strategy along with testing a specific group of MOCHAs for the electrocatalytic CO₂ reduction reaction.⁴⁴ Building on this report, Chapter 3 expands on the possibility of using three Ag-based MOCHAs as co-catalysts for the hydrogen evolution reaction.

1.3.3 Organic-inorganic architectures (OIA)s

1.3.3.1 Hybrid titania carbon spherogels (TiO₂@C)

TiO₂ is one of the most widely studied metal oxide photocatalyst due to its excellent advantages such as low cost, environmentally benign, good chemical and structural stability, etc. It was the first material used in demonstrating photoelectrochemical water splitting by Fujishima and

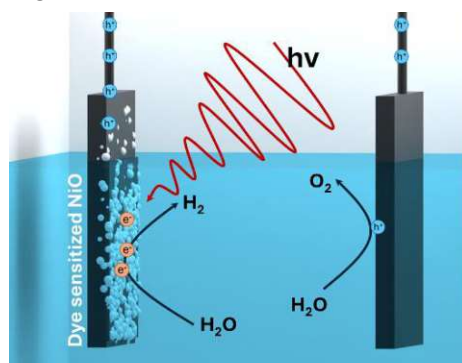


Scheme 1.6 Left shows the electron extraction via a single Pt nanoparticle (dark grey) on the surface along with various recombination centres as well, as compared to the right showing the enhancement of charge (electron) extraction from TiO₂ (light grey) due to high contact surface area using a core-shell architecture with graphitic carbon (black).

Honda in 1972, kickstarting the field of photo- and photoelectrocatalytic water splitting.⁴⁵ However, two major drawbacks limit its potential as a commercially viable photocatalyst: first the wide bandgap limiting its absorption to the UV region of sunlight (<5%) and second the rapid electron-hole recombination and a relatively low charge transport, resulting in low quantum efficiencies. While a few strategies such as using co-catalyst materials like metallic Pt nanoparticles (NPs) or molecular co-catalysts (MoS_x) can act as an electron sink, the lack of control and inhomogeneity of deposition can limit the enhancement to only those interfaces while the rest of the surface can still act as recombination centres (Scheme 1.6). Alternatively, core-shell architectures provide an excellent solution where the two materials have a homogeneous and vast contact area resulting in excellent interfacial interactions. For example, studies on hybrids made using TiO₂ and carbon nanotubes (CNTs) or using other graphitic carbon sources have demonstrated to have a drastic improvement in the photocatalytic performance as compared to pristine TiO₂. In the case of core-shell architectures using CNTs, the improvement was attributed to the enhanced electron-capturing efficiency of the structure supported by the observed longer lifetimes of the photogenerated electrons. Furthermore, the electron-extraction efficiency increased upon using shorter CNTs which were able to create a better interface with the TiO₂ core.⁴⁶ Similar to this, another study reported a higher CO₂ uptake capacity and improved photocatalytic CO₂ reduction performance due to the homogeneity of the carbon/TiO₂ interface.⁴⁷ Several other studies have also reported similar enhancements when using TiO₂/carbon core-shell architectures for various applications in photocatalytic hydrogen peroxide generation and dye degradation.^{48–50} Tu et al. reported the fast migration of electrons from TiO₂ to graphene (or other graphitic materials) is mainly due to the d-π electron orbital overlap in Ti–O–C band.⁵¹ Furthermore, TiO₂ has a conduction band minimum at -4.21 eV and the work function of graphene is at approximately -4.42 eV, thereby facilitating the electron extraction from TiO₂.^{52,53} Based on these previous studies, Chapter 4 of this thesis explores a TiO₂@C core-shell architecture prepared via a novel sol-gel method for photocatalytic hydrogen production. Furthermore, this chapter also elaborates on effect of modulating the relative TiO₂ content and post synthetic treatments to maximize its photocatalytic HER performance.

1.3.3.2 Dye sensitized NiO photocathodes

In contrast to the above three approaches purely depending on material design for improving the photocatalytic performance, photoelectrocatalysis, a bridge between the fields of photo- and electrocatalysis, is also an attractive approach towards hydrogen production since it can tremendously enhance a photocatalysts performance by providing a driving force that suppresses the inherent charge recombination rates within the material. For example,



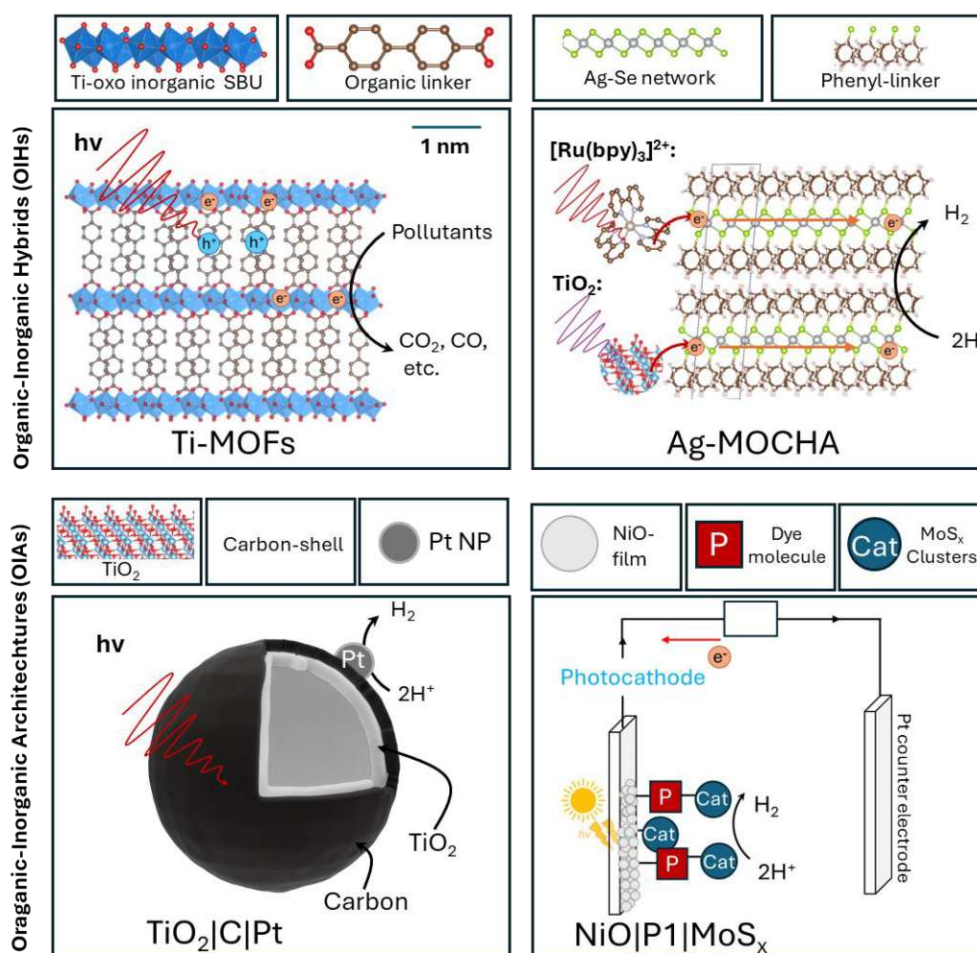
Scheme 1.7 Photoelectrocatalysis setup showing a dye sensitized NiO photocathode which upon illumination and a small bias separates the photogenerated charges, carrying out water reduction and oxidation to H₂ and O₂ on each of the electrodes

Wang et al. reported that by applying a small potential bias (0.5V) on a $\text{TiO}_2/\text{Cu}_2\text{O}$ hybrid the overall selectivity of the photocatalyst towards hydrogen production increased from 5 to 85%.⁵⁴ Even in the original discovery by Fujishima and Honda, photoelectrocatalytic approach was used to demonstrate the benefits of using solar-assisted water splitting. Typically, photoelectrocatalysis is carried out by applying a small bias to a photocathode, where the reduction reaction takes place, and a photoanode, responsible for oxidation reactions; as shown in scheme 1.5. This bias not only acts as a driving force for initial charge separation but also physically separates the charge, across two electrodes (over cm apart), therefore further isolating the oxidation and reduction sites, which in a typical photocatalyst would be located on the same material (less than a few nm apart) increasing the chances of charge recombination and back reaction. Therefore, designing hybrid materials that can effectively make use of this advantage is also a viable approach towards water splitting. In general, widely studied architectures include a wide bandgap semiconductor functionalized with visible-light-absorbing sensitizers along with a co-catalytic material. In such an organic-inorganic architecture, the wide bandgap semiconductor, often a metal oxide, provides structural, chemical, and thermal stability, while the dye sensitizers efficiently capture sunlight initiating the catalytic process; together creating an efficient and stable photosystem. For example, Szaniawska et al. recently reported an architecture made using dye-sensitized NiO photocathodes decorated with palladium nanoparticles for the photocatalytic hydrogen production. Based on these points, Chapter 5 of the thesis explores a similar OIA with organic dye sensitized mesoporous NiO decorated with inorganic molybdenum sulphide catalysts for the photoelectrocatalytic hydrogen production.

Motivation and aims

Based on the discussion in the previous sections, in this thesis I will present the study of two OIH and two OIA photosystems (Scheme 1.8). The results are divided into four chapters with the primary focus of each chapter on evaluating the catalytic performance of the hybrid photosystem and understanding the underlying mechanism behind it. The study also explores the limits of each photosystem in terms of reusability and overall stability under turnover conditions. The structure of the thesis includes a preface before each chapter giving an overview of the work presented in that chapter and the outcomes of the project. Furthermore, each chapter consists of a brief introduction on the specific photosystem studied and the motivation behind it.

Chapter 3 explores the use of a novel Ti-based metal-organic framework (OIH), namely COK-47, as a potential photocatalyst for wastewater treatment, specifically targeting organic-dye-molecules as pollutants (Scheme 1.8a). The chapter tries to understand the fundamental



Scheme 1.8 Overview of the 4 hybrid photosystems studied in this thesis and their building blocks. (a) Top left shows the schematic of a Ti-based MOF consisting of interconnected Ti_2O_3 SBUs with charge delocalisation and conductivity in the 2D-layers linked via a bpdc^{2-} molecules. (b) Top right shows another class A hybrid called a MOCHA built using a $[\text{AgSeC}_6\text{H}_5]$ repeating subunit. (c) Bottom left shows a core-shell OIA consisting of a TiO_2 core and carbon shell and (d) Bottom right shows another OIA, built as a photocathode using NiO, organic dye P1, and a molecular catalyst MoS_x .

interactions between the photocatalyst and pollutant molecules, and the importance of their role in the overall photodegradation process and efficiency.

Chapter 4 explores a novel class of Ag-MOCHAs (Scheme 1.8b) as potential co-catalysts for the hydrogen evolution reaction. The study uses two light sensitization approaches, using a Ru-based dye or TiO₂ NPs, for testing the co-catalytic performance of the MOCHAs and explores the factors determining the stability and overall H₂ production performance.

Chapter 5 explores the first OIA consisting of a core-shell structure built using a TiO₂ core and carbon shell. In this chapter, effects of two aspects of the core-shell structure on its photocatalytic HER performance are studied: first, the composition i.e. the ratios of TiO₂ and carbon in the OIA, and second the surface morphology. The effect of post synthetic treatments like annealing in different atmospheric environments which change the surface morphology and thereby the overall photocatalytic performance are also studied.

Chapter 6 is a preliminary study on the design and optimization of an OIA photocathode and tests its performance for the photoelectrocatalytic hydrogen evolution reaction. The OIA is constructed using a stable p-type NiO, visible light absorbing organic dyes (Ru(bpy)₃²⁺ and P1) and a molecular catalyst (MoS_x). The photocathode performance, stability, and recyclability are then tested for the PEC H₂ production.

Finally, chapter 7 concludes with a recap and an overview of each chapter highlighting the advantages of different ways of making organic-inorganic hybrids for photocatalysis along with some of the key findings and results. The chapter also discusses the outlook of each work with some ideas for further improving the prepared OIHs and OIAs.

Chapter 2: Methods and instrumentation

This chapter describes all the characterization methods that were used to analyze the physical, chemical, and optoelectronic properties of each of the hybrid photosystem. Each section briefly discusses the theoretical background, the material property studied using the method, and the protocol followed to measure the samples along with details on the corresponding devices.

2.1 X-ray diffraction

X-ray diffraction (XRD) is a non-destructive characterization technique which can provide useful information regarding the crystal structure, phase analysis, dominant crystal orientations, average grain size and more. It is based on the constructive interference between incident monochromatic X-rays when diffracted from a crystalline sample. Typically, when a beam of monochromatic X-rays is scattered by the atoms in a periodic crystal lattice, they result in either cancelling each other out (destructive interference) or adding up together (constructive interference). For instance, Figure 2.1a shows the two parallel incident beams of X-rays onto two parallel lattice planes in a crystalline material. The Bragg equation provides the necessary conditions required for constructive interference of the scattered rays and given as follows,

$$2d\sin\theta = n\lambda$$

where, d is the distance between the two lattice planes, θ is the angle of incidence of the x-rays, and λ is the wavelength of the incident x-ray beam. The set of angles resulting in a constructive interference provides a characteristic set of data for different materials.

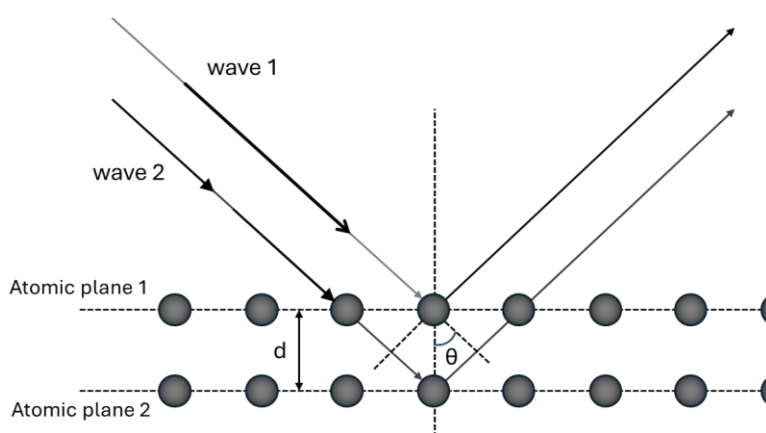


Figure 2.1a Schematic of a two-dimensional crystal lattice with a set of parallel planes diffracting two light waves with a change in path length of $2d\sin\theta$

In this thesis, XRD analysis was used to confirm the successful synthesis of different materials in their pristine state as well as after their catalytic testing to ensure that the crystal structure is retained. All measurements were carried out on a XPERT II: PANalytical XPert Pro MPD (Θ - Θ Diffractometer). The sample was placed on a Si sample holder and irradiated with a Cu X-ray source (8.04 keV, 1.5406 Å). The signals were then acquired with Bragg-Brentano Θ / Θ -diffractometer geometry ranging from 5° to 80° degrees using a semiconductor X'Celerator (2.1°) detector.

2.2 Optical spectroscopy

UV-Vis (Ultraviolet-visible) spectroscopy, diffuse reflectance spectroscopy (DRS), and photoluminescence (PL) spectroscopy are 3 common ways to characterize the optical properties (absorption and emission) of a material in either liquid or solid form.

2.2.1 UV-Vis spectroscopy

UV-vis spectroscopy is used to determine if the material absorbs any wavelengths in the ultraviolet or visible range providing information about the possible electronic transitions in the material or any other interaction of the sample with light. Generally, UV-vis spectroscopy is used to characterize liquid samples or thin films samples due to the way it is measured. A typical measurement setup consists of a light source (Xe lamps), monochromators to separate the incident light into individual wavelengths, a samples holder, and finally a detector which can convert the transmitted light into electrical signals. The amount of light absorbed or transmitted by a sample is given by the beer-lamberts law, which states that the absorbance is directly proportional to the sample path length and the sample concentration, written as follows,

$$A = \varepsilon cl,$$

Where A is the absorbance, c is the concentration, and l is the light path length through the sample in cm, and ε is the proportionality constant also called the molar absorptivity of the sample.

In this thesis, UV-vis spectroscopy was used to track and determine the dye concentration in the solution during a photodegradation experiment. First a calibration curve relating the intensity of absorption at a particular wavelength to the known concentration, which was then used to determine the unknown concentration of the dye solution as described in section 3.4.2.

2.2.2 Diffuse reflectance spectroscopy

Diffuse reflectance spectroscopy (DRS) is a subset of absorption spectroscopy where instead of tracking the amount of light transmitted or absorbed by the sample, the amount of light reflected is measured. DRS is typically used to measure powder samples as compared to UV-Vis, which is used for liquid or thin film samples. In a DRS measurement, the light incident on the powder sample surface is reflected in a diffused manner (specular reflection) due to the random orientation of particles in sample. This diffused light is then collected to identify the amount of light absorbed or reflected. This measurement approach alleviates the disadvantages of UV-Vis spectroscopy where the measurement often has solvent interaction effects on the sample absorption properties.

For semiconductor materials, which typically absorb all light above a particular wavelength resulting in both band-to-band transitions and excitation from deep band states in both valence and conduction band, DRS measurements can be used to the determine the optical bandgap of the material. In 1931, Paul Kubelka and Franz Munk proposed their theory on how the color of a substrate changed after applying a layer of paint with a certain thickness and composition. However, this theory was further extended to analyze the DRS spectrum of a solid material under a few assumptions. Briefly, the Kubelka-Munk equation is expressed as,

$$\frac{K}{S} = \frac{(1 - R_{\infty})^2}{2R_{\infty}} = F(R_{\infty})$$

where R_{∞} is reflection of the sample when it is infinitively thick, K represents absorption coefficient, S represents scattering coefficient and $F(R_{\infty})$ is the remission KM function. Furthermore, this remission function represents the absorption coefficient of the material, which when inserted into the Tauc equation and plotted against the energy of the incident wavelength can be used to determine the bandgap of the material.

In this thesis, DRS was used to determine the optical bandgaps of several hybrid materials in their pristine form as well as after any chemical or thermal treatment, in or determine their effects. UV-Vis spectroscopy was performed on a Jasco V670 UV-Vis spectrometer. The samples were prepared in aqueous solution with different concentrations of dyes; UV-Vis spectra were recorded in absorbance mode. Absorption spectra of powdered samples were measured on the same device in solid-state via diffuse-reflectance spectroscopy (DRS) using MgSO_4 as a reference.

2.2.3 Photoluminescence spectroscopy

Photoluminescence (PL) is the phenomenon where an excited electron relaxes from the conduction band edge or lowest unoccupied molecular orbital (LUMO) of a semiconductor material to the valence band or (highest occupied molecular orbital) HOMO level, releasing energy in the form of light. The wavelength and intensity of this emitted light are measured and analyzed to reveal details about the material's optoelectronic properties such as the lifetime of the photogenerated charges or the number of decays in the relaxation process. Typically, the excited electron can relax directly from its first excited singlet state resulting in fluorescence, however, in some cases it can undergo a spin change to a triplet state and then relax radiatively resulting in phosphorescence.

In this thesis, I employed solid-state PL (ssPL) to understand the charge carrier lifetimes of photogenerated charges. I also used it to identify charge extraction ability of certain co-catalyst anchored onto the photocatalyst by tracking the PL intensity of the material. All measurements were carried out on a Picoquant FluoTime 300 photoluminescence spectrometer, equipped with two excitation sources: a continuous-wave (300 W) Xe arc lamp (coupled with an excitation double monochromator) and a pulsed laser at 377 nm excitation. The device includes a PMA Hybrid 07 detector, coupled to an emission double monochromator. For lifetime measurements time-correlated single photon counting (TCSPC) system was utilized.

2.3 Thermogravimetric analysis

Thermogravimetric analysis (TGA) is carried out by constantly measuring the mass of a material when heated from room temperature to upto 800 °C, in a set atmosphere such as N_2 or synthetic air mixture. The measurement tracks the weight gain or weight loss during this process which provides information about the thermal stability of the material under given conditions. In the case of hybrids, each component can have a decomposition temperature characteristic to it. Therefore, TGA curves showing the relative weight loss at different temperatures can be used to identify the relative amounts of different materials present in a hybrid.

In this these, I used TGA to first identify the thermal stability of several hybrid materials and second, to determine the amount of a photocatalyst loaded onto a substrate. All measurements were carried out with a PerkinElmer Thermogravimetric Analyzer TGA 8000 equipped with an autosampler. The samples were loaded onto Al_2O_3 crucibles and heated at the rate of 5 °C min^{-1} under air and N_2 atmosphere from 25-650°C.

2.4 Total X-ray fluorescence spectroscopy

X-ray fluorescence (XRF) spectroscopy is a non-destructive technique that can be used to determine the elemental composition of both solid and liquid samples. To briefly its working principle, when a sample is excited using high energy X-rays, electron from the inner atomic shell are knocked out and replaced or refilled by electrons relaxing from the next outer shell releasing X-rays of lower energy during the relaxation, which corresponds to the energy gap between the two electronic shells resulting in a characteristic fingerprint of each material. Furthermore, the intensity of each x-ray energy peak released can be correlated to the amount of the element present, by preparing and comparing against a calibration curve.

In this thesis, the measurements were performed in a total reflection mode, where the source is in a critical angle and the detector at 90°, with respect to the sample. Such a setup provides higher sensitivity to the various elements present in the sample composition. The measurements were carried out with an Atomika 8030C x-ray fluorescence analyzer with a molybdenum x-ray source monochromatized K_{α} -line. Typically, a small bead of sample was loaded onto the blank reflector substrate using a pipette tip. Prior to measuring the sample, the reflector substrate was cleaned in soap water, ethanol, and finally rinsed with triply distilled water. The reflector substrate was also measured as a blank to ensure the absence of any impurities before measurement. Once the blank was clean, a tiny amount of sample was loaded onto it and measured in a similar way. In the case of hybrids samples containing multiple components, the intensity of the signal observed was correlated to the relative amount of that element using one of the major matrix elements as a reference in powder samples. In cases where this was not possible due to experimental limitations, a known amount of internal standard was added to the reflector substrate along with the sample for reference.

2.5 Electron microscopy

Electron microscopy is a technique used to visualize the surface morphology and structure of materials. Typically, a beam of electrons is focused on the sample and the reflected electrons are collected at a detector in a photon-multiplier converting the data to a visual image. Such imaging can be predominantly done in two operation modes, namely, scanning electron microscopy and transmission electron microscopy.

2.5.1 Scanning electron microscopy (SEM)

SEM produces images by bombarding the specimen with a focused electron beam which upon interaction with the sample surface results in the emitting of secondary electrons (SE), elastically back scattered electrons (BSE), Auger electrons (AE), and X-rays, depending on the penetration depth of the incident electron beam and the density of the material, as shown

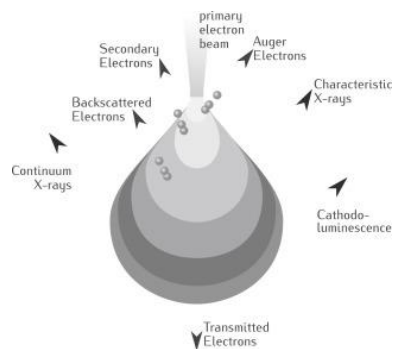


Figure 2.5.1a Schematic showing the different electrons generated in the sample upon electron beam irradiation

in Figure 2.5.1a. Each of these emitted electrons or signals can then be used to characterize certain material properties. For instance, secondary electrons that are generated close to the sample surface are generally used for imaging the surface of the material. On the other hand, back scatter electrons are electrons elastically scattered by direct interaction with the atomic nucleus. The number of backscattered electrons strongly depends on the atomic number of the material. This information can then be used to understand the chemical composition or distribution of different elements on the surface, since heavier elements will appear brighter and lighter elements will appear darker in contrast.

2.5.2 Transmission electron microscopy (TEM)

In contrast to SEM, TEM produces images by detecting the transmitted electrons through the sample. The electrons are collected from below the sample onto a phosphorescent screen. In the areas where the electrons are reflected and do not pass through the sample, the image dark, whereas, un-scattered electrons pass through and create bright areas, along with grey regions throughout showing the partial passthrough of electrons depending on the interaction of the electrons with the crystal lattice. Therefore, these images are also called bright-field images. Figure 2.5.2a shows a schematic of a TEM and its components including a series of electromagnetic lenses, sample holder, detector screen, etc.

2.6 Raman spectroscopy

Raman spectroscopy is a non-destructive analytical technique used to study the vibrational and rotational modes of molecules or materials.⁵⁵ It is based on the inelastic scattering of photons from a monochromatic light source, a phenomenon known as Raman scattering.^{56,57} Typically, most of the scattered light has the same energy (wavelength) as that of the incident light (Rayleigh scattering). However, a small fraction of the incident light interacts with the molecular vibrational states such that the scattered light to have different energy to the incident light (Raman scattering), classified further as Stokes or anti-stokes scattering, corresponding to lower and higher energy scattered light, respectively. Typically, anti-stokes is even more unlikely than stokes scattering and usually provides similar information as stokes scattering. Importantly, in the case of stokes scattering, the energy transfer from the light to the molecule is exactly the amount required to excite one of the molecular vibrations of that particular molecule or material, providing a fingerprint characteristic for material identification.

In this thesis, raman spectroscopy was used to characterize the graphitic nature of the carbon shell and TiO₂ core, in the core-shell architecture studied in chapter 5. All measurements were carried out using a 532 nm laser excitation and a laserpower of 4 mW. A Thermo Scientific DXR2 raman microscope equipped with a confocal microscopy BX41 (Olympus corp.) and a 10x objective with a 0.25 numeric aperture was used.

2.7 Attenuated total reflection Fourier transform infrared spectroscopy

Attenuated total reflection Fourier transform infrared spectroscopy (ATR-FTIR) is another technique that uses the interactions of infrared light with the different vibrational modes of the bonds in molecule or material to analyze and characterize the material. It works on the concept of total internal reflection at the interface of two materials, where the latter has a higher index of refraction than the former, thereby generating an evanescent wave. Evanescent waves are created when the IR light cannot propagate through the sample and is concentrated at a small region or point where the total reflection takes place. These evanescent waves penetrate out of the sample and can interact with the vibrational states of a molecule, as shown in Figure 2.7a. In a typical measurement, the areas of the sample in contact with the evanescent wave absorbs some of the IR depending on the sample, which is absent in the total reflected

beam. This information can then be used to identify the various vibrational states for material characterization.

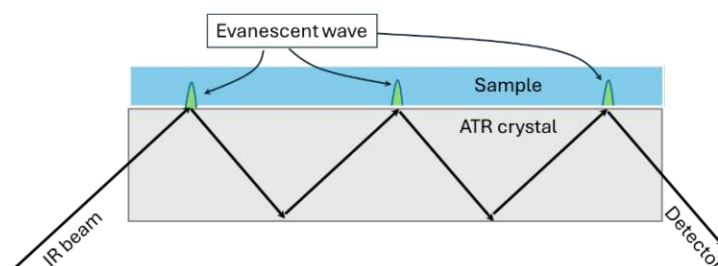


Figure 2.7a Schematic showing the working principle of the ATR-FTIR measurement where the evanescent waves interact with the vibration modes of the sample and are thereby absorbed which is then detected by a detector

In this thesis, all powder samples were characterized using a PerkinElmer spectral UATR-TWO with a spectrum two Universal ATR (Single reflection diamond) accessory.

2.8 X-ray photoelectron spectroscopy

X-ray photoelectron spectroscopy (XPS) is a non-destructive surface sensitive analytical technique that can be used to identify and quantify the chemical composition of the elements present in a sample. It is based on the photoelectric effect but instead of using light, a beam of soft X-rays (energy lower than $\sim 6\text{keV}$) is bombarded on to the surface knocking out some of the core electrons and the kinetic energy of the emitted electrons is measured to thereby calculate the binding energy of the electron using the following formula,

$$h\nu = BE + KE + \phi_{spec}$$

where, $h\nu$ is the energy of the x-ray, BE is the binding energy of the electron, KE is the kinetic energy, and ϕ_{spec} is the spectrometer work function. The x-rays can typically knock out electrons both on the surface and well deep into the sample. The electrons produced in the bulk of the sample undergo multiple inelastic collisions before escaping the surface and thus have a low kinetic energy, however, the electrons knocked from the surface only contribute to the characteristic photoelectron peaks. The binding energy obtained from these electrons is characteristic of the material and depends on the chemical environment thereby providing information such as the oxidation state of the element.

In this thesis, XPS analysis was used to analyze the oxidation of state of the individual elements in the hybrid material or architecture. Furthermore, it was also used to test the stability of the hybrid after catalytic testing. All experiments were carried out on using a custom-built SPECS XPS-spectrometer equipped with a monochromatized ($\text{Al-K}\alpha$) X-ray source and a hemispherical WAL-150 analyzer. The samples were mounted onto the sample holder using double-sided carbon tape. The excitation energy was set to 1486.6 eV with the beam energy and spot size of 70 W onto $400\text{ }\mu\text{m}$, respectively; The incident angle was set to 51° with respect to the sample surface normal. All measurements were carried out with a base pressure of $5 \times 10^{-10}\text{ mbar}$ and a pressure of $2 \times 10^{-9}\text{ mbar}$ during measurements.

Chapter 3: Ti-based MOFs as OIH photosystems for visible-light-driven water remediation

This chapter studies a recently reported Ti-based MOF, called COK-47, for its performance in visible light driven photocatalytic wastewater treatment, specifically towards industrial dye degradation. This study benchmarks its performance against other such hybrid materials and sheds light on the fundamental interactions and chemical processes leading to dye degradation, using a series of experimental and characterization techniques.

The work presented in this chapter has been published as a research article in the Journal of Materials Chemistry A, with a DOI number of: [10.1039/D4TA01967A](https://doi.org/10.1039/D4TA01967A), along with a back cover feature in the special edition as shown below. The publication is an open-access article with the contents shown made accessible under a CC BY 4.0 license.

My contributions as the first author include the initial ideation and proof-of-concept experiments followed by experimental design and data analysis, and finally, summarizing the overall results and paper writing. A significant portion of the work was carried out in the bachelor thesis of Magdalena Ladisich under my supervision. I would also like to mention that this work was inspired by a previous publication by one of the co-authors and colleague, Pablo Ayala, on designing a novel synthetic approach of previously reported COK-47 and exploring its capability in visible light driven hydrogen evolution published in Advanced Energy Materials in 2023.

Journal of
Materials Chemistry A



PAPER

View Article Online
View Journal



Cite this: DOI: 10.1039/d4ta01967a

Harnessing a Ti-based MOF for selective adsorption and visible-light-driven water remediation†

Stephen Nagaraju Myakala,^a Magdalena Ladisich,^a Pablo Ayala,^a Hannah Rabl,^a Samar Batool,^a Michael S. Elsaesser,^b Alexey Cherevan^{b,*a} and Dominik Eder^{b,*a}

In pursuit of universal access to clean water, photocatalytic water remediation using metal–organic frameworks (MOFs) emerges as a strong alternative to the current wastewater treatment methods. In this study, we explore a unique Ti-based MOF comprised of 2D secondary-building units (SBUs) connected via biphenyl dicarboxylic acid (H₂bpdcc) ligands – denoted as COK-47 – as a visible-light-driven photocatalyst for organic dye degradation. Synthesized via a recently developed microwave-assisted method, COK-47 exhibits high hydrolytic stability, demonstrates a strong dye uptake, and shows noteworthy dye-degradation performance under UV, visible, and solar light, outperforming benchmark TiO₂ and MIL-125-Ti photocatalysts. Due to its nanocrystalline structure and surface termination with organic linkers, COK-47 exhibits selective degradation of cationic pollutants while remaining inert towards anionic dyes, thus highlighting its potential for selective oxidation reactions. Mechanistic studies reveal the involvement of superoxide radicals in the degradation process and emphasize the need to minimize the recombination of photogenerated electron–hole pairs to achieve optimal performance. Post-catalytic studies further confirm the high stability and reusability of COK-47, making it a promising photocatalyst for water purification, organic transformation, and water splitting reactions under visible light.

Received 24th March 2024
Accepted 4th June 2024

DOI: 10.1039/d4ta01967a

rsc.li/materials-a

3.1 Introduction

In 1999, MIL-22 - the first Ti-based MOF – was synthesized and reported by Ferey and Serre using phosphonate groups as ligands.⁵⁸ Following this, in 2009, they reported the first Ti-carboxylate MOF called MIL-125, a highly porous material with excellent photochemical properties, which caused a boom in the research on Ti-based MOFs both for developing synthetic strategies of new Ti-MOFs and testing them for applications including various photocatalytic reactions.^{59,60} Due to the high valency metal ion (Ti^{4+}), these Ti-MOFs often show high chemical and hydrolytic stability, which is attributed to the strong coordination bond formed between carboxylate based ligands (hard base) and high valent Ti^{4+} ion (hard acid) according to Pearson's hard-soft acid-base (HSAB) principle.^{61–63} Over the course of two decades, the promising optoelectronic properties and higher chemical stability has allowed the use of Ti-MOFs in solar fuels generation and wastewater remediation via photocatalysis, making them a potential alternative for TiO_2 .^{64–71} Typically, the linker molecule is the light absorbing center, photogenerating an electron-hole pair followed by a ligand-to-metal-electron transfer to the SBU, where the reduction reaction can take place. However, in a 3D framework where each SBU is linked via linkers the electron mobility is significantly lower as compared to typical inorganic semiconductors.^{72,73} This is generally due to the porosity of the MOF resulting in large distances between ligands preventing the π -stacking interactions, or the large size of the ligand itself preventing metal-to-metal charge transfer. Till date, there are only a few reported MOFs which are intrinsically conductive, where the conduction is either electron hopping or via a guest molecule creating an electronic bridge between the two SBUs.^{74,75} More recently, another subclass of MOFs has emerged as excellent photocatalytic hybrids with 1D/2D Ti-SBU units interconnected via organic linkers. These MOFs consist of SBUs built out of almost an infinite chain (1D) or plane (2D) of metal oxo clusters, unlike other typical MOF structures where the SBU consists of either a single or polyhedral of metal-oxo clusters connected via linker molecules. It is predicted that this nature of the SBU allows delocalization of the electrons with the chain or plane, resulting in improved conductivity and charge separation. In 2018, Wang et al. reported the first such MOF, namely, MIL-177-HT, which featured a 1D infinite Ti-O SBU (Ti_6O_9)_n chain showing excellent chemical stability in acidic environments.⁷⁶ Following this, several other groups reported such 1D Ti-MOF architecture(s) that exhibit excellent photoconductive properties with long-lifetimes for the photogenerated charges.^{77–79} However, till date there are only two reports of 2D Ti-SBU based MOFs, IEF-11⁸⁰ reported in 2021, and COK-47 (Centrum voor Oppervlaktechemie en Katalyse) reported in 2019.⁸¹

Motivated by the unique structural properties of 1D/2D SBU MOFs along with their advantageous impact on charge separation, this chapter will study the novel MOF COK-47 consisting of Ti-oxo cluster (TiO_6) as the SBU connected via biphenyl-dicarboxylate (bpdc²⁻) linker molecule as shown in Figure 3.1a. This MOF was first reported by Smolders et al. for its use as a thiophene oxidation catalyst. Apart from improved charge extraction/separation due to the 2D SBU structure, COK-47 is very attractive material because of its high condensation degree (i.e. high oxo/Ti ratio of x), which is not far from that of TiO_2 , known for its wide use in photocatalytic applications.⁷⁶ Unfortunately, the original synthesis of COK-47 reported in 2019 resulted in a large bandgap semiconductor behavior with a bandgap of > 3.1 eV limiting its absorption to UV light. In 2023, our group reported an alternative synthetic strategy, using a microwave based approach, resulting in uniform-size nanoparticles absorbing in the visible region and having an optical bandgap of ~ 2.7 eV.⁸² We also demonstrated that this variant of COK-47 hybrid can be used as an excellent photocatalyst for hydrogen production when coupled with a co-catalytic material such as Pt.⁸³ Our results show that while the electrons

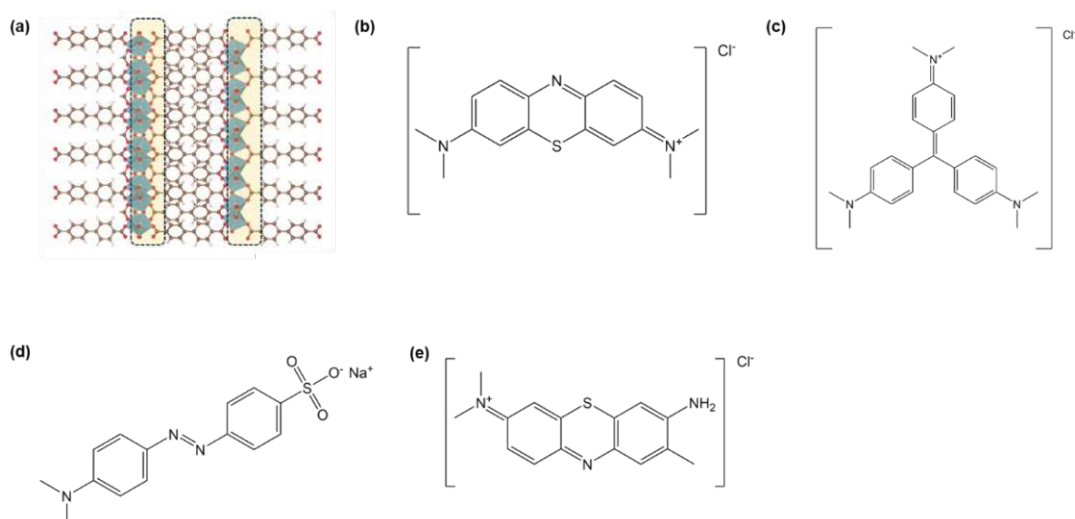


Figure 3.1 (a) Illustrative model of an isolated COK-47 nanoparticle showing the 2D SBU connected by bpdc²⁻ ligands (b) Methylene Blue (c) Crystal violet (d) Methyl orange and (e) toluidine blue structures

photogenerated in COK-47 are able to effectively reduce H⁺ to H₂, the photogenerated holes are not consumed effectively towards the oxygen evolution reaction, thereby necessitating the use of a sacrificial hole acceptor, such as methanol in this case. While co-depositing another co-catalyst that can promote the water oxidation reaction is an alternate strategy, the design and synthesis of such a system can be challenging. However, achieving effective and economically viable photocatalytic H₂ production can be realized by replacing methanol with an organic pollutant molecule. Therefore, in this chapter we explore the photocatalytic performance of COK-47 in the degradation of relevant dyes, which can then be extended to the previously reported Pt/COK-47 photosystem. In this study, methylene blue (MB) was studied as a model dye followed by further testing the performance of COK-47 for the degradation of other dyes such as crystal violet (CV), toluidine blue (TB), and methyl orange (MO) (Figures 3.1b-3.1e). In addition to COK-47, two other MOFs – MIL-125 and COK-47-bpy (COK-47 analogue using bipyridine-dicarboxylic acid (H₂bpydc) as the linker) - were also prepared as reference benchmarks.

3.2 Results and discussion

This section is divided into subsections based on key characteristics of COK-47 such as its physical and optoelectronic properties, followed by the exploration of its photocatalytic performance towards dye degradation with an in-depth view on the underlying degradation mechanism. Finally, this section concludes with a study of stability and reusability of COK-47 over multiple photocatalytic cycles.

3.2.1 Structural and optoelectronic characterization

All materials were characterized with regard to their structural, chemical, and optoelectronic properties via techniques including X-ray diffraction (XRD), Fourier transform infrared (FTIR), transmission electron microscopy (TEM), and diffuse reflectance spectroscopy (DRS). Figure 3.2a shows the XRD pattern of the as prepared COK-47. We observe its three characteristic peaks – with the first peak corresponding to the interlayer spacing of ~1.5 nm – in line with the length of the bpdc²⁻ linker as shown in Figure 2.2a inset. Figure 3.2b shows the FTIR spectrum of COK-47 revealing peaks corresponding to carboxylate groups at 1572, 1506, and 1416 cm⁻¹, along with the fingerprint region matching well with reported literature.^{81,82} The TEM image of

the as-prepared COK-47 shows nanocrystals with an estimated size of ~10 nm in each dimension. Bright areas of each individual particle correspond to the layered SBU, while lighter areas – to the bpdc²⁻ linkers connecting them. Using the provided scalebar, the distance between two bright layers can be estimated as ~1.5 nm (Figure 3.2c), further complementing the XRD data. UV-Vis (DRS) spectra of pristine COK-47 shows an absorption edge at 450 nm, corresponding to a bandgap value of 2.7 eV – as calculated from the Tauc-function plot in Figure 3.2d.

TGA analysis was further used to understand the thermal stability and decomposition temperature of the as-synthesized COK-47 MOF. Figure 3.2e shows the weight loss curve in synthetic air atmosphere. We see an initial weight loss of ~5 wt% between 30-200 °C corresponding to the loss of solvent trapped (physi- and chemisorbed) in the pores. Following this, between 400 and 500 °C, we observe a major weight loss of ~60 wt% in synthetic air which corresponds well to the mass fraction of the ligand in the structure. This oxidative decomposition results in the formation of TiO₂, verified using XRD analysis of the post TGA sample.⁸² Based on the molecular weight of COK-47, assuming the formula Ti₂O₃(C₁₄H₈O₄) proposed in literature, we obtain it to be 383.94 g mol⁻¹.⁸² This value when subtracted from the molecular weight of the final product (TiO₂) corresponds to the theoretical weight loss upon decomposition, assuming a defect-free COK-47 structure. Based on Equation 3.1, we estimate the total weight loss to be ~58 wt% after the full conversion into TiO₂ when annealed in synthetic air. Therefore, the observed weight loss of ~60% (in synthetic air) between 400 and 500 °C strongly implies the presence of excess ligands, which we believe are present on the surface of COK-47 nanocrystals as surface passivation, accounting for the higher ligand:Ti ratio.

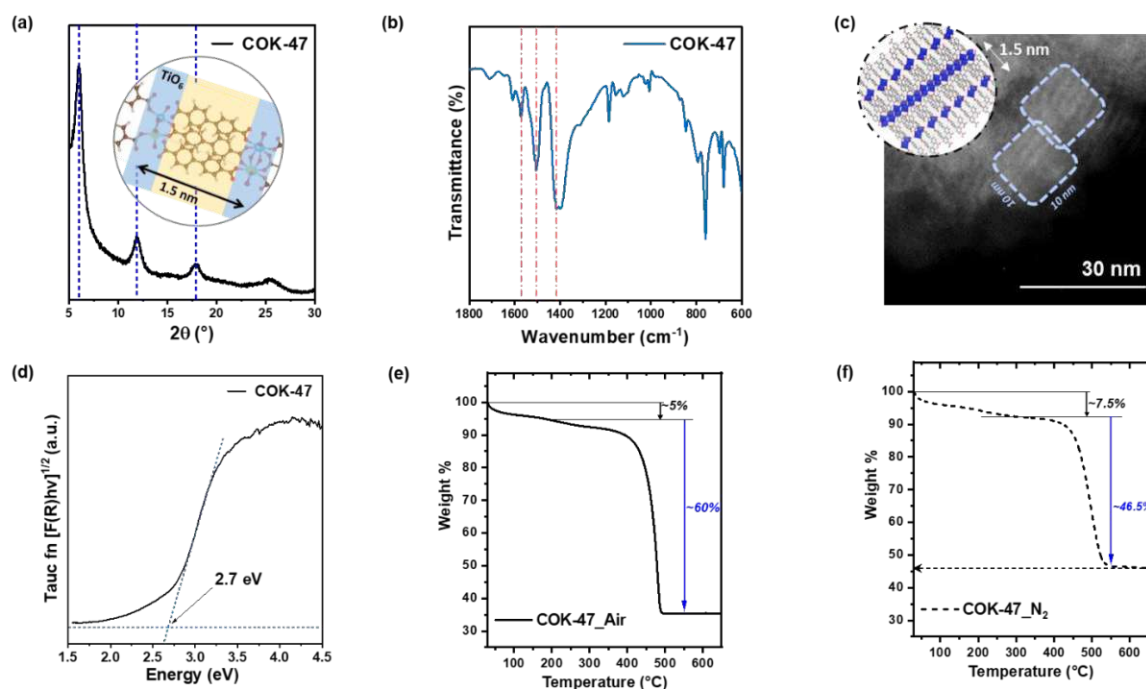
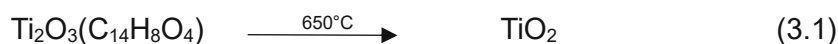


Figure 3.2 (a) XRD pattern of pristine COK-47 nanoparticle (inset: illustrative model showing the distance of one ligand between two SBU layers) (b) FTIR spectra (c) high resolution TEM image (d) Kubelka-Munk analysis plot, of the as prepared COK-47 (e) TGA curve of pure COK-47 in synthetic air atmosphere (f) and N₂ atmosphere

All the above characterizations confirm a successful synthesis of the desired COK-47 nanoparticles and suggests that the surface of COK-47 nanoparticles is terminated with undercoordinated ligands.

3.2.2 Adsorption studies

Typically, a photocatalytic dye degradation test involves two stages: first, adsorption (equilibration) stage, where in the absence of illumination the dye is adsorbed onto the surface/pores of the material; second, photocatalytic degradation stage, where under illumination the photogenerated charges create reactive oxygen species or directly interact with the adsorbed dye, resulting in its degradation. Both stages and their understanding play key roles in the evaluation of the photocatalytic activity of an active compound. Since the first stage is especially important for porous materials, such as MOFs, we first evaluate the adsorption performance of pristine COK-47.

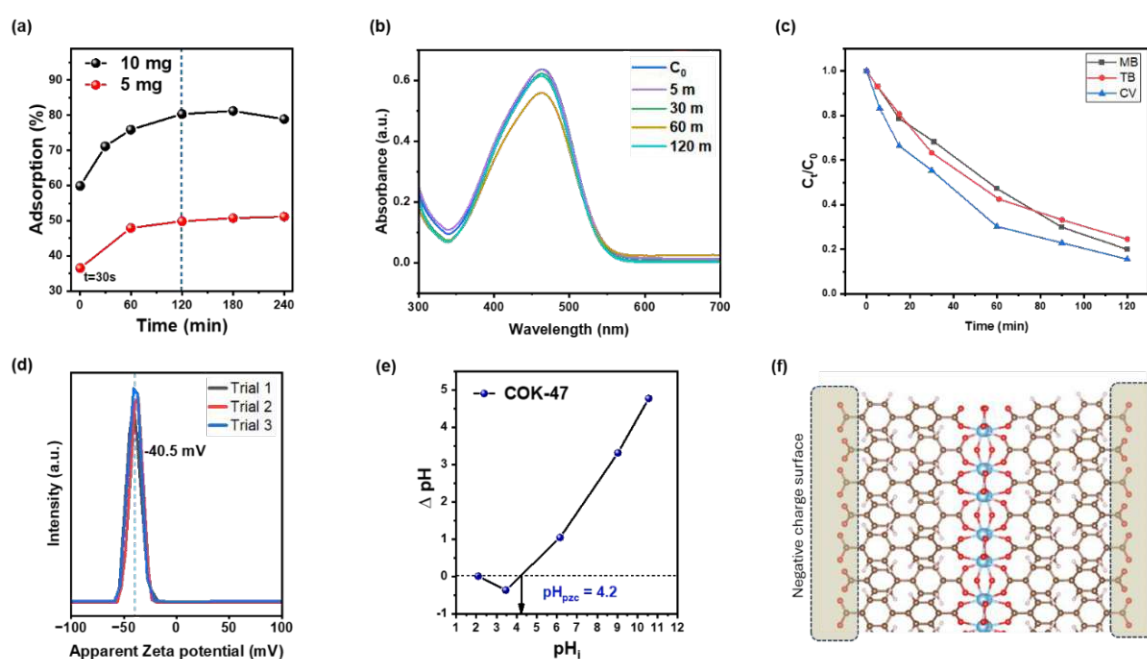


Figure 3.3 (a) Methylene blue adsorption profiles for 4 h, using two different loadings of COK-47 powder (b) UV-Vis spectra of methyl orange solution over the course of 2 h (c) methylene blue, toluidine blue, and crystal violet degradation profiles using COK-47 under visible light illumination (d) Zeta potential measurements of pristine COK-47 particles suspended in water (pH = 7) (e) PZC calculations showing measuring isoelectric point of COK-47 suspension (f) Model schematic showing an isolated edge of COK-47 nanoparticle terminated via free bpdc²⁻ ligands.

In our adsorption tests, we measure the amount of MB adsorbed onto the surface of COK-47 over the course of 4 h, in the absence of light. Figure 3.3a shows an initial increase in the MB adsorption profile corresponding to a strong adsorption of (~30% of the initial dye concentration) in the first minute of mixing, followed by stable MB concentration attained in the solution after 2 h of mixing. Therefore, for all experiments we fixed the equilibration phase to 2 h before subjecting the suspension to light illumination. Based on the initial amount of dye in the solution and the final MB concentration in the solution we determined the total amount of dye adsorbed by 10 mg of COK-47 powder to be ~1 mg. These results show that COK-47 has an overall adsorption capacity of ~100 mg g⁻¹, making it an intermediately strong adsorbent in comparison to other MOFs (Table 2.1). To further complement this observation, we calculated the maximum amount of MB adsorption possible as follows considering a monolayer adsorption model. Using the reported surface area for COK-47 nanoparticles and the

Table 3.1 Overview of the adsorption capacity (Q_e) values for a variety of MOFs reported previously towards dye adsorption in comparison to current work.

MOF	Pollutant	Q_e (mg g ⁻¹)	Equilibrium time	Pollutant concentration (ppm)
COK-47 ^{This work}	MB	100.5	60 min	25
UiO-66-Zr ³	MB	81	200 min	50
Zr-BDC-CP ⁴	MB	39	5h	25
MIL-100(Fe) ⁵	MB	736.2	-	60
MIL-100(Cr) ⁵	MB	645.3	-	25
HKUST-1	MB	123	-	50
MOF-235 ⁶	MB	187	80 min	25
Fe-BDC ⁷	MB	8.65	90 min	5
UiO-66-Zr ⁸	AR	400	90 min	50
Cu-BTC ⁹	MB+MO+RhB	39.5	30 min	100
Ni(BIC)₂·2.5H₂O ¹⁰	MB	15.5	60 min	5
MIL-53(Al)-NH₂ ¹¹	MB/MG	45/37.8	60 min	5
MIL-53(Al) ¹¹	MB/MG	3.6/2.9	60 min	5

(interaction) footprint of a single MB molecule to be $\sim(17 \times 7.6 \text{ \AA}^2)$, we obtain values corresponding to a MB coverage by $\sim 2.2 \times 10^{20}$ dye molecules per gram of MOF.⁸⁴ This translates to $\sim 366 \text{ \mu mol}$ (117 mg) of MB and corresponds to $\sim 12 \text{ wt\%}$ adsorption capacity of the MOF surface – value that is similar to the one observed experimentally. Further extending these adsorption studies to other dyes such as TB, CV, and MO – we observed a similarly strong uptake of TB and CV, however, interestingly, no adsorption was observed in the case of methyl orange (Figure 3.3b, 3.3c). Few studies have also reported a similar behavior, where the MOF showed selective preference towards a set of dye molecules.⁸⁵ To gain some insight into this, we employed surface characterization techniques such as zeta potential and point-of-zero-charge (PZC) measurements to understand the nature of the surface of COK-47 nanoparticles. Zeta potential measurements carried out at pH = 7 – relevant to experimental conditions – show a strong negative surface charge of -40.55 mV (Figure 3.3d). In addition to this, PZC measurements revealed an isoelectric point at pH = 4.2 for COK-47, indicating a negatively charged surface above this pH (Figure 3.3e). Both these findings demonstrate a negatively charged MOF surface, most likely arising from the presence of deprotonated carboxylic groups (COO^-) present in the ligands passivating the MOF nanoparticle (Figure 3.3f). Therefore, considering this negatively charged MOF surface and the ionic nature

of the dyes in question – MB, TB, and CV are all cationic dyes and whereas MO is an anionic dye – we can suggest that electrostatic interaction processes between the dyes and COK-47 dominate in the adsorption. As such, the MO anions are strongly repelled from the MOF surface inhibiting any adsorption whereas the cationic nature of the other dyes aids their adsorption evident from their high uptake values. While the main driving force of adsorption are clearly due to electrostatic interactions, we don't exclude that adsorption can also be aided by the π - π and hydrogen bonding interactions between the bpdc²⁻ ligands and MB molecules, as reported by Ali et al.⁸⁵ Such a selective behavior towards a specific set of dyes is often observed by varying the pH of the solution and thus changing the surface chemistry of the photocatalyst⁸⁶, however the ability of COK-47 to selectively interact to positively and negatively charged pollutants in neutral aqueous media is noteworthy.

3.2.3 Photocatalytic degradation results

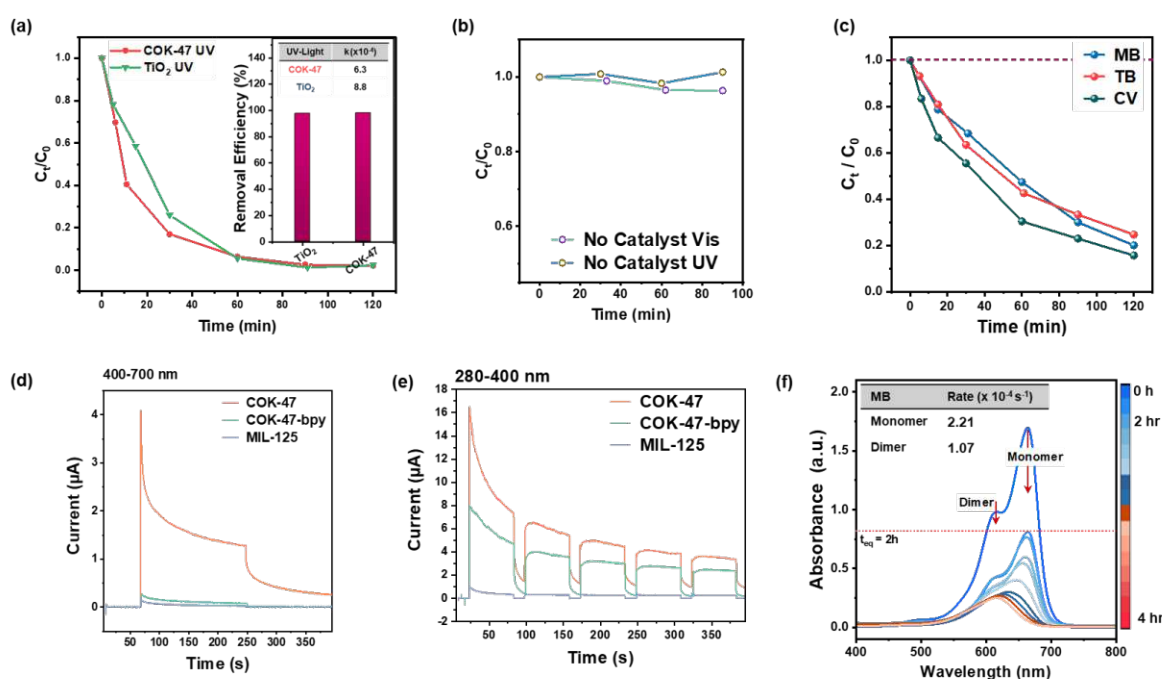


Figure 3.4 (a) Methylene blue concentration profiles for 2 h, using two different adsorbents, COK-47 and TiO₂, under UV (200-400 nm) illumination (inset: overall removal efficiency and the corresponding degradation rates) (b) concentration profiles of MB solution under UV and visible illumination in the absence of COK-47 (c) MB, TB, and CV concentration profiles using COK-47 under visible light illumination (d) chopped light chronoamperometry showing photo-response of COK-47, COK-47-bpy, and MIL-125 under visible and (e) UV illumination (f) UV-Vis spectra of methylene blue degradation on COK-47 under visible light illumination (inset table showing the degradation rates of the MB₁ and MB₂).

Moving on to the photocatalytic dye degradation tests (stage 2), COK-47 was tested under both UV (200-400 nm) and visible (400-700 nm) illumination. We first carried out a set of reference experiments with MB solutions in the absence of COK-47 to reveal any inherent photodegradation processes, such as photobleaching, that might contribute to the overall photodegradation performance of the MOF. Figure 3.4b shows that there is no change in the MB concentration when illuminated under UV and visible light, in the absence of any catalysts. Additionally, we also benchmarked the performance of COK-47 with TiO₂ and MIL-125, two of the most widely studied materials in the community.

When tested under UV illumination, we observed a similar degradation performance of COK-47 and TiO₂, with both achieving an overall removal efficiency of ~98% after 2 h of illumination. Figure 3.4a shows the MB concentration profiles of COK-47 and TiO₂, where we observe both catalysts to have a comparable rate of degradation of 6.3×10^{-4} and $8.8 \times 10^{-4} \text{ s}^{-1}$, respectively, with almost 100% dye removal efficiency (Figure 3.4a inset). Figure 3.4b shows the degradation profile using COK-47 under visible light illumination and displays its excellent dye removal efficiency of 80 % along with degradation rates reaching as high as $2.21 \times 10^{-4} \text{ s}^{-1}$. COK-47 outperforms both TiO₂ and MIL-125 which have degradation rates an order of magnitude slower and a removal efficiency of ~1% and 18%, respectively. Figure 3.4c compares the dye concentration profiles for MB, TB, and CV using COK-47 as a photocatalyst under visible-light and demonstrates that COK-47 achieves similarly excellent removal efficiencies and high degradation rates for all three cationic dyes irrespective of their structure (Table 2.2). Once again, in line with our adsorption studies, we observe no degradation or change in the MO concentration profiles as expected from the strong repulsion between the dye and the MOF surface.

Table 3.2 Photocatalytic degradation rates and removal efficiencies of various cationic dyes using COK-47 under visible light illumination

Dye	Degradation Rate ($\times 10^{-4} \text{ s}^{-1}$)	Removal Efficiency (%)
MB	2.2	80
TB	2.1	75
CV	2.7	85

To provide more details on the activity difference between COK-47 and its benchmark MOF MIL-125, we measured the photocurrent response of each of the materials under visible and UV light using chopped light chronoamperometry. Figure 3.4d shows that COK-47 shows the highest photocurrent response of an initial value of ~3.5 μA reaching a stable value of 1.3 μA . This value is almost 36 times higher than that of MIL-125, which is expected mostly due to limited absorption of MIL-125 in the visible region. In the case of UV-illumination, however, COK-47 once again shows the highest photocurrent response which in this case can be direct evidence for its better charge separation/extraction due to its 2D SBU structure. In comparison to COK-47, MIL-125 has an isolated 0D SBU node structure strongly limiting its photoconductivity, as shown in Figure 3.4e. These results once again highlight the benefit of the interconnected 2D SBU in the COK-47 framework.

In addition to the excellent dye degradation performance of COK-47 under visible light, upon close inspection we observe a strong blue shift in the overall MB absorption spectrum over the course of degradation, as shown in Figure 3.4f. Methylene blue is known to form aggregates in solution, often displaying a blue shifted (hypsochromic) absorption.⁸⁷ First we deconvoluted this spectrum into its individual components. Based on literature, the absorption maximum at 664 nm and 612 nm correspond to the presence of monomeric (MB₁) and dimeric (MB₂) forms of methylene blue in the solution. Figure 3.5a-3.5b shows the rate of degradation calculated for each of the maxima values. We observed two different degradation rates for MB₁ and MB₂ of 2.21×10^{-4} and $1.07 \times 10^{-4} \text{ s}^{-1}$, respectively. Additionally, the MB₂ concentration profile plateaus after the first 90 mins, whereas MB₁ concentration continues to decrease. This behaviour was also observed for other metachromatic cationic dyes tested – TB and CV – as shown in Figure 3.5c-3.5d.⁸⁸⁻⁹⁰ Similar behaviour was also observed by Kojima et al. and

Shivatharsiny et al. while testing the photocatalytic performance of WO_3/TiO_2 hybrids and $\text{SnS}_2/\text{TiO}_2$ hybrids, respectively, for photodegradation of methylene blue, which they proposed could be due to interactions between the N-demethylation products and the dye molecules.^{91,92} Building on this, we also believe the strong π - π interactions between the dimers and some of the demethylated products makes it difficult to degrade the dye in its dimeric form.

3.2.4 Photocatalytic degradation mechanism study

Since we observe a strong interaction between the surface of COK-47 and dye molecules, the overall degradation mechanism can occur in a few different ways. First, the dyes can directly react with the photogenerated holes located on the linker molecules, thereby getting converted into oxidized products or radicals; or second the photogenerated holes/electrons react with H_2O (OH^\cdot) or O_2 present in the solution, thus producing reactive oxygen species (ROS), such as $\text{O}_2^{\cdot-}$ and $^\cdot\text{OH}$. These ROS can then react with the surface adsorbed dye molecules resulting in their degradation.^{93,94} Elucidating the degradation mechanism of a photocatalytic process is a very important part of our investigation as it can hint at advantages or limitations of the COK-47 and give directions to its structural optimization. In order to provide such insights, various scavengers are added to the photodegradation experiment where they react and quench the produced ROS or other active species thereby inhibiting the dye degradation.

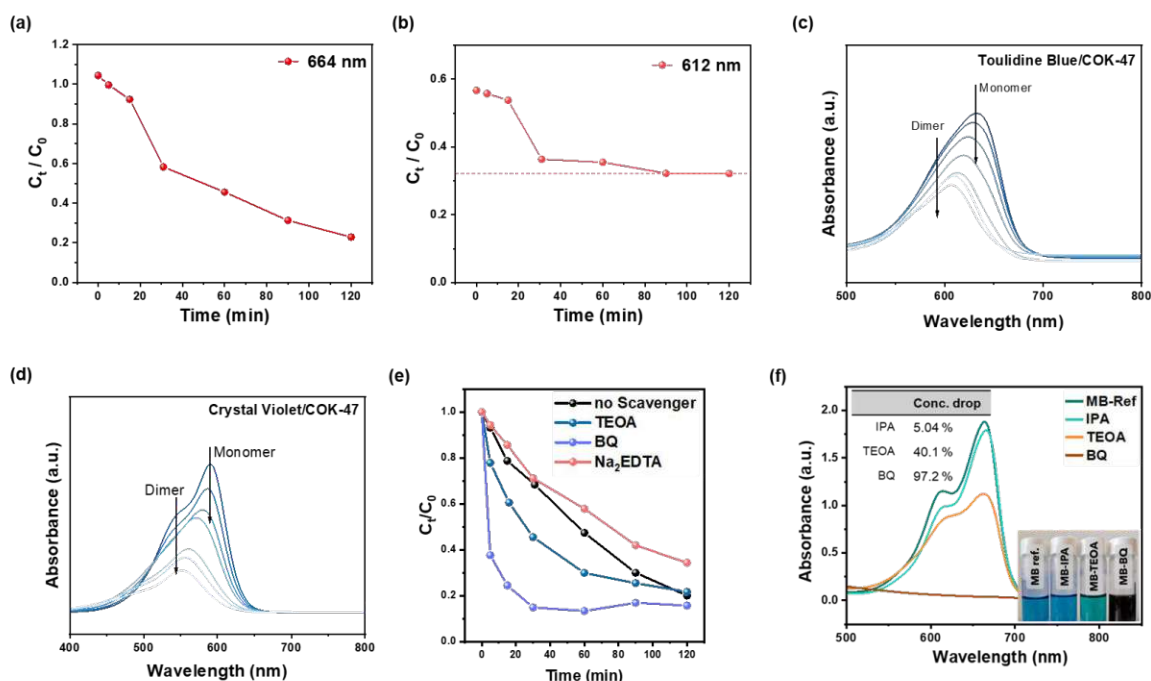


Figure 3.5 (a) Degradation profile of MB₁ and (b) MB₂ using COK-47 under visible light illumination (c) absorption spectrum of toulidine blue and (d) crystal violet, both cationic dyes also showing a hypsochromic shift during the degradation process (e) MB concentration profiles using COK-47 in the presence and absence of ROS scavengers (f) absorption spectrum of MB solutions after illumination in the presence of scavengers

Figure 3.5e shows the MB concentration profiles during a typical dye degradation process for 2 h of visible light illumination in the presence of these scavengers. In contrary to our expectations, we observe a ~1.5 and ~2.4-fold increase in the degradation rates when MB-MOF suspension was irradiated in the presence of BQ and TEOA, respectively, suggesting a degradation enhancement effect. We believe BQ[·] radicals formed additionally can react with the dye molecules via a different oxidation pathway leading to the increased degradation rate. Similarly, TEOA can also act as an excellent hole scavenger from COK-47 thereby improving

the overall charge separation which leads to the generation of long-lived electrons. These electrons can further react with $\text{H}_2\text{O}/\text{O}_2$ present in the solution producing ROS that ultimately react with the dye molecules. While these hypotheses can be in part true, reference experiments carried out using BQ and TEOA in the absence of COK-47 also showed MB degradation. Figure 3.5f clearly shows that when BQ or TEOA are illuminated in presence of MB, clear photochemical transformation and solution color change take place,⁹⁵ which ultimately makes these widely used scavengers unsuitable for our investigations. In order to address this gap, we switched to chloroform (CHCl_3) and disodium ethylenediaminetetraacetic acid (Na_2EDTA) known for their ability to scavenge $\text{O}_2^{\cdot-}$ and h^+ selectively.^{96,97} CHCl_3 and IPA did not show any direct interaction with MB under illumination making them suitable for our mechanistic studies, Na_2EDTA was able to slowly degrade MB under visible light illumination.^{98,99}

Based on the above observations we decided to only use IPA and CHCl_3 as scavengers. Figure 3.6a shows the MB degradation profiles in the presence of IPA showing a slight decrease in the overall degradation rate from $2.21 \times 10^{-4} \text{ s}^{-1}$ to $2.1 \times 10^{-4} \text{ s}^{-1}$ and a negligible difference in the overall dye removal efficiency. This indicates that $\cdot\text{OH}$ radicals play a minor role in the degradation mechanism. In contrast to this, when using CHCl_3 we observe a strong decrease (~ 3.8 times) in the overall degradation rate and dye removal efficiency. This demonstrates that $\text{O}_2^{\cdot-}$ are the ROS responsible for the MB degradation. Since CHCl_3 is largely immiscible with water (lower polarity), it can form a layer around the MOF surface readily scavenging the $\text{O}_2^{\cdot-}$ radicals formed from the dissolved O_2 .

Scavenger experiments described above help to shed light on the mechanism of dye degradation, however, they only reveal the most likely and active form of the redox species taking part in the degradation process. Taking one step back, we also believe the electron/hole separation efficiency could be another strong factor related to the excellent photodegradation performance for COK-47 and defining the absolute number of electrons and holes able to create these redox species, i.e. $\text{O}_2^{\cdot-}$ radicals. To test this hypothesis and study efficiency of charge separation, we prepared a COK-47 analogue, namely COK-47-bpy, using the H_2bpydc instead of the standard H_2bpdc . The resultant MOF has the same structural and compositional properties to its pristine form, with a slightly lower bandgap due to the presence of pyridinic groups in the MOF. However, photocatalytic degradation testing under visible light revealed a

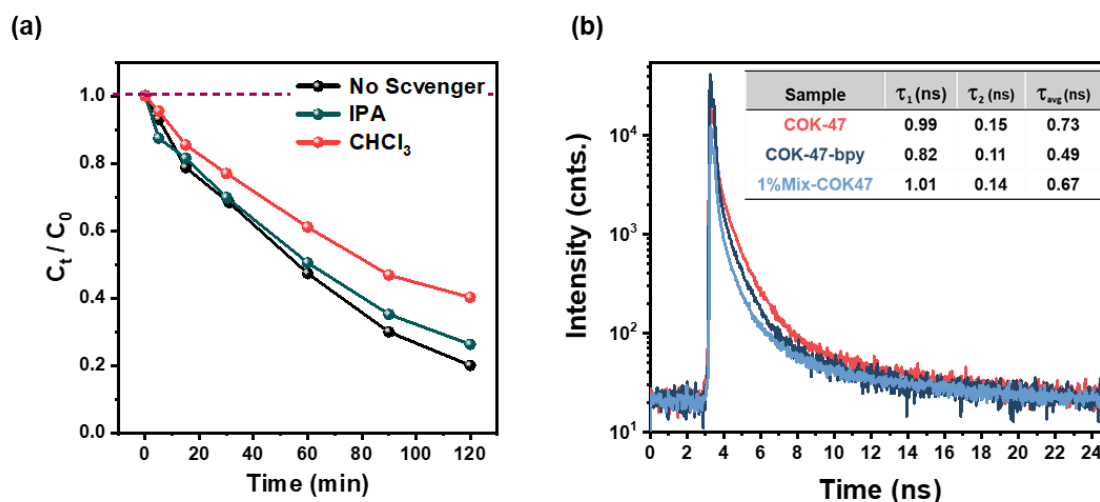


Figure 3.6 (a) Degradation profile of MB on COK-47 in the presence of oxygen radical and OH radical scavengers via CHCl_3 , and IPA, respectively. (b) Time-resolved emission spectra of pristine COK-47 (orange), COK-47-bpy (dark blue), and 1mol% bpydc²⁻ COK-47 (pale blue).

35% lower performance in comparison to COK-47. Similar to the case of MIL-125, Figure 3.4d-3.4e shows complementary photocurrent measurements and demonstrate a much lower photocurrent response of COK-47-bpy (compared to COK-47) under both UV and visible light illumination, suggesting a weak charge extraction in the presence of bpydc²⁻ ligands. This is further corroborated by the time-resolved emission spectroscopy (TRES) measurements where COK-47-bpy shows a 30 % lower carrier lifetime as compared to COK-47, reflecting the enhanced electron-hole recombination caused by the presence of -N- moiety in the ligand (Figure 3.6b).

3.2.5 Stability and reusability

For a long time, aqueous stability has been an overarching problem for MOFs, in which the aqua ligands attack the SBU center replacing the coordinated carboxylates, resulting in structural breakdown. Additionally, photoexcitation often adds to the problem since the photogenerated electrons are transferred from the ligand to the metal leaving behind a hole which, if not consumed, can readily oxidize the ligand also resulting in facilitated breakdown of the ligand-SBU bonding. Therefore, water- and photo-stability are of critical importance for MOFs especially in applications like photocatalysis and wastewater treatment.

Figure 3.7a shows the degradation rates and overall removal efficiency of MB over multiple cycles. Each measurement involved recovering, drying, and resuspending the MOF particles in a fresh MB solution for each cycle. COK-47 shows a stable degradation rate over 3 cycles, with a consistent removal efficiency of ~80 %. Figure 3.7b shows the XRD pattern of COK-47 before and after undergoing multiple photocatalytic cycles. Both XRD patterns match well without showing any peak shift or the appearance of any new peaks in both the MB-saturated-

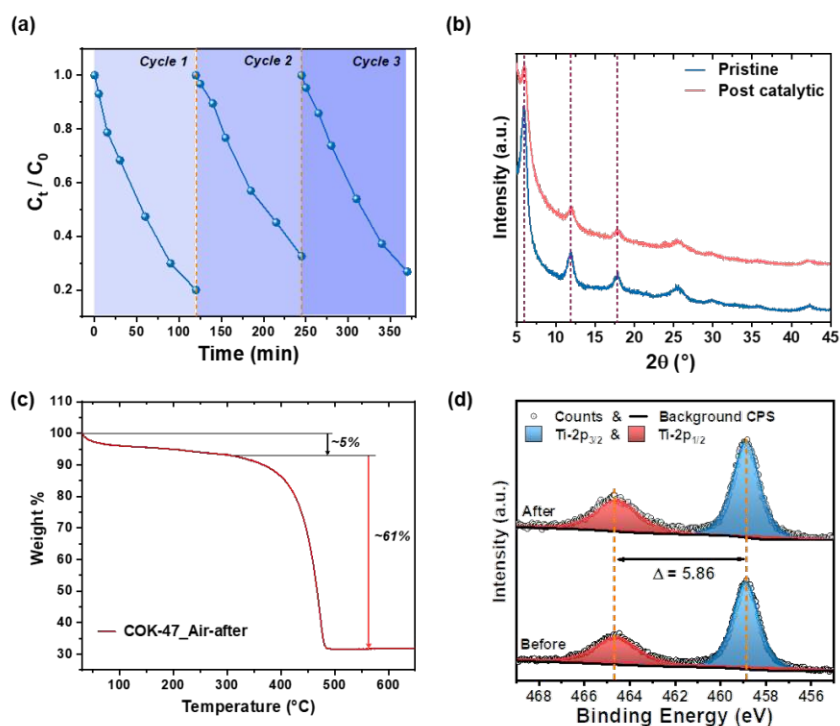


Figure 3.7 (a) MB concentration profiles for 3 cycles showing the recyclability and stability of COK-47 under reaction conditions (b) XRD pattern of COK-47 before and after photocatalytic degradation of MB (c) TGA curves showing weight loss of COK-47 after a single MB degradation cycle, in air and N_2 (d) XPS spectra of the Ti 2p edge of COK-47 before and after multiple photocatalytic degradation reactions.

COK-47 and post catalytic COK-47, indicating that neither strong dye adsorption nor the photocatalytic testing causes any changes in the structure of COK-47. Subsequently, complementary total reflection X-ray fluorescence (TXRF) and thermogravimetric measurements were performed on post-catalytic MOFs to verify whether any MOF degradation occurred, potentially resulting in the leaching of Ti ions and/or organic ligands into the solution. TXRF analysis shows a negligible amount of titanium – ~0.003% of the original content – present in the solution after 3 cycles of MB degradation. Similarly, Figure 3.7c shows the TGA curves corresponding to COK-47 after photocatalytic tests. We observe a similar weight loss of ~61 wt% as compared to the pristine COK-47. Both these results combined indicate that the overall composition of the MOF has not changed after the experiment. Additionally, absence of any additional weight loss (organic content) at lower temperatures or in the overall value strongly indicates that there is no adsorbed MB or its degraded components on the surface of the MOF particle.

Lastly, XPS analysis was used to identify any chemical changes that might occur in the oxidation state of the MOF after catalysis. Figure 3.7d shows the Ti 2p signal of COK-47 before and after the reaction. The lack of change in the XPS signal indicates that the titanium within the COK-47 framework remains unaffected by the repetitive catalytic processes, thus confirming the MOF's chemical stability. These datasets combined show the resilience and efficiency of COK-47 in these photocatalytic processes commending it as a promising candidate for various environmental and industrial applications via visible-light-driven purification methods.

3.3 Conclusion

To summarize, in this chapter a Ti-based MOF, namely COK-47, was studied as an OIH photosystem for its potential in visible light driven wastewater treatment via dye degradation. Photocatalytic experiments showed an excellent photodegradation performance in both UV and visible light illumination, outperforming other Ti-based systems such as TiO₂ and Ti-MIL-125 by an order of magnitude higher degradation rates in visible light conditions. This performance was attributed to the improved charge separation and lower bandgap due to the 2D-SBU and small nanoparticle size, respectively. The study also reveals the selective nature of COK-47 towards specific pollutants which is mainly attributed to the negatively charged surface (attracting positively charged pollutants like MB) resulting in an electrostatic driven interaction between the pollutant molecules and MOF surface. However, this interaction allows COK-47 to have a moderately high adsorption capacity as compared to some of the other MOF based OIH systems despite its relative low surface area. The study further explores the possible degradation mechanism via a set of scavenger-based experiments revealing O₂ radicals as the majority ROS responsible for degradation. Finally, COK-47 also shows reusability, structural and chemical stability over multiple photodegradation cycles without any loss in performance.

3.4 Experimental section

3.4.1 Synthesis and characterization

COK-47 was prepared according to the previously reported procedure. Briefly, 242 mg of biphenyl-4,4'-dicarboxylic acid (H₂bpdc) (1 mmol) were suspended in a volumetric 1:9 mixture of HPLC-grade methanol and absolute dimethylformamide. The vial was flushed with argon and the sonicated for 10 minutes. To this suspension, 148 μ L (0.5 mmol) of titanium tetraisopropoxide (TTIP) were added under argon. The reactor vial was then closed, and the suspension stirred for 2-3 min. Subsequently, the reactor was heated to 150 °C using

microwave irradiation for 1 h with 600 rpm stirring. After rapid cooling to ~55 °C, the product was filtered from the reaction medium by vacuum filtration and washed six times, thrice with 30 mL DMF and thrice with 30 mL methanol. The filtered powder was then pre-dried under a vacuum at 100 °C for 30 m, followed by milling and drying at 150 °C overnight, under vacuum. COK-47-bpy was prepared in a similar fashion, however, instead of H₂bpdc – same molar concentration of H₂bpydc was used as a linker molecule.

MIL-125 was prepared according to a previously reported solvothermal synthesis.¹⁰⁰ Briefly, 1 g (6 mmol) of terephthalic acid was added to a solution mixture of 2 mL HPLC-grade methanol and 18 mL absolute DMF in a 45 mL Teflon-lined autoclave, the reactor was then thoroughly flushed with argon. After 50 min of stirring, 568 µL TTIP (1.9 mmol) was added under an argon atmosphere. The reaction mixture was sonicated for 3 minutes and additionally stirred for 30 min. It was then heated to 150 °C for 18 h. After naturally cooling down to room temperature, 60 mL DMF was added to the mixture, and sonicated for 10 min. The product was separated via vacuum filtration and washed 3 times with 20 mL methanol respectively, and vacuum dried at 150 °C.

3.4.2 Standard calibration curve

UV-Vis absorption was used to accurately quantify the amount of dye in the solution. For this, calibration curves were made by measuring the absorption peak intensities, for each of the dye molecules, for a set of known concentrations in the range of 0.5 to 10 ppm. For homogeneity, each of these solutions was prepared by diluting a 50 ppm stock solution. A linear regression fit was made from the measured data points providing a standard curve equation that was used to estimate the dye concentration for all the photodegradation experiments.

3.4.3 Figure of merit

Throughout this study, the overall removal efficiency and degradation rates were used as a figure of merit to rank and compare different catalyst materials.

The overall removal efficiency was calculated according to the following formula,

$$Efficiency(\%) = \left(\frac{C_0 - C_t}{C_0} \right) * 100$$

Where, C₀ and C_t are the MB concentration right before the illumination and at any time t during illumination, respectively.¹⁰¹

Degradation rates and kinetic constants were calculated assuming the degradation followed either first, second or third order, depending on the shape of the degradation curve.

Reactions of the first order can be described using the following equation.

$$C_t = C_0 \cdot e^{-kt}$$

Here, the kinetic constant k was then calculated by plotting ln(C₀/C_t) against time (in seconds) and fitting a linear function with a fixed y-intercept at 0 to the data points.¹⁰²

Reactions of second order can be described using the following equation.

$$\frac{1}{C_t} = \frac{1}{C_0} + kt$$

For those reactions, the kinetic constant was calculated by plotting $\frac{1}{C_t} - \frac{1}{C_0}$ (C in mol L⁻¹) against the reaction time (in seconds). Reactions of third order can be described with the following equation.

$$\frac{1}{C_t^2} = \frac{1}{C_0^2} + 4kt$$

For those reactions, the kinetic constant was calculated by plotting $\left(\frac{1}{C_t} - \frac{1}{C_0}\right)\frac{1}{4}$ (C in mol L⁻¹) against the reaction time (in seconds).

3.4.4 Photocatalytic dye degradation setup

Each experiment was carried out in a homemade slurry-type reactor equipped with a water-cooling jacket. A 200 W lamp (Lumatec SUV-DC-E) was used for illumination with a fixed illumination distance of 8.6 cm with an intensity of 32.8 mW cm⁻² for visible light (400-700 nm) and 17.2 mW cm⁻² for UV-light (240-400 nm). Briefly, 10 mg of the pristine catalyst was suspended in 25 mL of deionized water and sonicated for 15 minutes to obtain a homogeneous suspension. This suspension was then transferred into the reactor and mixed with 25 mL of 50 ppm dye solution, leading to an overall methylene blue concentration of 25 ppm in the final solution. After mixing, immediately, the first sample of 2 mL was taken, followed by an "equilibration phase" of stirring in the dark for two hours to reach a dye-adsorption-maximum. Following this, another 2 mL sample was taken, and the solution was illuminated for 2 h. During the "illumination phase", 2 mL samples were taken after 5, 15, 30, 60, 90, and 120 min of illumination. The solution was then separated from the catalyst by centrifugation, and the concentration of methylene blue was measured using UV-Vis spectroscopy. The characteristic peak intensities of methylene blue (MB), crystal violet (CV), toluidine blue (TB), and methyl orange (MO) at 664, 590, 630 and 464 nm, respectively were used to evaluate the photocatalytic degradation performance of each of the materials. The reaction temperature was maintained at 15°C throughout the experiment under constant stirring of 200 rpm.

3.4.5 Mixed dye adsorption studies

Briefly, 25 mL solution of 50 ppm methylene blue was mixed with 25 mL of 50 ppm methyl orange and stirred for 30 min. After mixing, the solution was filtered to remove any particles formed due to electrostatic attraction between the two dyes, yielding a homogeneous green (~6 ppm) MB/MO solution. From this, 25 mL of the solution was mixed with 25 mL of pre-sonicated COK-47 suspension in water (0.2 mg mL⁻¹). The first sample for UV-Vis analysis was taken 30 s after mixing, followed by sampling at 5, 15, 30, 60, 90, and 120 min. Each sample was then centrifuged at 5600 rpm for 20 min, followed by UV-Vis measurement to determine the dye concentration.

3.4.6 Point-of-zero-charge (PZC) measurements

To determine the PZC, five 0.1 M KNO₃ solutions, adjusted to different pH points using solutions of 0.1 M HCl and 0.1 M KOH, were prepared and measured with a pH meter. Briefly, 10 mg of MOF powder was dispersed in 15 solutions via ultrasonication for 10 min. following this, the homogeneous suspensions were stirred for 24 h at 500 rpm under dark to allow equilibration between the adsorption-desorption of the protons on the surface of the MOF. Next, 10 mL of the solution was centrifuged at 5600 rpm for 15 min. The pH of the supernatant was determined using a pH meter. The difference between the initial and the final pH of the solution was plotted against the initial pH to determine the point-of-zero charge.

3.4.7 Zeta potential measurements

Zeta potential measurements were carried out using water as a solvent. Briefly, 10 mg of powder was suspended in de-ionized water via ultrasonication for 10 min. Each measurement consisted of ~12 to 15 runs to obtain a stable value that is in good agreement with the model and had a standard deviation of less than 10%.

3.4.8 Photoelectric test setup

Electrode preparation: Briefly, FTO glass electrodes ($\sim 3 \times 1 \text{ cm}^2$) were ultrasonicated for 15 min each in soap solution, DI water, and finally with EtOH, to obtain clean surfaces for drop casting. These electrodes were then dried at 60 °C and masked at top $1 \times 1 \text{ cm}$ using Kapton tape, 30 min before use. Simultaneously, 10 mg of catalyst powder was dispersed in 200 μL of isopropanol solution via ultrasonication for 10 min. Following this, $\sim 80 \mu\text{L}$ of this homogeneous suspension was drop-casted onto the masked FTO electrodes and allowed to dry at RT followed by drying at 60 °C for 30 min. The total electrode area covered with catalyst material was $2 \times 1 \text{ cm}^2$.

Chopped light-chronoamperometry tests: These tests were carried out in a single gas-tight cell using catalyst on FTO glass, Pt plate, and Ag/AgCl (in 3 M KCl) as the working, counter, and reference electrode respectively, dipped in 0.1 M K_2SO_4 electrolyte solution. The solution was purged with N_2 for 1 h before testing. Chronoamperometry tests were done at 0 V vs. the open circuit potential (OCP) with multiple light on–off cycles with an illumination ranging from 280–400 nm (UV) or using 400–700 nm (visible) in the case of each sample. Each illumination cycle included a light “on” for about 60 s followed by 15 s of no illumination.

Chapter 4: MOCHAs: Ag-based OIHs as co-catalysts for photocatalytic H₂ production

This chapter introduces and studies a set of class D hybrids, called Ag-MOCHAs, previously reported for their performance in electrocatalytic syngas production (CO+H₂) via CO₂ reduction. In our study, we benchmark its performance as a photocatalytic hydrogen production catalyst using two different light absorption strategies described in section 4.1, along with a series of experimental and characterization techniques to understand the underlying processes.

The work presented in this chapter has been published as a research article titled “MOCHAs: An Emerging Class of Materials for Photocatalytic H₂ Production” in the journal *Small* from Wiley with DOI number of [10.1002/sml.202400348](https://doi.org/10.1002/sml.202400348).

My contributions as the first author include the initial ideation and proof-of-concept experiments followed by experimental design, testing and data analysis, and finally, summarizing the overall results and paper writing. I would also like to mention that this work was carried out in continuation to the aforementioned report on the facile microwave assisted synthesis of MOCHAs and their application in electrocatalytic syngas production carried out by Hannah Rabl (co-author and colleague) published in *Communications Chemistry* in 2023.⁴⁴

RESEARCH ARTICLE

small
www.small-journal.com

MOCHAs: An Emerging Class of Materials for Photocatalytic H₂ Production

Stephen Nagaraju Myakala, Hannah Rabl, Jasmin S. Schubert, Samar Batool, Pablo Ayala, Dogukan H. Apaydin,* Alexey Cherevan,* and Dominik Eder

Production of green hydrogen (H₂) is a sustainable process able to address the current energy crisis without contributing to long-term greenhouse gas emissions. Many Ag-based catalysts have shown promise for light-driven H₂ generation, however, pure Ag—in its bulk or nanostructured forms—suffers from slow electron transfer kinetics and unfavorable Ag–H bond strength. It is demonstrated that the complexation of Ag with various chalcogenides can be used as a tool to optimize these parameters and reach improved photocatalytic performance. In this work, metal-organic-chalcogenolate assemblies (MOCHAs) are introduced as effective catalysts for light-driven hydrogen evolution reaction (HER) and investigate their performance and structural stability by examining a series of AgXPh (X = S, Se, and Te) compounds. Two catalyst-support sensitization strategies are explored: by designing MOCHA/TiO₂ composites and by employing a common Ru-based photosensitizer. It is demonstrated that the heterogeneous approach yields stable HER performance but involves a catalyst transformation at the initial stage of the photocatalytic process. In contrast to this, the visible-light-driven MOCHA-dye dyad shows similar HER activity while also ensuring the structural integrity of the MOCHAs. The work shows the potential of MOCHAs in constructing photosystems for catalytic H₂ production and provides a direct comparison between known AgXPh compounds.

4.1 Introduction

Ag NPs have been an extensively studied co-catalyst for various photocatalytic applications like H₂ production, CO₂ reduction, wastewater treatment, and many more.^{103–105} However, they often suffer from sluggish interfacial charge transfer arising from strong electron trapping and a relatively weak Ag-H bond (i.e. weak H adsorption), altogether diminishing their photocatalytic efficiency.^{106,107} Several attempts have been made to improve its performance by either modifying the pristine metallic Ag NPs or by employing Ag-based complexes as co-catalysts. For example, Choi et al. reported a strong increase in the H₂ production when using an Ag-thiocyanate complex, attributing the better performance to the improved charge transfer kinetics due to the presence of organic ligands.¹⁰⁸ Alternatively, Yu et al. prepared a core-shell architecture by in-situ selenization of silver present on Ag-NP/TiO₂ nanostructures. They observed a threefold increase in their HER performance from these new Ag@AgSe_x core-shell co-catalysts, which they attribute to the increased number of active sites due to the selenization process. Both of these approaches involved preparing a hybrid material by creating a bond between Ag and chalcogens like S and Se, resulting in a boost in the performance. As introduced in section 1.3.2.2, Ag-MOCHAs, specifically mithrene (AgSePh) and thiorene (AgSPh), are a set of layered OIHs consisting of an Ag-chalcogen complex forming a stacked 2D coordination polymer. Considering the aforementioned studies, Ag-MOCHAs can also provide, firstly, improved charge transfer kinetics, and secondly, modularity and fine control over other electronic properties by controlling the organic functional group in the structure, making them an attractive catalyst that can efficiently carry out the hydrogen evolution reaction. AgSePh was the first reported 2D MOCHA, isolated via a reaction of AgCl with PPh₃, in 2002 by Cuthbert et al.¹⁰⁹ Following this, in 2018, Hohman et al. improved upon the synthetic procedure preparing Ag-MOCHAs via two new methods, first a Ag-film tarnishing approach and second a biphasic synthesis approach.¹¹⁰ Both these approaches allowed the authors to thoroughly characterize and explore the structural and optoelectronic properties of this class of materials.¹¹¹ However, the low product yield strongly limited their testing in any applications, as mentioned in section 1.3.2.2. Recently, our group successfully demonstrated the potential of AgSePh and AgSPh for electrocatalytic syngas production, reducing a CO₂/H₂O mixture producing CO and H₂.⁴⁴ Additionally, this work reported a facile microwave assisted synthetic route, avoiding the use of harsh precursors such as benzeneselenol or -thiols in previous reports. Overall, this work was a critical advancement for exploring various applications of Ag-MOCHAs since it not only provides a high yield synthetic route but also hints towards their potential to catalyze hydrogen production. Based on these studies, the strong improvement in the photocatalytic performance in Ag-chalcogen based co-catalysts, AgSePh (mithrene) and AgSPh (thiorene) also make an attractive set of new materials that are yet to be tested as catalysts for photocatalytic H₂ production. In order to do this, the first step involves selecting a good photosensitizer (light absorbing molecules or semiconductor materials) that can harvest light into photogenerated electrons, which can then be used by MOCHAs for H₂ production. Recalling from section 1.2 there are mainly two important aspects of a good photosensitizer – first, strong light absorption to maximize the number of photogenerated charge carries, and second, the interaction between the co-catalyst and photosensitizer, which is important for efficient charge transfer. Typically, sensitization can be achieved via two methods – 1. Homogeneous (using molecular photosensitizers like Ru(bpy)₃²⁺, Eosin Y) photosystems, and 2. Heterogeneous (using solid-state semiconductors like TiO₂, CdS, C₃N₄) photosystems. Typically, Heterogeneous photosystems involve photoactive semiconductors anchored with co-catalysts, linked either via covalent or van der Waals interactions, resulting in a static sensitization process. On the other hand, homogeneous photosystems generally have both

the components (photosensitizer and co-catalyst) of optimized concentrations dissolved in the solution resulting in a dynamic sensitization process. In this work we investigate the photocatalytic behavior of Ag-MOCHAs, denoted as AgXPh where X = S, Se, Te, using both sensitization strategies. The first strategy involves a quasi-homogeneous approach employing a widely studied organometallic photosensitizer, $[\text{Ru}(\text{bpy})_3]^{2+}$, as the visible light photosensitizer. The second strategy adopts a heterogeneous approach, using TiO_2 as the photosensitizer.

4.2 Results and discussion

This section is divided into subsections such that section 3.2.1 delves into the characteristic physical and optoelectronic properties of each of the MOCHAs, namely, AgXPh (X = Se, S, Te). Subsequently, we unravel photocatalytic performance in section 3.2.2 and 3.2.3 of each of the MOCHAs depending on the type of photosensitization approach employed, with a detailed analysis on their activation, stability, and possible transformation under turnover conditions.

4.2.1 Structure and optoelectronic properties

XRD analysis of each of the MOCHAs confirms its crystallographic structure showing 3 characteristic peaks corresponding to the {002}, {004}, and {006} planes perpendicular with respect to the 2D layers, similar to that of previous reports (Figure 4.1a).^{44,111} We also observe a small shift in the peak positions between the three chalcogens which is consistent with the relative size difference of the chalcogens resulting in an overall contraction or expansion of the unit cell.¹¹² Furthermore, deriving from Bragg's equation, we obtain the interlayer spacing for each of the MOCHAs as 1.41, 1.44, and 1.50 nm for AgSePh, AgSPh, and AgTePh, respectively. Figure 4.1b-4.1d shows the electron microscopy images obtained, which reveal a tetragonal platelet, rod-like, and thread-like morphology for AgSePh, AgSPh, and AgTePh, respectively. While the exact reason is not known, such chalcogen dependent morphology could be related to the change in the Ag-Ag bonding as previously reported by Scriber et al.¹¹³ FTIR analyses of the MOCHAs revealed characteristic peaks at 1434, 1471, 1572 cm^{-1} related to the phenyl rings, specifically corresponding to the C-C stretching vibration. Moreover, due to the difference in the electron donating ability of each of the chalcogens we observe a slight shift in the peak maxima as shown in Figure 4.1e. DRS analysis of the MOCHA powders showed them to have a bandgap in the range of 2.5 – 2.8 eV, close to the previously reported values.^{44,113–115} Based on this observation, typically, we could expect the MOCHAs to carry out photocatalytic water splitting independently without the need for an external photosensitizer (e^- supply). However, considering the valence band potential of AgSePh at $\sim 0.9\text{V}$ (vs. NHE), obtained by Maserati et al.¹¹⁴ via ultraviolet photoelectron spectroscopy (UPS), would indicate the possible inability to carry out water oxidation, thereby needing an appropriate hole scavenger. Therefore, the any photoexcitation in the MOCHA would largely be dominated by the recombination reactions in the absence of an hole scavenger. This is also similar to the observations of Rabl et al. where the applied potential acted as the hole extraction channel to drive the CO_2 reduction reaction. Figure 4.1f shows the solid-state photoluminescence (PL) spectra, with a sharp peak at 2.67 eV ($\sim 467\text{ nm}$) and a broadband emission profile at 2.06 eV, corresponding to AgSePh and AgTePh, respectively. However, AgSPh shows no emissivity in the visible region. This is in-line with the previous reports, where the visible light absorption and emission arises from the 2D delocalization in the argentophilic network in AgSePh and AgTePh, that is absent in AgSPh due to the presence of only linear Ag-Ag chains in the structure.¹¹³ Furthermore, Figure 4.1g shows the time-resolved measurements for AgSePh and

AgTePh with charge-carrier lifetimes of 182 ps and 1.2 ns, respectively. While our value reported for AgSePh is amongst the highest reported, charge lifetimes for AgTePh are highly temperature sensitive – increasing with decreasing temperatures.¹¹⁶

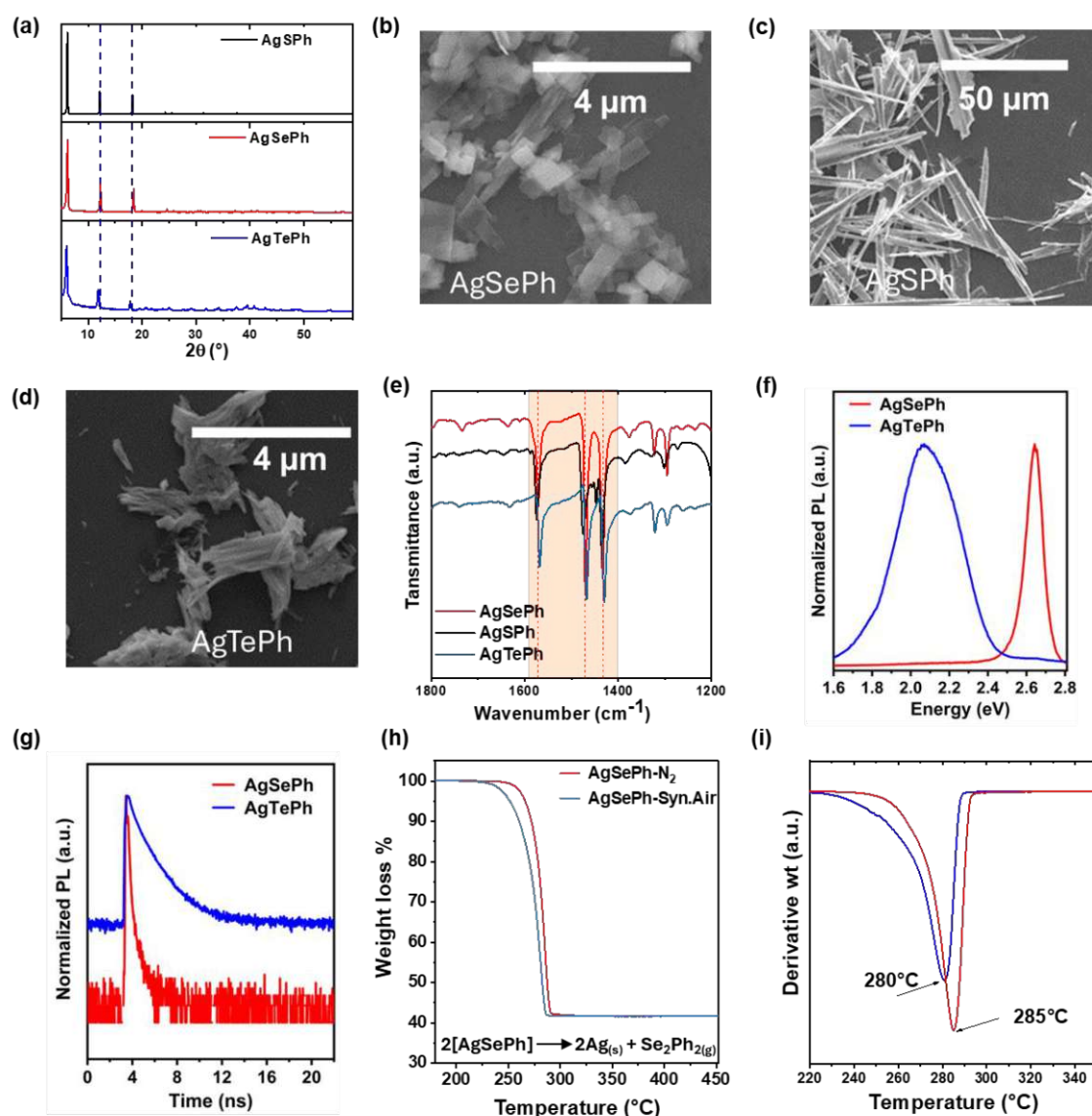


Figure 4.1 (a) XRD pattern of AgXPh MOCHAs (X = S, Se, Te), SEM images of (b) tetragonal diamond like structures of AgSePh (c) needle like morphology of AgSPh and (d) bulk thread like morphology of AgTePh, showing chalcogen dependent morphology (e) FTIR spectra of pristine AgXPh (X = S, Se, Te) (f) steady-state PL emission spectra using 405 nm excitation for AgSePh and AgTePh, (g) time-resolved PL emission spectra using 370 nm excitation and (h) TGA curves of AgSePh in N₂ and synthetic air atmosphere (i) DTG curves derived from TGA curves showing the onset temperature for weight loss of diphenyl diselenide (DPDSe) in N₂ and synthetic air.

TGA analysis of each of the MOCHAs was carried out to determine the thermal stability and decomposition pathways, under air and N₂ atmospheres. Figure 4.1h shows that AgSePh begins to decompose at 230 °C until 280 °C with an overall weight loss of 58 wt % which is close agreement with the theoretical value of 59 wt%. AgTePh also shows a similar weight loss curve with an overall weight loss of 65 wt%, again in good agreement with the theoretical value of 65.4 wt%. In contrast to the previous two, AgSPh shows a higher thermal decomposition temperature as seen in the weight loss curve with an initial weight loss of 40-45% until 350°C,

followed an additional weight loss of 5 wt% at 490 °C. While this is unreported, we believe this could be due to the structural differences between these MOCHAs. However, the overall weight loss is still similar to the theoretical value of 50.4 wt%. Additionally, the absence of any weight loss peak from the DTG curves of the precursors in Figure 4.1i, indicates the absence of any unreacted or excess diphenyl-dichalcogenide precursors which typically decompose at ~180°C. Furthermore, the absence of any change in the weight loss in the presence of absence of air strongly indicate a similar decomposition pathway of most likely losing gaseous diphenyl-dichalcogenide, according to reaction shown in Figure 4.1h, inset. This is further supported by XRD analysis of the products obtained after TGA analysis, showing peaks corresponding to Ag⁰ and no peaks corresponding to AgO_x.

TXRF and XPS analysis were used to quantify the stoichiometric amounts of Ag and chalcogen in each of the MOCHAs. Table 4.1 summarizes these values showing a close relation between the values extracted from XPS and TXRF analysis which are similar to the theoretically predicted ratio.

These set of characterizations confirm the successful synthesis of each of the MOCHAs.

Table 4.1 Ratio between Ag and chalcogen measured via different quantification techniques such as TXRF and XPS analysis

Sample	Ratio	TXRF	XPS	Theoretical
AgSePh	Ag:Se	1.28	1.32	1
AgSPh	Ag:S	1.05	1.01	1
AgTePh	Ag:Te	1.09	0.93	1

Table 4.2 Apparent quantum yields based on incident photons at 445 nm on MOCHA/[Ru(bpy)₃]²⁺ photosystem

Sample	AQY ⁴⁴⁵ (%)
AgSePh/[Ru(bpy) ₃] ²⁺	0.0062
AgSPh/[Ru(bpy) ₃] ²⁺	0.0030
AgTePh/[Ru(bpy) ₃] ²⁺	0.0018

Table 4.3 H₂ and CO₂ produced using AgSePh/[Ru(bpy)₃]²⁺ under 445 nm illumination (335 mW cm⁻²) over 140 mins

Time (min)	H ₂ (μmol)	CO ₂ (μmol)
20	0.249	0.016
40	0.448	0.029
60	0.631	0.049
80	0.869	0.076
100	0.906	0.088
120	1.015	0.104
140	1.205	0.138

4.2.2 Photocatalytic performance of MOCHA as a quasi-homogeneous photosystem

In this section, we studied the photocatalytic potential of all three MOCHAs using a quasi-homogeneous approach – where we used a molecular photosensitizer dissolved in a solution suspended with MOCHA particles. We used [Ru(bpy)₃]²⁺ as the light absorber since it has a high molar absorptivity constant with an absorption maximum (450 nm ~2.12 eV) in the visible

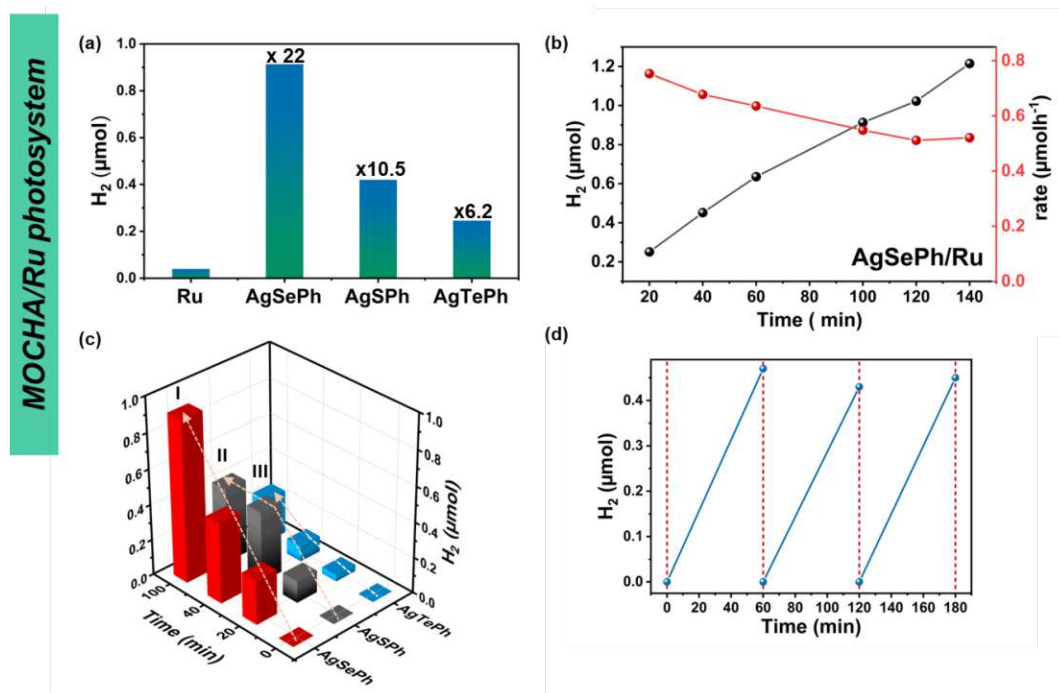


Figure 4.2 (a) Visible-light-driven H_2 evolution activities of AgXPh MOCHAs under quasi-homogeneous conditions along with the reference experiment involving just the $[Ru(bpy)_3]^{2+}$ (b) Time resolved HER profile of the AgSePh/ $[Ru(bpy)_3]^{2+}$ along with H_2 production rates for 140 min (c) HER performance of AgXPh/ $[Ru(bpy)_3]^{2+}$ (X = S, Se, and Te) over 100 min of reaction (d) cyclability tests involving three light on-off cycles with intermittent purging.

region, corresponding to the metal to ligand charge transfer.¹¹⁷ Typically, upon illumination $[Ru(bpy)_3]^{2+}$ absorbs a visible light photon resulting in its long-lived excited state $[Ru^*(bpy)_3]^{2+}$, which then transfers the electron to the catalyst and simultaneously reverts back to the $[Ru(bpy)_3]^{2+}$ using ascorbic acid (H_2A) as a sacrificial agent.¹¹⁷ Since $[Ru(bpy)_3]^{2+}$ is dissolved in the solution, as compared to the MOCHA particles which are freely suspended, the sensitization process is most likely dynamic in nature with the $[Ru(bpy)_3]^{2+}$ either attached to the MOCHA only via weak forces, as opposed to immobilization onto the MOCHA surface. Throughout this chapter the photosystem is denoted as AgXPh/ $[Ru(bpy)_3]^{2+}$ where X = Se, S, and Te. Reference experiment using only the $[Ru(bpy)_3]^{2+}$ photosensitizer in the absence of MOCHAs produced a small amount of hydrogen. However, the addition of MOCHAs to this system resulted in a sharp increase in the photocatalytic hydrogen production reaching values up to $0.6 \mu\text{mol h}^{-1}$ in the case of best performing AgSePh/ $[Ru(bpy)_3]^{2+}$. Figure 4.2a shows the overall amounts of hydrogen produced with the performance in the following order – AgSePh > AgSPh > AgTePh, each catalyzing the hydrogen evolution reaction 22, 10.5, and 6.2 times higher as compared to pristine $[Ru(bpy)_3]^{2+}$. This is also reflected in the apparent quantum yields summarized in Table 2.2. While the charge carrier lifetimes obtained from PL measurements showed the highest values for AgTePh, the poor photocatalytic performance could be attributed to the self-trapping nature of AgTePh, which is significantly more evident at low temperatures of $15 \text{ }^\circ\text{C}$, as in the photocatalytic tests.¹¹⁶ In contrast to this AgSePh did not show any temperature dependence for the charge carrier lifetimes. Long-term HER testing using the best performance AgSePh/ $[Ru(bpy)_3]^{2+}$, we observed a relatively stable hydrogen production for at least 2 h with a slight decrease in the production rate over time (Figure 4.2b). Corresponding to this we also saw a substantial H_2A oxidation via the photogenerated holes.¹¹⁸ however, since these can be a complex range of oxidation products resulting from partial

oxidations, CO₂ evolved would indicate the amount of complete oxidation reactions resulting in the complete mineralization of H₂A according to the following formula,

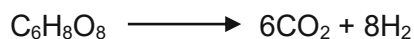


Table 4.3 shows the H₂ and CO₂ values obtained over the period of 140 min. The overall ratios of CO₂ to H₂ is far from the values expected from the equation above possibly due to intermediate H₂A products such as xylonic, threonic, and oxalic acids, co-existing in the solution.¹¹⁹ Figure 4.2c shows the long-term hydrogen production using each of the MOCHAs. While the initial amount of hydrogen is higher using AgSPh as compared to AgTePh, the rate of production decreased for AgSPh showing strong deactivation behavior over a course of 100 min. Finally, Figure 4.2d shows the hydrogen produced over multiple illumination cycles, with an intermediate purging step. We observed that the catalysts retain its photocatalytic performance even after multiple cycles without an average value close to the initial performance.

Figure 4.3a shows the XRD patterns for each of the recovered MOCHAs before (dotted line) and after (solid line) the HER reaction. There are no observable shifts in the peak positions along with the absence of any new peak appearing or old peak disappearing, which confirms

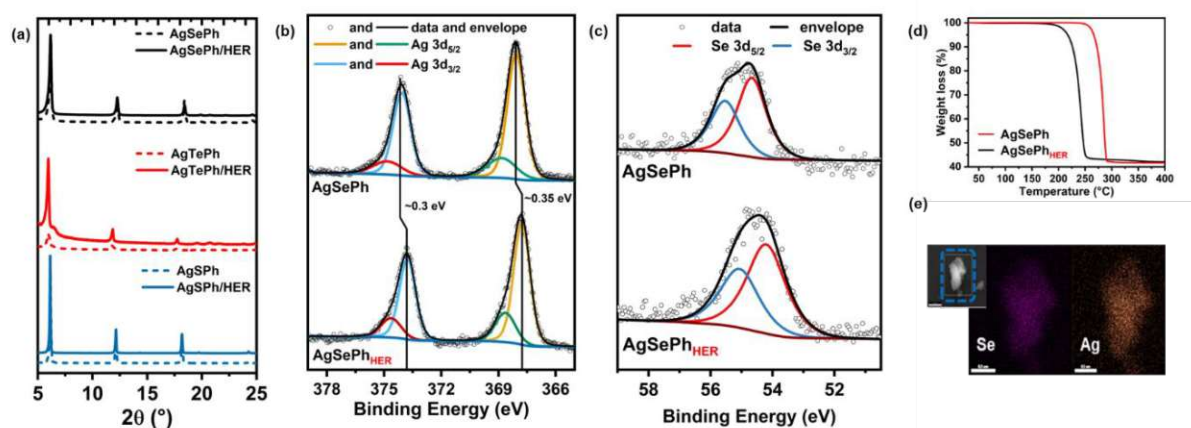


Figure 4.3 (a) XRD pattern of AgXPh MOCHAs, (b) XPS Spectra of the Ag 3d and (c) Se 3d edge in AgSePh, (d) TGA profiles, and (e) Photoluminescence spectra of AgSePh before and after HER testing in catalysis.

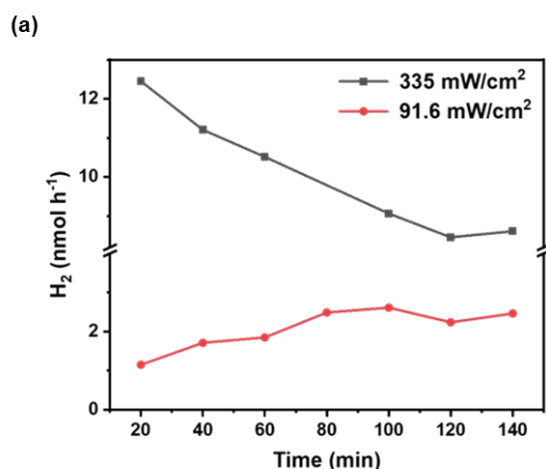


Figure 4.4 Rate of hydrogen production using AgSePh/[Ru(bpy)₃]²⁺ photosystem under two different light intensities using 445 nm LED lamp over a period of 140 min

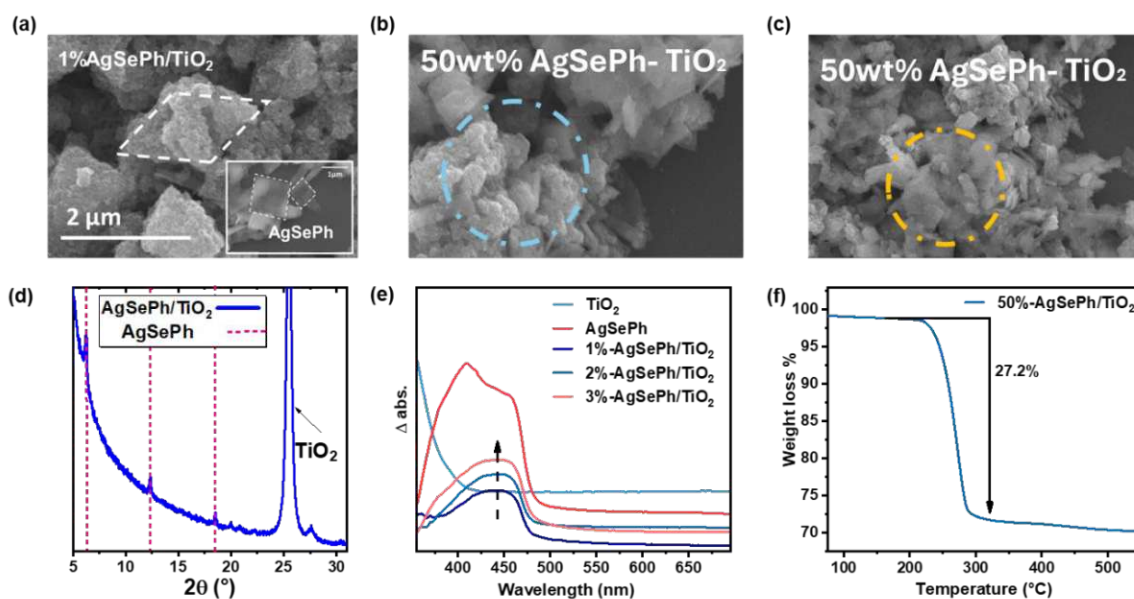


Figure 4.5 (a) SEM image of 1wt% AgSePh/TiO₂ composite showing diamond like structures covered in TiO₂ nanoparticles, inset: pristine diamond structures of AgSePh, (b) SEM image of 50 wt% AgSePh/TiO₂ composite showing exposed areas of TiO₂ and (c) only AgSePh diamonds, (d) XRD pattern of 3wt% AgSePh/TiO₂ composite showing the characteristic peaks of AgSePh and TiO₂ (anatase and rutile) (e) DRS spectra of Z wt% AgSePh/TiO₂ (Z = 1, 2, and 3) with respect to TiO₂ as zero background (f) TGA curves of 50 wt% AgSePh/TiO₂ composite in synthetic air

Table 4.4 This table shows the quantification data obtained from XPS analysis of the ratio between the metal and chalcogen present in before and after HER testing

Sample	Ratio	Before	After	Theoretical
AgSePh	Ag:Se	1.32	1.18	1
AgSPh	Ag:S	1.01	0.95	1
AgTePh	Ag:Te	0.93	0.99	1

the structural integrity of the sample after over 5 h of catalysis. This also confirms that there is no solvent intercalation between the MOCHA layers during catalysis, as this would cause an expansion in the interlayer spacing resulting in a peak shift to lower 2 theta values. In-line with this, SEM-EDX mappings also show the intact diamond morphology of the AgSePh as shown in Figure 4.3e. In contrast to this, the quantification data obtained from XPS analysis showed no change in the elemental composition of the MOCHA (summarized in Table 2.4), but while the overall shape of the Ag 3d peak and Se 3d peaks is the same before and after HER, we observe a slight shift of around 0.3 eV towards a lower binding energy as shown in Figure 4.3b-4.3c. This shift could indicate a weakening of the Ag-Se bonds in the overall structure. TGA analysis further corroborates this reasoning, as we observe a strong shift of almost 40 ° in the decomposition onset temperature that corresponds to the loss of (Se)₂(Ph)₂, (Figure 4.3d). Finally, photoluminescence measurements of the AgSePh after reaction does not show a new peak or shift in the original emission spectrum confirming there is no amorphous polymeric MOCHA present under HER conditions which would result in the loss of emission as reported by Popple et al.¹²⁰ Overall, all MOCHAs perform well for the photocatalytic hydrogen production. However, the mild deactivation in activity can be attributed to the combined effects of weakening of the coordination strength in the MOCHA as well as the photodegradation of [Ru(bpy)₃]²⁺ via self-oxidation or agglomeration under illumination.¹²¹ Figure 4.4 shows the HER performance of AgSePh/[Ru(bpy)₃]²⁺ under lower light intensity with a more-stable time-

dependent H₂ evolution profile. This result substantiates the [Ru(bpy)₃]²⁺ photobleaching as the limiting cause.

4.2.3 Photocatalytic performance of MOCHAs as a heterogenized photosystem

In this section we study the photocatalytic potential of all three MOCHAs using a heterogenous approach – where we use powder TiO₂ (Anatase) as the light absorber. TiO₂ is one of the most studied inorganic photosensitizers because it is inexpensive, non-toxic, and abundant. First, we prepare a series of composites called, Z wt% AgXPh/TiO₂, where Z = 1, 2, 3, and 50 wt% corresponding to the amount of MOCHA in the overall composite. While the lower loadings were chosen based on widely used optimized values for co-catalysts, a 50 wt% sample was prepared as a model system, where any transformation under turnover conditions would be magnified and detectable with otherwise low sensitivity devices. Before moving on to the testing of these composites, we characterized them using various techniques to firstly, understand any changes that might have occurred in the structural or chemical properties of the MOCHAs and secondly, confirm the successful formation of intended composites. Figure 4.5a shows the SEM images obtained for 1wt% AgSePh/TiO₂ where we observe micrometer

Table 4.5 AgXPh (X = Se, S, Te) loadings derived from TXRF measurements for the low-loading samples.

Intended loading (wt%)	AgSePh	AgTePh	AgSPh
1	1.3	-	-
2	2.5	1.8	1.7
3	3.3	-	-

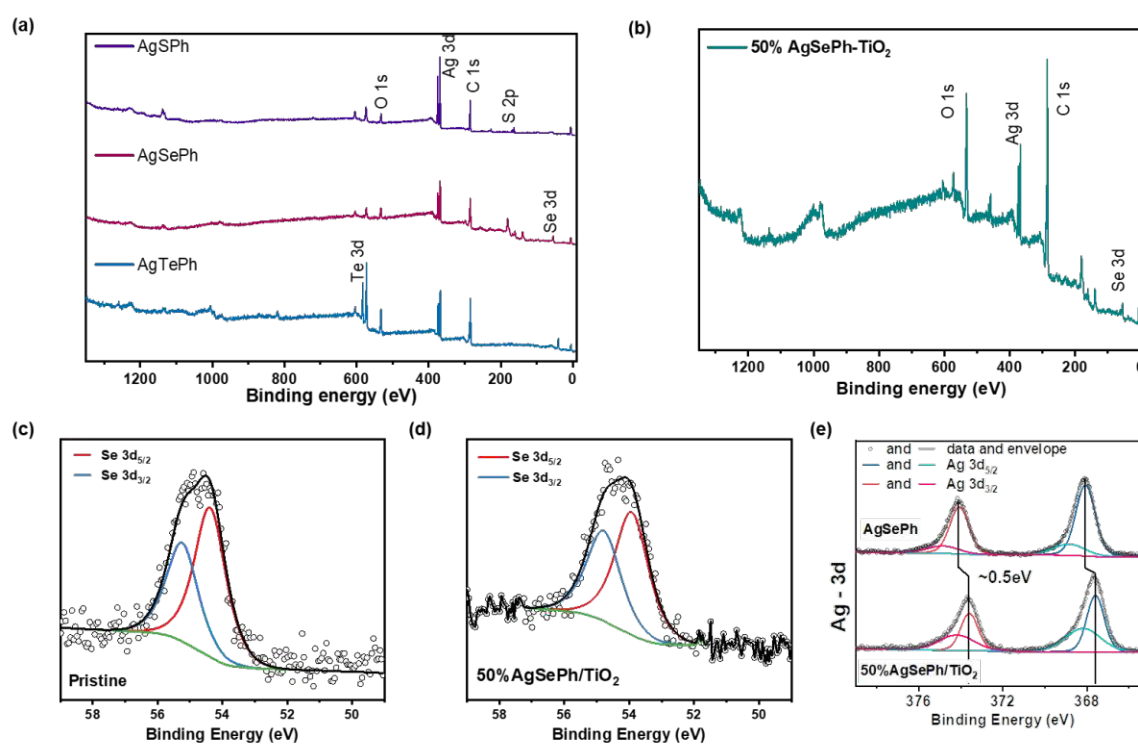


Figure 4.6 XPS survey spectra of (a) Pristine AgXPh (X=S, Se, Te) confirming the presence of the Ag and the corresponding chalcogen, (b) 50%-AgSePh-TiO₂ before HER reaction, (c) XPS curves of Se – 3d edge for Pristine AgSePh (d) after composite formation (50wt%) with TiO₂ (e) XPS spectra of Ag 3d edge for pristine and 50%AgSePh/TiO₂ composite

Table 4.6 Quantification data from TXRF and XPS analysis of the compositional ratio of Ag:Se before and after photocatalytic HER tests

Sample	Ratio	TXRF	XPS	TGA	Theoretical
50% AgSePh/TiO ₂	Ag:Se	0.81	0.98		1
	Ag:Ti	0.47	0.60		0.5
50% AgSePh/TiO ₂ -[HER]	Ag:Se	0.99	2.03		1
	Ag:Ti	0.48	0.73		0.5

large MOCHA structures, uniformly coated with agglomerates of nano-sized TiO₂ (~ 25 nm). However, in the model 50 wt% sample, there were few observable areas exposed with uncovered AgSePh surfaces as shown in Figure 4.5b-c. Figure 4.5d shows the XRD pattern of 3wt% AgSePh/TiO₂ with the characteristic peaks corresponding to TiO₂ with pronounced diffractions at 25.3° and 27.4°, for anatase and rutile, respectively. Additionally, in the 3 wt% AgSePh/TiO₂ sample we observe low intensities of the characteristic peaks from the AgSePh MOCHA confirming the structural integrity after composite formation. Figure 4.5e shows the DRS curves for all of the loadings of AgSePh/TiO₂ using pristine TiO₂ as the measurement background. This was done to isolate and magnify the peaks appearing from the MOCHAs present in the composites. In all the spectra, we clearly observe a characteristic absorption centered around 400-450 nm range corresponding to AgSePh. Noticeably, the absorption intensity increases with the increase in the loading from 1 to 3 wt%, complementing the observed coloration in the composites. Table 4.5 summarizes the actual loading of AgSePh present in the TiO₂ composite quantified using TXRF. We observe a slightly higher loading (~0.3%) of MOCHAs in comparison to expected values most likely due to instrumental absorption effects and errors. Similarly, when measuring higher loading samples, like 50 wt%, due to the presence of two heavy elements - the emitted rays from Ag can be reabsorbed by Ti – which results in underestimating the real loading amounts. Therefore, we used TGA analysis as an alternative to quantify the amount of AgSePh in the composite since the loss of Diphenyl diselenide (DPDSe) can be directly correlated to the total amount of MOCHA. Figure 4.5f shows the TGA curves with an overall weight loss of 27.2 wt% (between 230 and 300 °C). Based on this, we can estimate the amount of C₆H₅Se and Ag to be ~27.2 mg and ~18.8 mg, respectively. Therefore, the total amount of AgSePh present in the composite is ~46 wt% which is close to the expected 50 wt%. XPS analysis comparing spectra obtained from AgSePh before and after the formation of the composite shows the presence of all expected elements in the survey scans (Figure 4.6a-b). The detailed analysis of the Se 3d edge shows no changes in the peak positions at a binding energy of 54.84 eV and 54.39 eV, for the pristine and the composite sample, respectively (Figure 4.6c-d). However, the Ag 3d edge of the pristine AgSePh shows a slight shoulder at higher BE, accordingly the best fits are obtained by de-convoluting the data with two fits corresponding to 367.5 eV for AgSePh and 368.1 eV for the composite with a slight shift of ~0.5 eV, values typically found in compounds

Table 4.7 Apparent quantum yields based on incident photons at 365 nm on MOCHA/TiO₂

Sample	AQY ³⁶⁵ (%)
AgSePh/TiO ₂	0.10
AgSPh/TiO ₂	0.04
AgTePh/TiO ₂	0.11

with Ag in a mixed oxidation state of +1 and +2 (Figure 4.6e).¹²² Auger spectra of Ag M₅N₄₅N₄₅ and Ag M₄N₄₅N₄₅ further confirmed the Ag in AgSePh is a mixture of Ag⁺¹ and Ag⁺² oxidation states. More importantly, metallic Ag can be excluded since Ag⁰ only appears at higher BE and has a characteristic full width at half maximum (FWHM) with an asymmetric line shape.¹²³ Finally, the quantification results, as summarized in Table 4.6, show the preserved ratio of Ag:Se before and after composite formation indicating that the MOCHA's chemical composition remains the same. Complementary to these results, the Ti 2p edge spectra also showed no changes in the peak positions upon composite formation with the MOCHA.

Based on these results, we confirmed that the MOCHAs retain their chemical and structural stability after composite formation with TiO₂. Next, we move onto testing these prepared composites for photocatalytic hydrogen evolution. Since AgSePh/[Ru(bpy)₃]²⁺ showed the highest performance compared to S and Te, here as well, we first vary the loading of the AgSePh/TiO₂ to find the optimum value to obtain the highest possible performance in H₂ production, followed by the preparation of similar loadings using AgSPh and AgTePh as well. Figure 4.7a shows the total amount of H₂ produced after 1 h of illumination with both pristine TiO₂ and with AgSePh/TiO₂. Clearly, AgSePh strongly promotes the hydrogen evolution reaction with an optimal loading of 2 wt% achieving an enhancement in activity by a factor of 47 in comparison to pure TiO₂. Chopped light chronoamperometric measurements shed some light onto this behavior. Since TiO₂ is an n-type semiconductor – it behaves as a photoanode under illumination – producing a positive current response that corresponds to the photogenerated holes in the system. The photocurrent response is directly proportional to the

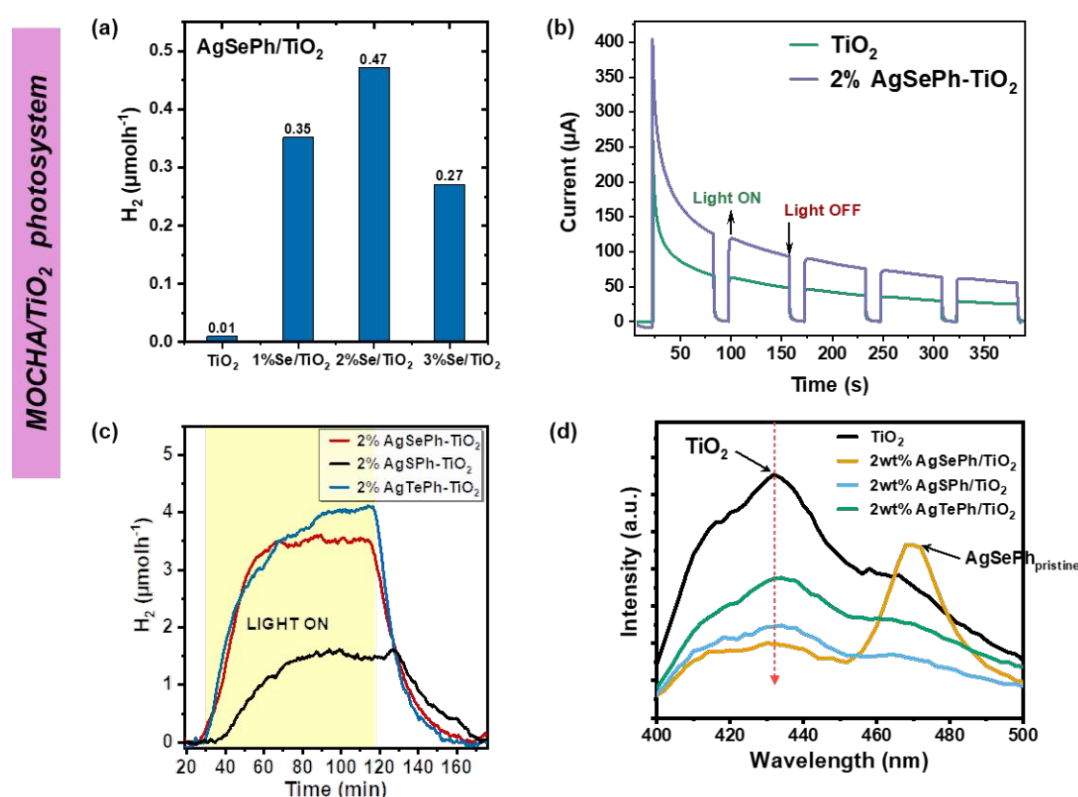


Figure 4.7 (a) H₂ production profile of Z wt% AgSePh on TiO₂ (Z = 1, 2, and 3) along with bare TiO₂ (b) transient photocurrent response of 2%AgSePh/TiO₂ composite samples under 365 nm illumination (c) on-stream detected H₂ evolution profiles for 2 wt% AgXPh/TiO₂ composites (d) PL spectroscopy profiles of the MOCHA/TiO₂ composites using 365 nm as excitation wavelength

number of holes available for reaction. Figure 4.7b shows the photocurrent response of both pure TiO₂ films and AgSePh/TiO₂ films that were drop casted onto FTO glass electrodes. We observed an 80 % higher photo-response in the presence of AgSePh, most likely due to the charge extraction ability of the MOCHA from TiO₂, resulting in a higher number of available holes for reactions. This further complements the excellent photocatalytic performance of AgSePh/TiO₂. As for the optimal loading, we obtain 2 wt % as the best performing sample. This trend can be related to the light absorption efficiency and surface area available for hole consumption. Firstly, at high loading – too-much AgSePh could lead to insufficient light absorption/sensitization by TiO₂, while too low loading would lead to parasitic absorption of excessive TiO₂ that are not in contact with any MOCHA surface, thus not contributing to the charge consumption for H₂ production.

Notably, when comparing the 2 wt% AgSePh/TiO₂ and AgSePh/[Ru(bpy)₃]²⁺ performance, we observe that although they have similar H₂ production, AgSePh/TiO₂ has much lower amounts of AgSePh and therefore outperforms the latter when compared under mass normalized activity, which is also reflected in the higher AQY values of AgSePh/TiO₂, as summarized in Table 4.7 and Table 4.2. This could imply a more efficient sensitization (charge transfer) between the MOCHA and TiO₂ due to the heterojunction formation at the interface as compared to the [Ru(bpy)₃]²⁺ case where it is more dynamic sensitization and dependent on factors such as concentration, temperature, etc. However, before concluding TiO₂ to be the better sensitizer it is important to note the differences in the incident light energy, 365 nm (4.4 eV photon⁻¹) for TiO₂ and 445 nm (2.7 eV photon⁻¹) for [Ru(bpy)₃]²⁺, partially accounts for this discrepancy in performance. Furthermore, even if we attempt to keep the total number of incident photons the same, other factors will hinder the comparison. Next, based on the optimum value we further prepared each of the MOCHA/TiO₂ composites and measured the photocatalytic performance over a longer period of illumination. These experiments were carried out using a home-made reactor and an online detection method using a continuous Ar stream carrying the products to the detector, as described in the experimental section. Figure 4.7c shows the catalytic hydrogen evolution performance for each of the prepared composites. In contrast to the [Ru(bpy)₃]²⁺ assisted sensitization case, here we observe an HER activity trend of AgSePh~AgTePh>AgSPh which indicates that the interface at the MOCHA/TiO₂ junction plays an important role in the extraction and utilization of charges. While chopped light chronoamperometric experiments could shed light on this trend, we faced several challenges with AgSPh and AgTePh/TiO₂ electrode preparation mostly with regard to film adhesion on the FTO glass surface thereby rendering that approach unfeasible. However, solid-state PL measurements, where we measure the emission spectra of TiO₂, of each of the composite samples could be used to understand the charge transfer mechanism at the interface, since better charge transfer would result in strong quenching of the emission signal as compared to pristine TiO₂. Figure 4.7d shows the emission spectra obtained using 377 nm excitation on pristine TiO₂ and all of the MOCHA/TiO₂ composites. Here, we see a strong quenching in the AgSePh composite in-line with the highest observed HER performance. However, for the remaining two we observe the quenching ability in the order AgSPh >~ AgTePh which is opposite of their observed catalytic performance. Time-resolved PL data, summarized in Table 4.8, also show a similar trend of the shortest lifetime in AgSePh/TiO₂, followed by almost similar lifetimes in AgSPh and AgTePh composites. Based on these, we can conclude that the overall photocatalytic activity is dependent on more factors than just the charge transfer that needs some more advanced characterization. Additionally, AgSPh and AgSePh composites were able to achieve stable activity quicker than the AgTePh which only reached a stable H₂ production rate after 100 min. While the overall HER performance was stable over the course

of the 2 h illumination, we observe visual changes in the sample suspension transforming from a pale yellow, white, and red color for AgSePh, AgSPh, and AgTePh, respectively, to a faint grey color after the experiment. Since these samples have a very low amount of MOCHA in the composite, we test the model 50 wt% AgSePh/TiO₂ sample under similar conditions, which was then recovered for post catalytic analysis.

50wt% AgSePh/TiO₂ performed worse than the 2wt% AgSePh/TiO₂ sample as expected (from previous discussion), with a stable H₂ production rate of ~2.5 μmol h⁻¹ for over 3 h of illumination. In addition to measuring H₂ production, we also quantified the CO₂ produced through methanol oxidation, utilizing photogenerated holes on the TiO₂ surface. Figure 4.8a-b shows both H₂ and CO₂ production curves over two consequent cycles, revealing that the overall activity is retained showcasing the possibility for sample reusability. Similar to the low loading case we observe a strong color change from a bright yellow to slightly grey further darkening over the course of the experiment (~10 h) resulting in a dark grey powder, as shown in Figure 4.8a (inset). Figure 4.9a shows the XRD pattern of the composite before and after the catalytic run. We observe a strong decrease in the characteristic peaks corresponding to the AgSePh MOCHA and a new low intensity peak appears at around 78°, corresponding to the formation of metallic Ag (Figure 4.9a inset). However, SEM images of this sample after HER still show areas corresponding to the original AgSePh/TiO₂ morphology, implying that the composite structure is largely preserved (Figure 4.9b-c). In stark contrast to these results, XPS analysis of the composites before and after HER show no changes in the peak positions and peak shapes of both Ag 3d and Se 3d edges, contradicting the previous observation of the presence of metallic Ag in the XRD pattern (Figure 4.9d-e). Considering that XPS is mostly a surface sensitive technique probing on the top 10 nm of the composite sample, and XRD

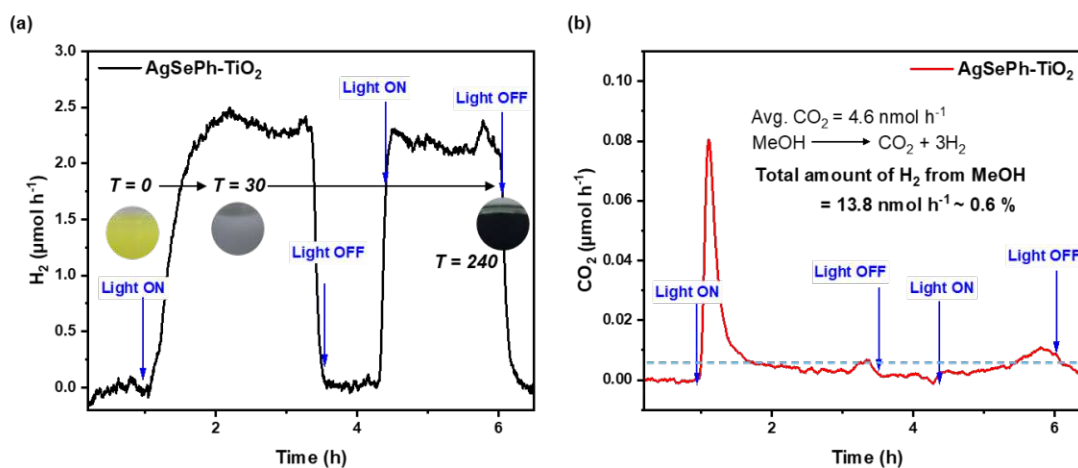
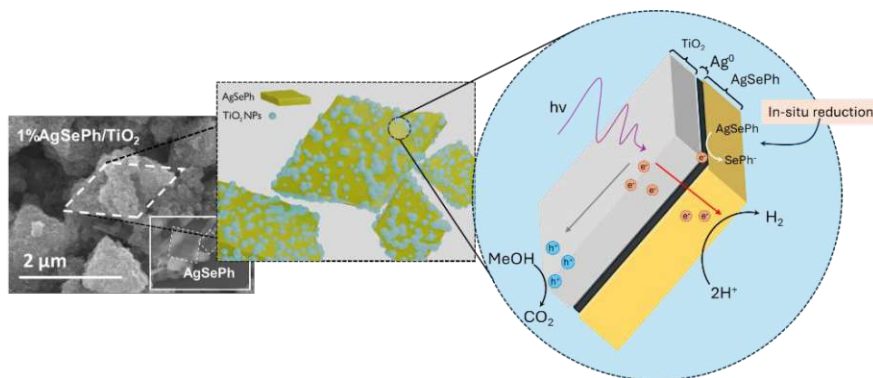


Figure 4.8 H₂ (a) and CO₂ (b) evolution rates of the heterogeneous AgSePh/TiO₂ composite

Table 4.8 individual contributions during the relaxation processes with average lifetimes

Samples	Lifetime and Proportion							
	τ_1 (ns)	A ₁	τ_2 (ns)	A ₂	τ_3 (ns)	A ₃	τ_{avg} (ns)	χ^2
TiO ₂	10.62	0.57	0.38	2.5	1.01	4.85	5.89	1.14
2wt% AgSePh/TiO ₂	9.75	0.06	0.51	3.81	1.08	3.98	1.61	1.08
2wt% AgSPh/TiO ₂	9.98	0.26	0.61	5.55	1.75	1.89	3.60	1.34
2wt% AgTePh/TiO ₂	10.45	0.18	0.94	3.79	0.41	3.66	3.46	1.42



Scheme 4.1 (left) SEM image of AgSePh/TiO₂ (middle) illustration showing a large MOCHA particle (yellow) coated with TiO₂ nanoparticles (white), and (right) zoomed in view at the TiO₂/AgSePh interface under illumination conditions showing the in-situ reduction of AgSePh to Ag⁰ via the loss of SePh⁻

characterizes the bulk and surface effect combined – we believe that a small fraction of AgSePh is reduced to Ag⁽⁰⁾-AgSePh combination at the interfacial junction between the MOCHA and TiO₂, as shown in Scheme 4.1. This reduction most likely happens at the beginning of the illumination cycle and stops after a few nm; therefore, we are unable to detect it using XPS but clearly observe diffraction peaks corresponding to Ag⁰ in the XRD pattern. This is further reflected in the TGA curves obtained from samples after catalysis, Figure 4.9f

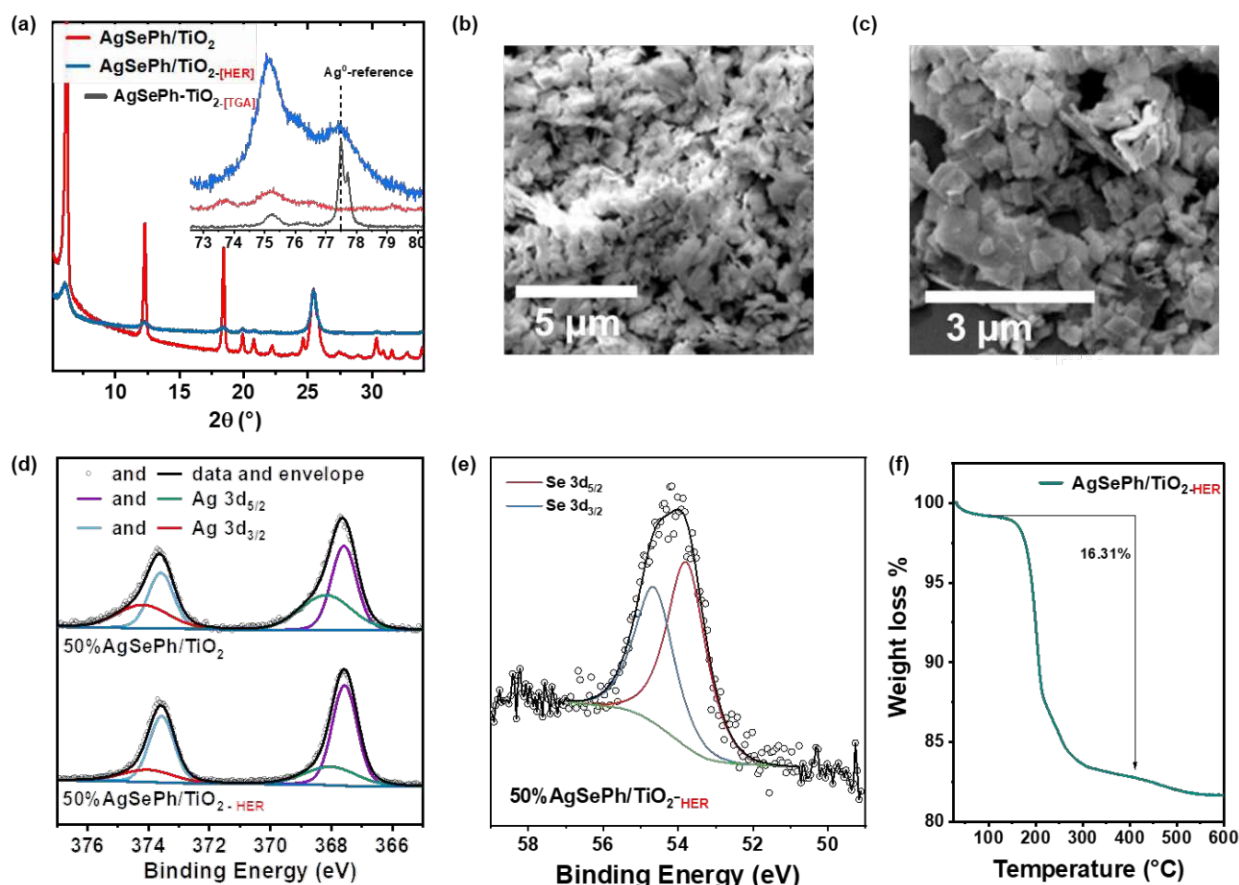


Figure 4.9 (a) XRD pattern of AgSePh/TiO₂ before and after heterogeneous HER (inset: XRD pattern showing the peak corresponding to Ag⁰, JCPDS: 04-004-8065) (b) SEM images of high loading 50wt%-AgSePh-TiO₂ before and after HER reaction using TiO₂ as a photosensitizer in the on-stream setup (c) XPS spectra of Ag 3d and (d) Se 3d edge of the composite before and after catalysis (f) TGA curve showing mass loss of AgSePh-TiO₂ after HER

shows an overall weight loss of ~16.3 wt%, strongly reduced from the original 27.2 wt% from the loss of diphenyl diselenide content in the MOCHA.

Previous tests on the photostability of AgSePh and AgSPh MOCHA powder were done using both UV- and visible light sources, with no structural, compositional or chemical changes even after several days. In our case, however, the interfacial transformation rather happens under the complex reaction conditions of the photocatalytic process, nonetheless resulting in a catalyst system with a stable H₂ production for over 4 h. Based on this hypothesis, we further carried out some reference experiments subjecting each of the pure MOCHA powders to similar conditions as in the photocatalytic testing, so as to decouple any effects caused due to the presence of TiO₂ and only showing transformation/s caused due to other factors such as solvent interactions under illumination, etc. Firstly, we do not observe any visual color change in the illuminated sample and secondly, XRD analysis reveals that all three characteristic peaks, at 6°, 12°, and 18° are preserved in the samples post illumination. However, we do observe an additional peak at 78°, corresponding to metallic Ag on the surface of the MOCHA. This result suggests that the observed Ag⁽⁰⁾-AgSePh formed in the composite could have a small contribution from a light induced transformation in the MOCHA surface.

4.3 Conclusion

To summarize, this chapter reports the photocatalytic performance of a series of Ag-based OIHs, specifically AgXPh (X = S, Se, Te) MOCHAs, for the hydrogen evolution reaction (HER), under visible- and UV-light using molecular [Ru(bpy)₃]²⁺ and semiconductor TiO₂ photosensitizers creating a quasi-homogeneous and heterogeneous photosystem, respectively. Among the three, AgSePh outperforms the other MOCHAs in both cases, while the relative activity between AgSPh and AgTePh strongly depends on the sensitization pathway. In the heterogeneous case, MOCHA/TiO₂ photosystem undergo a rapid transformation, yielding a sandwich-like structure of AgXPh/Ag⁰/TiO₂ nanohybrids that exhibit stable HER performances over 4 h of illumination. This transformation process is strongly correlated with photocatalytic (irradiation) conditions resulting in the loss of organic ligands from the surface of the MOCHA structures and is likely accelerated by the presence of photoexcited carriers in the semiconductor which promote Ag¹⁺-to-Ag⁰ reduction. Conversely, the quasi-homogeneous MOCHA/[Ru(bpy)₃]²⁺ photosystem shows a relative stable and active HER performance without any noticeable degradation in the MOCHAs' structures even after long term reaction. However, a small drop in HER activity over time can likely be traced back to the irreversible consumption or degradation of the molecular photosensitizer. These results highlight the potential of MOCHAs as OIH photocatalysts for HER providing a pathway for their further exploration in constructing various photosystems for water splitting.

4.4 Experimental section

4.4.1 Synthesis of AgSePh and AgSPh

The synthesis was followed as reported by Rabl et al.⁴⁴ Briefly, to a 30 mL microwave vial 0.75 mmol of DPDS (Diphenyl diselenide) or DPDS (Diphenyl disulfide) (Acros Organics, 99%) were dissolved in 5 mL of MeOH via ultra-sonication for 1 h, individually. In another vial, 0.5 mmol AgNO₃ was dissolved in 2 mL of DI H₂O. Next, the AgNO₃ (abcr, 99.9%) solution was slowly added to the DPDX (Se/S) methanol solution under vigorous stirring. Upon mixing the two solutions, a yellow and a white suspension corresponding to DPDS and DPDS was obtained, respectively. The suspension was heated to 110 °C for 5 h via microwave irradiation under constant stirring at 500 rpm. The obtained MOCHA powders were washed with 40 mL

of methanol and water, each, via vacuum filtration. The filtered powder was dried at 50 °C overnight.

4.4.2 Synthesis of AgTePh

AgTePh was prepared by modifying the original aforementioned procedure by using 5 ml of anhydrous DMF as a solvent for dissolving 0.75 mmol of DPDTe, instead of MeOH, via ultrasonication for 5 min. As before, 2 mL of aqueous AgNO₃ solution was prepared and added dropwise to the DPDTe solution. Since the color of DPDTe is red, the solution immediately turned into a bright red colored suspension. The suspension was heated under microwave irradiation to 120 °C, at a heating rate of 2 °C min⁻¹ and held at that temperature for 8 h. The suspension was then rapidly cooled to 55°C and washed with 30 mL DMF and water, each. Finally, to completely remove any synthesis solvent such as DMF, the powder was dried at 150 °C in a vacuum oven.

4.4.3 Photocatalytic setup

Photocatalytic performance was assessed by measuring the amount of H₂ produced as a function of illumination time. In each case, a closed reactor setup was laterally illuminated using an LED lamp. H₂ quantification was done using a gas chromatograph calibrated with a six-point calibration ranging from 100 to 50 000 ppm.

4.4.3.1 MOCHA/TiO₂ composites (heterogeneous photosystem)

In these experiments, the MOCHAs were dip coated onto light absorbing inorganic semiconductors (TiO₂). This resulted in a “static” sensitization process where the semiconductor and co-catalyst form a relatively strong solid-solid junction at which the charge transfer processes occur. First, AgSePh was used as an exemplary case to optimize the conditions to obtain maximum H₂ evolution performance. Briefly, Z (Z = 1, 2, and 3) mg of AgSePh and 100 mg of TiO₂ (<25 nm) were dispersed in 5 and 30 mL of MeOH individually, via ultrasonication for 15 min to obtain a homogeneous suspension. The two suspensions were then mixed and further sonicated for 10 min followed by stirring overnight. Next, the solution was vacuum filtered and washed with 30 mL of MeOH to remove any loosely attached MOCHA on the surface of TiO₂. The powder was dried at 50 °C overnight to completely remove the MeOH. To avoid potential bottlenecks in understanding the transformation of the MOCHAs during catalysis, a reference sample of 50 wt% AgSePh/TiO₂ composite was also prepared to act as a model system suitable for complementary post-catalytic characterization studies.

4.4.3.2 HER testing: On-Stream versus closed reactor

The long-term HER testing of AgSePh/TiO₂ photosystem was carried out in an on-stream HER testing system using a homemade slurry-type reactor with side illumination using a UV LED source with an incident light intensity of 193 mW cm⁻² at 365 nm (Thorlabs SOLIS). In a typical measurement, 10 mg of the sample was suspended into 10 mL of 50 vol.% aqueous methanol solution via ultrasonication for 5 min. The reactor was then purged with Ar gas at a flow rate of 100 mL min⁻¹ for 10 min, following which the flow rate was reduced to 15 mL min⁻¹ for the entire duration of the experiment. The H₂ produced was carried to a continuous gas analyzer (X-stream, Emerson Process Management) using a thermal conductivity detector.

In contrast, a typical closed reactor HER test was done by suspending 2 mg of catalyst powder in 2 mL of 50 vol.% aqueous methanol solution. The suspension was purged with Ar at 10 mL min⁻¹ for 10 min followed by making an initial injection, of 200 µL of gas, into the GC. Following this the catalyst suspension was illuminated with a 365 nm UV LED lamp and a gas sample of

200 μL was taken from the headspace and injected into the GC to quantify the total amount of H_2 produced.

It is important to note that the “closed HER tests” were used for a quick testing approach for a higher number of sample screening and were used to find the optimal loading of MOCHA/ TiO_2 composite sample for highest HER performance. Following this, the “On-stream HER tests” allowed to understand the dynamic nature of the H_2 produced in terms of stably produced H_2 rates. Therefore, the tests for comparing different MOCHAs/ TiO_2 composite samples were done using the On-stream HER setup.

4.4.4 Recycling experiments

Re-cycling experiments were carried out using the “On-stream” HER testing to understand the re-usability of the catalyst after one complete illumination cycle. These experiments were carried out using the same catalyst solution by introducing a 30 min purge with Ar gas in the absence of any light. This was done to flush out all H_2 produced during the previous cycle and to avoid any effects of oxygen entering the system. This allowed to understand the stability of the catalysts hydrogen production rate on multiple illumination cycles under an inert atmosphere.

4.4.5 MOCHA/ $[\text{Ru}(\text{bpy})_3]^{2+}$ test setup

In this mode, the MOCHAs were freely suspended in a reaction solution of MeOH-water in 9:1 ratio and sensitization were done using $[\text{Ru}(\text{bpy})_3]^{2+}$, a visible light absorbing photosensitizer. This system denoted as MOCHA/ $[\text{Ru}(\text{bpy})_3]^{2+}$, provides a rather “dynamic” sensitization process where the interaction between the $[\text{Ru}(\text{bpy})_3]^{2+}$ molecule and MOCHA was predominantly the transfer of electrons for proton reduction while the generated hole was consumed by ascorbic acid (H_2A) chosen here as a common sacrificial agent often used in the community of homogeneous photocatalysis. Again, 10 mg of the MOCHA was dispersed in 4.5 mL of MeOH. Simultaneously, 9.6 mg of $[\text{Ru}(\text{bpy})_3]^{2+}$ and 320 mg of H_2A were dissolved in 4.5 mL MeOH and 2 mL of DI water via ultrasonication for 10 min. Finally, the MOCHA and $[\text{Ru}(\text{bpy})_3]^{2+}$ MeOH solution was mixed with 1 mL of H_2A aqueous solution in the reactor and purged with Ar gas for 10 min. The sample solution was illuminated using a 445 nm LED lamp (335 mW cm^{-2}), a sample of 200 μL was taken from the headspace and injected into the GC for quantification.

4.4.6 Apparent quantum yield (AQY) calculations

The apparent quantum yield (AQY), which is defined as the number of reacted photoelectrons (which for the HER is twice the number of H_2 molecules produced) divided by the number of incident photons at a given wavelength, was calculated according to formula below.

$$\text{AQY} = \frac{2 \times \# \text{ H}_2 \text{ molecules}}{\# \text{ photons}}$$

The total number of incident photons was calculated by measuring the power density of the incident beam using a PM100D (Thorlabs) power meter. By dividing this intensity value with the energy of a single photon of the wavelength (either 365 or 445 nm corresponding to 5.44×10^{-19} and 4.46×10^{-19} J, respectively), the total number of photons was calculated.

4.4.7 Photoelectrochemical test setup

4.4.7.1 Electrode preparation

Briefly, FTO electrodes ($3 \times 1 \text{ cm}^2$) were cleaned via ultrasonication for 15 min each in soap solution, DI water, and finally with EtOH. The cleaned electrodes were then dried at $60 \text{ }^\circ\text{C}$ and

masked on top 1×1 cm using Kapton tape, 30 min before use. Simultaneously, 10 mg of catalyst powder was dispersed in 200 μ L of isopropanol solution via ultrasonication for 15 min. Following this, \sim 100 μ L of this homogeneous suspension was drop-casted onto the masked FTO electrodes and allowed to dry at RT followed by drying at 60 $^{\circ}$ C for 30 min. The total electrode area covered with catalyst material was 2×1 cm².

4.4.7.2 Chopped light chronoamperometry tests

Chopped light-chronoamperometry tests were carried out in a single gas-tight cell using FTO glass, Pt plate, and Ag/AgCl (in 3M KCl) as the working, counter, and reference electrode respectively, dipped in 0.1M K₂SO₄ electrolyte solution. The solution was purged with N₂ for 1 h before testing. Chronoamperometry tests were done at 0V vs OCP with light on-off cycles with a 365 nm LED lamp in the case of composite samples. Each light on and off cycle was 60 and 15 s, respectively.

Chapter 5: TiO₂-based OIA: spherogels for photocatalytic H₂ production

This chapter explores a core-shell organic-inorganic architecture using a TiO₂ core and carbon shell, via a previously reported template assisted sol-gel process. In our study, we optimized the synthetic and photocatalytic conditions in order to obtain the highest performance towards the hydrogen evolution reaction. We unraveled the importance of the porosity and surface morphology of the OIA for good photocatalytic performance using a series of experimental and characterization techniques.

This work was carried out in collaboration with Dr. Michael S. Elsaesser from the Paris-Lodron-University of Salzburg, Austria. The synthesis and characterization of the hybrid material was carried out by him, and Dr. Jorge Torres-Rodríguez (shared first author) and the objective of the project was to demonstrate the advantages of constructing such an organic-inorganic architecture using TiO₂ and carbon for the photocatalytic hydrogen evolution reaction; as well as to understand the underlying mechanism behind its performance. The photocatalytic tests and optimizations were carried out here at TU Wien, and the samples went through a series of modifications, each involving either modifying the material composition or post-synthetic treatment, until we achieved high performance results towards photocatalytic hydrogen evolution.

The work presented in this chapter resulted in a successful publication titled “Titania hybrid carbon spherogels for photocatalytic hydrogen evolution” in the journal Carbon from Elsevier with DOI of [10.1016/j.carbon.2022.10.073](https://doi.org/10.1016/j.carbon.2022.10.073). The article is accessible under the CC BY 4.0 license.

My contribution as a shared first author involved the photocatalytic experimental design and optimization, data analysis, discussions, post catalytic analysis and paper writing.



Carbon

Volume 202, Part 1, 15 January 2023, Pages 487-494



Titania hybrid carbon spherogels for photocatalytic hydrogen evolution

Jorge Torres-Rodríguez^{a, b, 1}, Stephen Nagaraju Myakala^{c, 1}, Miralem Salihovic^a, Maurizio Musso^a

, Nicola Hüsing^{a, b}, Dominik Eder^c, Volker Presser^{d, e, f}, Alexey Cherevan^c  

Michael S. Elsaesser^a  

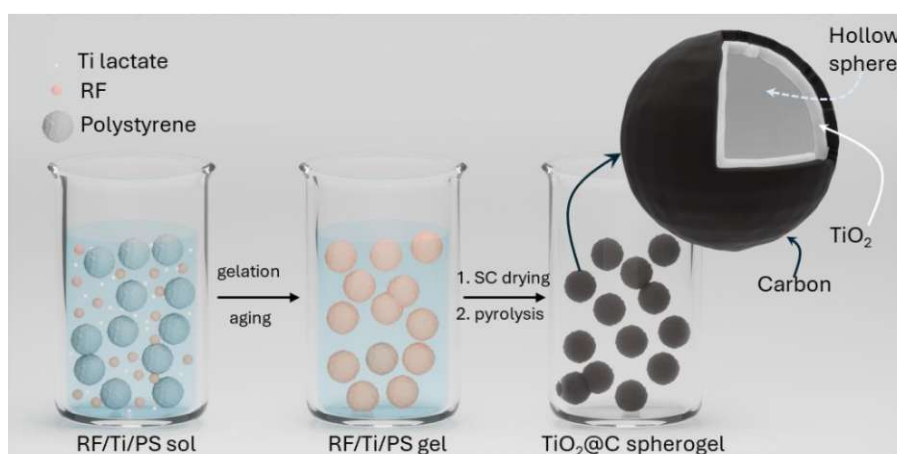
ABSTRACT

Recently, carbon spherogels have been introduced as a novel monolithic aerogel composed of hollow spheres. This material is conveniently obtained via polystyrene (PS) sphere templating. In the present study, we apply a water-soluble titania precursor (titanium(IV) bis(ammonium lactate)) to the aqueous sol-gel synthesis based on resorcinol-formaldehyde (RF) to effectively encapsulate titania. In this way, a very high mass loading of up to 59 mass% of titania can be confined strictly to the inside of the hollow carbon spheres. In the final synthesis step, carbonization at 800 °C has three simultaneous effects: Transformation of the RF coating on PS into microporous carbon, PS template removal by decomposition, and formation of titania due to precursor dissociation. A deliberate tuning of the microporous carbon shell, accessibility of the titania, titania amount, and titania's polymorph is further demonstrated by thermal treatment under a carbon dioxide atmosphere. In contrast to non-tuned or TiC-containing carbon spherogels, CO₂ activation of the composites results in a three orders of magnitude rise of their photocatalytic activity towards hydrogen evolution reaction, which we evaluate using flow and batch reactors. We further show that this effect is related to the partial etching of the carbon shell, which renders the TiO₂ surface accessible to the reactants in the solution and allows for an efficient hole scavenging. Given the simplicity of the hybrid carbon spherogel (HCS) composite fabrication, the high degree of control of their morphological characteristics, and the striking effects of CO₂-activation on performance, we believe that our results will contribute to the development of similar carbon-inorganic composites.

5.1 Introduction

As discussed in section 1.3.3.1, application of TiO_2 in photocatalysis is strongly limited by its large bandgap and more importantly the high recombination rate of the photogenerated charge carriers. Generally, several approaches of doping and functionalization with noble metal catalysts and/or other semiconductors have been developed to tackle this drawback. For instance, the classic TiO_2/Pt architecture is known to have a lower recombination rate due to the charge extraction by Pt NPs resulting in a superior photocatalytic performance. However, TiO_2 is also known to catalyse side and backward reactions, such as producing oxygen radicals using the photogenerated electrons or recombining the H_2 and O_2 into water. Moreover, these back reactions are only accelerated in the presence of catalyst materials like Pt, which are typically also used in fuel cells. Therefore, in addition to charge extraction, it is also critical to avoid the possibility of any side reactions. As an alternative, core-shell architectures constructed using $\text{TiO}_2@\text{C}$ can not only significantly improve the charge extraction, resulting in a substantial improvement in photocatalytic performance, but can also isolate the oxidation and reduction reactions to the TiO_2 and carbon surfaces, respectively.

Hollow carbon spheres or carbon spherogels are attractive template to build core-shell structures due to their high surface area, good conductivity, and uniform surface morphology.¹²⁴ These can be synthesized either using top-down approaches such as ball milling or be prepared using a bottom-up approach via sol-gel, solvothermal, or atomic layer deposition synthesis.¹²⁵ While top-down approaches are much easier to scale, they often lack control over the morphology, composition, and homogeneity of the core-shell architecture. Alternatively, bottom-up synthesis can easily overcome each of these drawbacks resulting in a well-defined core-shell architecture with the desired structure and morphology. Typically, these hollow carbon spheres can be prepared via a hard or soft templating method. Hard templating refers to the process of coating a hard spherical template such as SiO_2 or SnO_2 spheres with a carbon precursor which is carbonized at high temperatures, followed by chemical etching of the template.¹²⁵ While the soft templating approach in comparison provides the advantage of easy removal of templates like emulsion droplets and micelles, the hollow spheres produced often lack control on their morphology and are more polydispersed. However, hard templating provides a much more homogeneous and monodispersed product. Generally, SiO_2 is one of the most widely used hard template due to its chemical stability. However, this also makes it



Scheme 5.1 Illustration showing the synthesis process of preparing core-shell $\text{TiO}_2@\text{C}$ architectures via a hard template (polystyrene sphere), where the Ti/R-F (resorcinol-formaldehyde) coats the PS templates during the gelation and aging period followed by conversion to the $\text{TiO}_2@\text{carbon}$ shell during pyrolysis step

difficult to get rid of, requiring HF treatment to dissolve it resulting in a two-step synthetic process. Polymer based templates, such as polystyrene spheres, are an excellent alternative as they can be readily prepared at various desired sizes. Importantly, these templates decompose at temperatures as low as 400 °C, thereby resulting in a single step process for preparing hollow carbon spheres. In this chapter, we use a similar approach for the synthesis of TiO₂ encapsulated hollow carbon spheres, using polystyrene spheres as a template, as shown in Scheme 5.1. The negative surface charge of the polystyrene spheres and an appropriate titanium precursor was used to prepare a gel coating on the PS template followed by thermal treatment resulting in homogenous spheres of TiO₂@carbon core-shell architectures. Next, we explore these TiO₂@C OIAs and the effect of post synthetic treatments on their photocatalytic performance for the hydrogen evolution reaction.

5.2 Results and discussion

5.2.1 Structural and chemical characterization

Hybrid carbon titania spherogels (CTS) were synthesized using a previously reported method based on the gelation of resorcinol-formaldehyde (RF) assisted with a template of polystyrene spheres (PS), with a surface charge of around -20 mV measured using zeta potential analysis. The metal-oxide, TiO₂, was loaded onto the spherogels by the addition of a metal salts as a precursor during the sol-gel process. Typically, organometallic precursors such as Ti(IV)(acac)₂(OiPr)₂ are used due to their high solubility in isopropanol, however, their aqueous insolubility impedes its use in an water-alcohol mixture. Therefore, in our case we used a water-soluble Ti(IV)-salt, namely, titanium(IV) bis(ammoniumlactate) dihydroxide. Additionally, the negative surface of the PS provides an ample number of sites for the titanium (IV)-resorcinol species to arrange in a homogeneous manner. Scheme 5.1 shows a general scheme depicting the synthetic procedure used for the synthesis of titania loaded carbon spherogels. Briefly, the titania precursor is added to a solution mixture containing resorcinol, formaldehyde (F), and a certain mass percent of polystyrene spheres. It is important to note that the final drying step using supercritical CO₂ followed by carbonization under Ar atmosphere converts the RF coating to a microporous carbon layer, decomposes the titania precursor into small TiO₂ crystallites and finally also removes the PS template via thermal decomposition, resulting in carbon titania spherogels.

SEM and TEM imaging were used to analyze the surface morphology for each of the samples. Figure 5.1a shows the SEM image of the PS used as a template to prepare the hybrid spherogels. These show a uniform, relatively smooth surface with an average diameter of roughly 250 nm. Likewise, Figure 5.1a inset shows the average particle size distribution obtained using dynamic light scattering, with an average particle size centered around 275 nm. Next, in order to obtain a homogeneous core-shell nanoparticle, optimizing the synthetic conditions like pH and the concentration of PS, we observe that a PS mass of ~9% with respect to the amount of resorcinol-formaldehyde in the mixture at a pH value of 3 gave the best morphology, resulting in a uniform TiO₂ core evenly coated with a carbon shell, as shown in Figure 5.1b. In contrast to this, Figure 5.1c shows the SEM images of carbon titania spherogels obtained using a much lower PS mass % which resulted in a bimodal morphology of spheres along with the formation of RF nanoparticles. Furthermore, at pH values higher than 3 we observe either densely aggregated TiO₂ crystallites on the inner layer or a non-homogeneously dispersed TiO₂ nanocrystals, as shown in Figure 5.1d. This could most likely be due to the stability of the titanium precursor which is known to require acidic conditions for initiating hydrolysis, thereby resulting in uneven growth formation of TiO₂ in pH above 3.¹²⁶ Based on

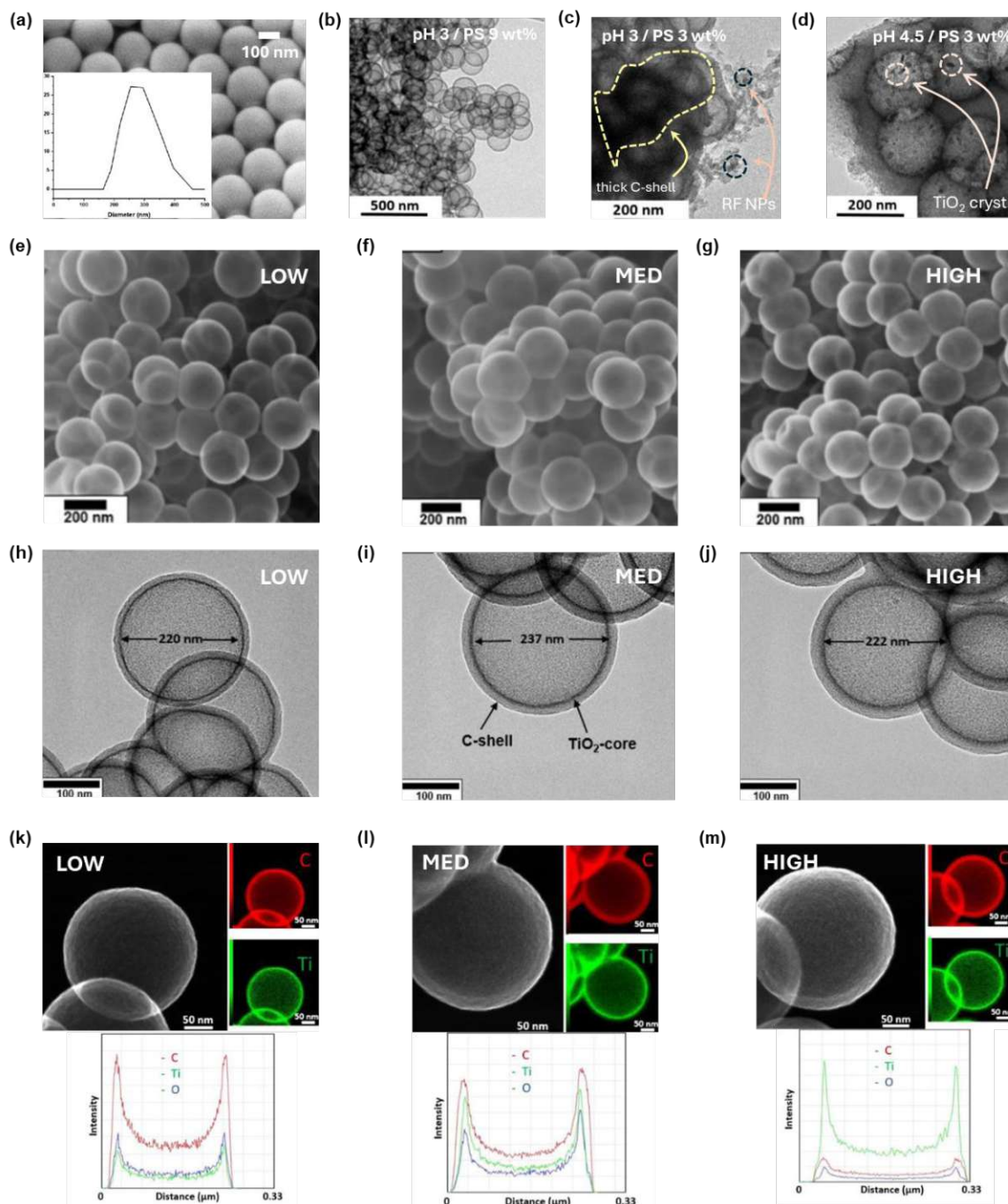


Figure 5.1 (a) STEM images of the polystyrene spheres used for templating (b)-(d) TEM images of hybrid carbon spherogels samples prepared by various synthesis parameters (e)-(j) SEM and TEM images of the CTS spherogels as obtained, Elemental analysis by STEM-EDX for elements Ti and C of three TiO₂-loaded carbon spherogels (LOW (k), MED (l), and HIGH (m)) as well as line scans across the hollow spheres for C, Ti, and O.

these optimized conditions, we prepared 3 sets of samples containing different amounts of TiO₂ denoted as CTS LOW, CTS MED, and CTS HIGH representing low, medium, and high loading samples. Figures 5.1e-g show the SEM images of these hybrids displaying uniform spheres with a continuous homogenous contact in the core-shell structure, which is extremely important for efficient charge extraction as discussed in section 1.3.3.2. We also observe no dependence of the final size of the carbon titania spherogels on the TiO₂ loading. Furthermore,

TEM imaging reveals the hollow TiO₂ sphere (core) coated with a uniform layer of carbon (shell), with an average interior diameter between 220 and 237 nm, which is expected due to shrinkage as compared to the 275 nm large polystyrene spheres. Complementarily, elemental analysis of Ti, C, and O via STEM/EDX scans across the diameter of the hybrids reveals a

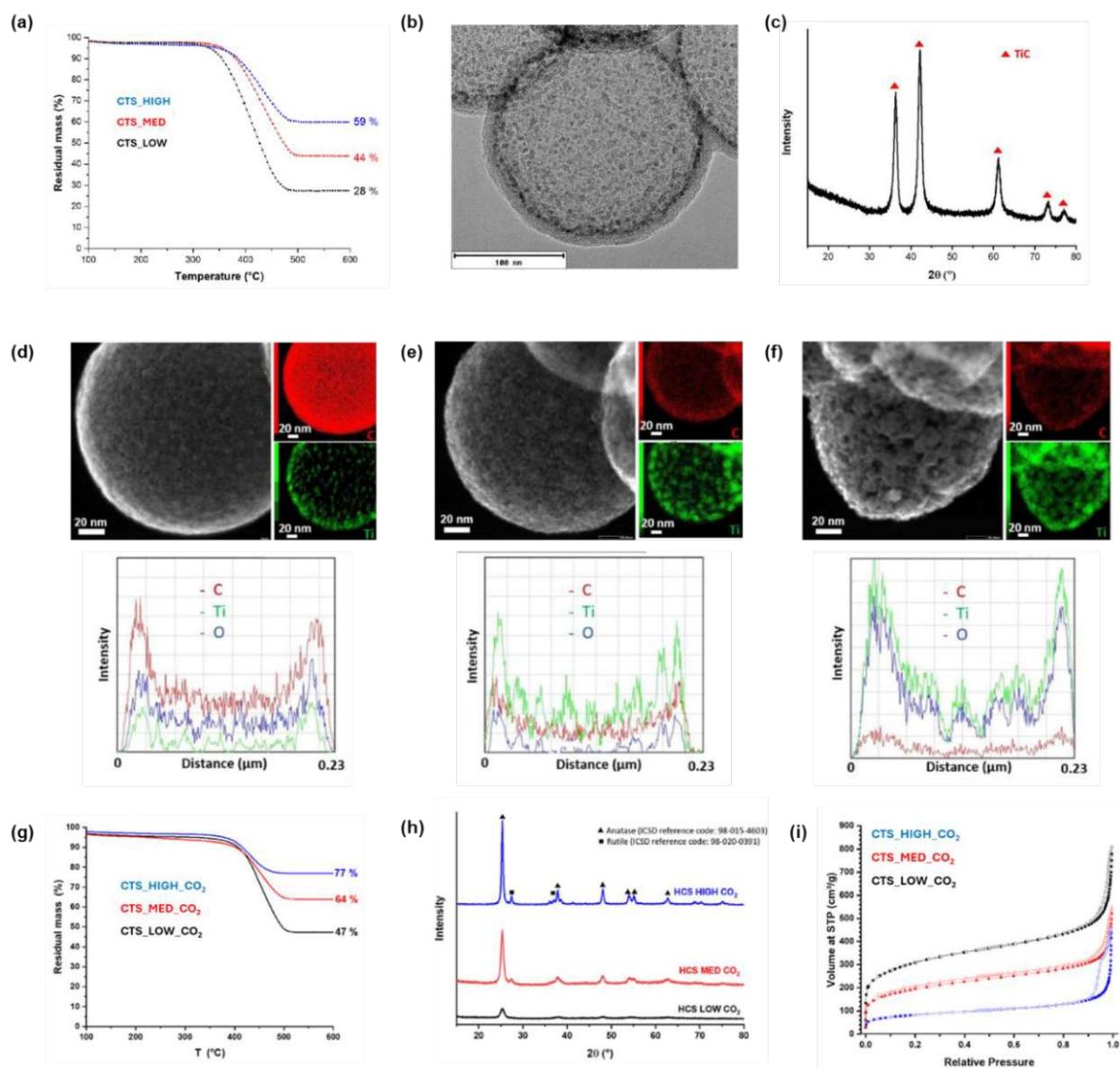


Figure 5.2 (a) TGA curves of pristine CTS samples loaded with different amounts of TiO₂ (b) HR-TEM of CTS_HIGH_Ar samples (c) XRD pattern of the CTS samples after annealing in Ar atmosphere, STEM images, elemental mappings, and cross-sectional elemental profiles of low (d), medium (e), and high titania (f) loaded spherogels after activation with CO₂ at 800 °C, 30 min (g) TGA curves (h) XRD pattern and N₂ sorption isotherm of CTS samples annealed in CO₂ atmosphere loaded with different amounts of TiO₂

continuous, nano-crystalline, uniformly sized titania layer surrounded by a homogeneous carbon layer, as shown in Figures 5.1h-j. Additionally, the signal intensities shown in Figures 5.1k-m corresponding to the concentration of each element showed the expected trend. The CTS_LOW loading samples show a higher C concentration in comparison to a small Ti signal, whereas similar intensity is observed for all components in the CTS_MED loaded samples and a higher Ti signal was observed in the CTS_HIGH sample. TGA analysis carried out in synthetic air atmosphere was used to estimate the amount of titania present in the spherogels. Figure 5.2a shows sharp drop between 350 to 450 °C, corresponding to the loss of the outer carbon

shell in the form of gaseous CO₂ and CO. Based on the remaining weight of the sample after this mass loss, assuming no change in the weight of TiO₂ in this temperature range, we estimated the amount of TiO₂ present inside the core as 28%, 44%, and 59% by mass for CTS LOW, MED, and HIGH, respectively. This result also demonstrates the effectiveness of this approach allowing for such a high loading of TiO₂ in a uniform manner.

In contrast to the pristine CTS, TEM images of samples annealed in Ar at 1100 °C showed a slightly bigger crystallite size (Figure 5.2b) which can be attributed to the high annealing temperature, as observed in a few other studies. Furthermore, XRD analysis of these samples shows peaks corresponding to TiC, as shown in Figure 5.2c. These peaks could arise from the formation of TiC at the core-shell interface. Similarly, CTS samples annealed in CO₂ atmosphere, denoted as CTS_LOW_CO₂, CTS_MED_CO₂, and CTS_HIGH_CO₂, at 800 °C also show an increase in the TiO₂ particle size between the range of 8 to 27 nm, as shown in Figure 5.2d-f. This variation in the size of the TiO₂ crystallites after thermal treatment is most likely due to the difference in the TiO₂ content in CTS_LOW, MED, and HIGH. Therefore, CTS_LOW_CO₂ shows the lowest amount of growth in the crystallite size since only a small amount of TiO₂ is present, which hinders any aggregation and growth process. Conversely, due to the large amount of TiO₂ content present, CTS_HIGH_CO₂ shows the largest growth of up to 27 nm in crystallite size. Furthermore, these images also show an etched carbon shell resulting in the generation of additional micropores. Since these pores are created via the loss of surface carbon, the ratio of TiO₂/C increases. In comparison to the untreated CTS, TGA analysis reveals a 30 % increase in the relative percentage of titania for each of the samples, as shown in Figure 5.2g. XRD analysis of samples after CO₂ treatment shows that the observed crystallite growth also effects the phase composition of the TiO₂ (core), where only pure anatase phase was observed in the CTS_LOW_CO₂ sample but CTS_MED_CO₂ and CTS_HIGH_CO₂ show a mixture of anatase and rutile phase, as shown in Figure 5.2h. Such behavior depending on the size of particles is reported in several other studies as crystallites smaller than 13 nm tend to thermodynamically favor the anatase form, however, larger crystallites initiate the formation of rutile phase. Table 5.1 shows the crystallite size for each of the samples after CO₂ treatment. N₂ adsorption isotherms were measured in order to evaluate the overall surface area and the nature of the pores after the thermal treatment of each of the CTS samples. Overall, we obtained a typical type II isotherm representing a micro/macroporous morphology, as shown in Figure 5.2i. Interestingly, CTS_LOW_CO₂ shows the highest N₂ uptake in micropores with a specific surface area (SSA) of 1149 m² g⁻¹, most likely due to the low amount of TiO₂ allowing for a more porous hybrid. In line with this, we observe a strong decrease in the SSA with increasing TiO₂ content with CTS_HIGH_CO₂ having a surface area of 271 m² g⁻¹. Typically, the large macropore (sphere interior) encapsulated by the microporous carbon shell would show a strong hysteresis effect due to the cavitation, however, since the hollow TiO₂ core blocks access to the inner cavity we do not observe such an effect for all TiO₂ loadings. Raman spectroscopy was used to understand the graphitic nature of the carbon shell by analysing the G- and D-band in the spectra which indicate the graphitic character and the defect intensity, respectively. Firstly, all CO₂ treated samples show two strong peaks corresponding to the D-mode (~1345 cm⁻¹) and G-mode (~1597 cm⁻¹) vibrations, representing a disordered, sp²-hybridised, partially graphitic-carbon material (Figure 5.3a). We also observed a peak ratio between A_d/A_g of around 2.5 which revealed the surface to be an incomplete crystalline material most likely as the amorphous carbon shell, as observed in similar resol-based carbon aerogels.¹²⁷ Moreover, when these peaks were further deconvoluted into 5 bands, namely, D, D*, D**, G, and D', the strong overlap of the D' and G peak revealed a disordered graphitic carbon material (Figure 5.3b). On

the other hand, we observe all four peaks of TiO₂ in the range of 150 to 650 cm⁻¹ for each sample (Figure 5.3a).^{128,129}

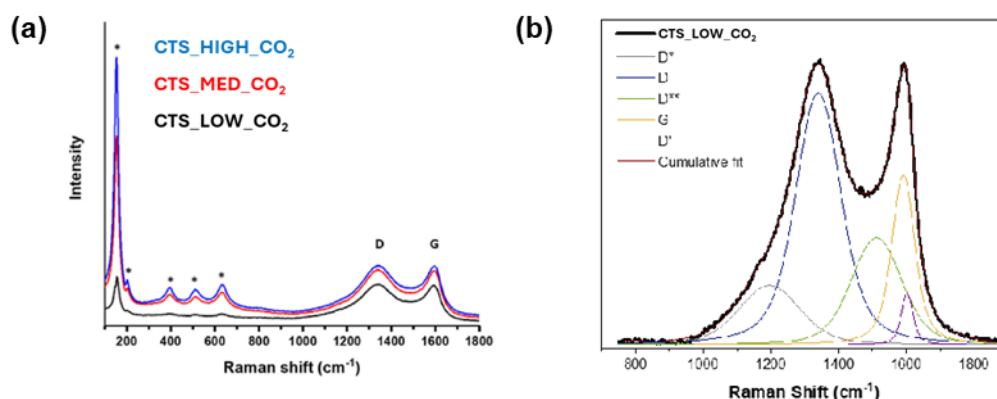
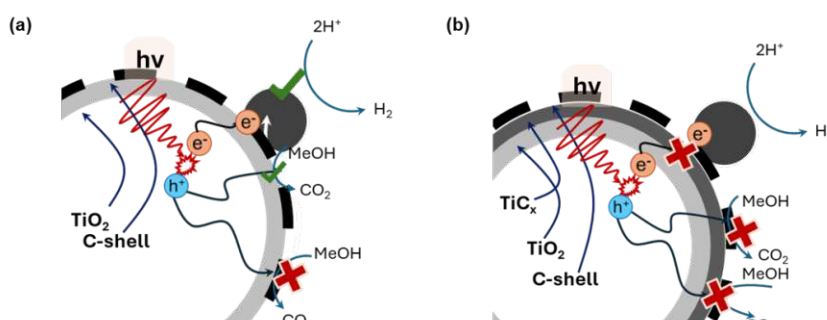


Figure 5.3 (a) Raman spectra of the CTS_CO₂ samples showing characteristic D and G-bands for graphitic carbon (b) Measured Raman spectra (black) and fitted spectra (red) of the activated hybrid CTS by deconvolution of the observed D- and G-bands into D* (grey), D (blue), D** (green), G (yellow), and D' (purple).

5.2.2 Photocatalytic hydrogen evolution

The photocatalytic hydrogen production performance of the pristine CTS samples, Ar annealed CTS, and CO₂ treated CTS was first evaluated in a closed batch reactor using a 365 nm LED as an illumination source, methanol as a sacrificial hole scavenger, and in-situ photodeposited Pt (1 wt%) as a co-catalyst on the CTS surface (see experimental details section 5.4).

Firstly, pristine CTS samples show almost negligible H₂ production (not shown in graph) with a 3-fold increase in the H₂ produced in the presence of co-catalytic Pt NPs (shaded bars), which shows the efficient charge transfer from the CTS to Pt NPs (Figure 5.4a). In the case of untreated-pristine CTS/Pt samples, all samples show comparable activity in the range of 3.8 and 4.8 nmol h⁻¹ with a slight increase in H₂ produced with increasing loadings of TiO₂. This could be due to insufficient consumption of photogenerated holes by the sacrificial agent (MeOH), in contrast to the photogenerated electrons, that are effectively extracted to the Pt co-catalyst via the carbon shell. This can lead to self-oxidation of the CTS and increased charge recombination. However, since the porous nature of the untreated CTS allows for some amount of MeOH to diffuse to the TiO₂ core, we observe a small amount of H₂ produced but the rate of MeOH diffusion could be insufficient and thereby the limiting step towards H₂ production, as shown in scheme 5.2a. Interestingly, all samples heated in Ar atmosphere show



Scheme 5.2 (a) Schematic showing the importance of MeOH diffusion through the porous shell for consumption of the photogenerated holes (b) schematic depicting the effect of annealing the sample in Ar possibly forming a layer of TiC at the interface of the core-shell, acting as a charge trap and also blocking MeOH diffusion, ultimately resulting in the drop in HER performance.

a drastic drop in their photocatalytic performance by almost 30-40% of the pristine activity, however, the trend of higher H₂ amounts from higher TiO₂ sample was still retained. This strong reduction in the photocatalytic performance can be mainly attributed to the formation of TiC at the interface as observed from XRD analysis, where the TiC layer can typically have a metallic nature and act as a trap for the photogenerated electrons¹³⁰, while also further hindering MeOH diffusion to the TiO₂ core, as shown in Scheme 5.2b.

In contrast to the detrimental effect of annealing in Ar, the CTS samples treated in CO₂ atmosphere showed an excellent HER performance, with an increase of over 2 orders of magnitude, as compared to the pristine CTS samples. This activation can be attributed to the partial etching of the carbon shell during the annealing, improving the overall surface area

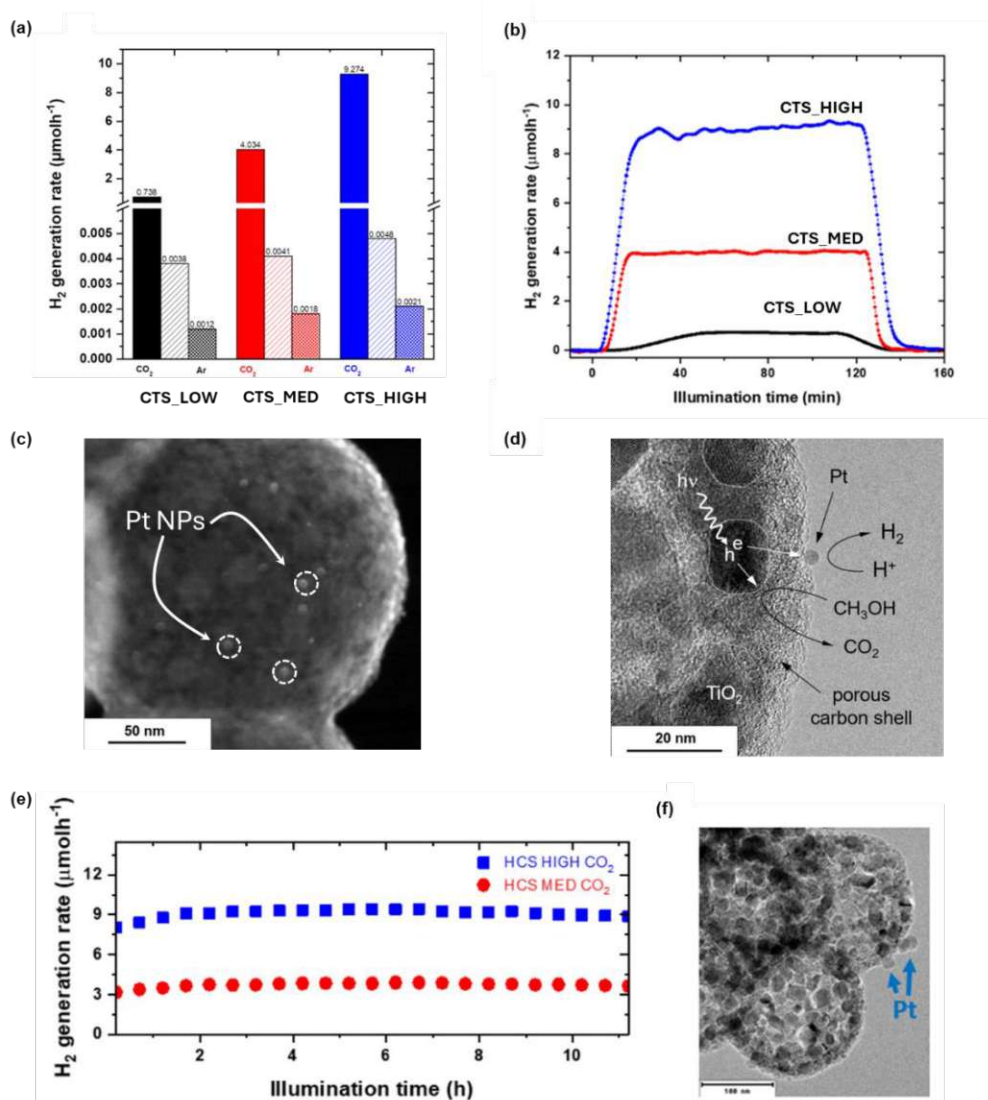


Figure 5.4 (a) Rates of H₂ evolution obtained for the as-prepared (hatched bars), 1100°C annealed (half-tone bars), and CO₂-activated (full bars) CTS hybrids, (b) H₂ evolution profiles measured for the CO₂ activated composites with low, medium and high TiO₂ contents, (c) Post-catalytic TEM analysis of Pt-loaded CTS samples showing the intact surface where Pt NPs can be seen as bright spots on the surface of the carbon shell (d) photodeposited Pt nanoparticle on the outer part of the shell showing the location of Pt NPs (e) H₂ generation rates plotted as a function of illumination time measured in long-term HER experiments exemplifying the most active CTS photocatalysts with medium (64 mass%) and high (77 mass%) TiO₂ contents (C) (f) TEM image of CTS_MED_CO₂ after 12 h of illumination under turnover conditions.

(from BET measurements) and MeOH diffusion to the TiO_2 core. Once again, increasing the amount of TiO_2 resulted in a higher amount of H_2 produced, that is $\text{CTS_HIGH} > \text{CTS_MID} > \text{CTS_LOW}$, however here the trend is non-linear suggesting that the improved performance is not only due to the higher surface area and higher number of catalytic centres but also due to better accessibility of the TiO_2 core for consumption of the photogenerated holes via methanol oxidation. To further elucidate this behaviour, all samples were tested in a flow-type reactor setup, where the produced hydrogen is constantly carried to a detector using Ar gas (see experimental details section 5.4). Such a setup provides insights into the rate of hydrogen evolution at all times as compared to the batch reactors which are limited to one- or two-point measurements. Figure 5.4b shows that the HER rates measured in the flow setup are comparable to the values obtained from the batch reactor experiments. Furthermore, we observe a stable H_2 production over an illumination period of 2 h without any degradation in performance. Typically, Pt NPs that are deposited in-situ on the surface of TiO_2 (in the absence of any shell) tend to be mobile resulting in the growth of the Pt NP which causes a strong decrease in the photocatalytic HER performance. However, the absence of any decrease in our HER rate suggests that the carbon-shell could also be preventing the growth of Pt NPs.³⁷ Figures 5.4c,d show high resolution TEM images of the samples post catalysis. Firstly, we observe no changes to the surface or bulk morphology of the CTS_CO_2 samples and secondly, we clearly see the preferred location of the Pt NP deposition on the outer carbon shell. In the high-resolution image, we observe bright spots corresponding to small Pt NPs on the outer part of the shell close to the TiO_2 crystallite, suggesting that the photogenerated electrons in TiO_2 are transferred and released at the C-solution interface and simultaneously the photogenerated holes are consumed via the diffused MeOH. Finally, to demonstrate the long-term stability of the prepared OIA, we tested two of the best performing samples, namely - CTS_MID_CO_2 and CTS_HIGH_CO_2 , in the flow-reactor setup. Figure 5.4e shows that both samples can stably produce H_2 for over 12 h of illumination without any loss of performance. Moreover, TEM images show no changes in the morphology of samples after 12 h of UV-illumination and no difference in the Pt NPs as compared to the samples after 2 h illumination (Figure 5.4f).

5.3 Conclusion

To summarize, this chapter explores a versatile synthesis approach for preparing a hollow-core OIA consisting of a carbon sphere shell with a hollow TiO_2 core. The approach allowed us to have fine control over the morphology on the final TiO_2 -C hybrid via PS sphere templating. We also demonstrate the importance of the reaction parameters such as pH of the solution and the RF dilution ratios in order to obtain a homogenous composition in the final hybrid. Importantly, template removal via thermal treatment provides a simpler and safer alternative as compared to other silica-templating approaches which require the use of hydrofluoric acid to generate the hollow carbon spheres. Next, we tested these hybrids for their photocatalytic HER performance and unravel the effect of thermal treatment in different atmospheres resulting in different morphology dependent activity. We observed a decrease in the performance for samples annealed in Ar atmosphere which was attributed to the formation of a TiC layer at the interface of TiO_2 and carbon, whereas treatment in CO_2 atmosphere resulted in a strong activation of the sample and thereby an improvement in the HER performance by over 2 orders of magnitude. This improvement was achieved via partial etching of the outer carbon shell allowing for better diffusion of MeOH into the pores, thereby resulting in better consumption of photogenerated holes. Furthermore, the core-shell nature prevents the

agglomeration/growth of Pt NPs resulting in a stable performance for over 12 h of illumination without any changes in the sample structure or chemical composition.

5.4 Experimental section

5.4.1 Synthesis of polystyrene spheres and CTS

The polystyrene (PS) spheres were synthesized according to a previously reported procedure from Du et al. using an emulsion polymerization reaction between styrene and potassium persulfate initiator, and polyvinylpyrrolidone added as a stabilization agent.¹³¹ The obtained PS sphere solution was diluted to a concentration of 9% by mass. Next, this aqueous PS solution was used as a templating agent for the carbon spherogels.

5.4.2 Synthesis of carbon spherogels

To prepare the organic gels, the resorcinol (R, carbon source) was dissolved in 25 g of 9% PS solution under mild magnetic stirring for 10 min. Consecutively, appropriate amounts of the titanium precursor titanium(IV) bis(ammonium lactate) dihydroxide (1.2 g (LOW), 2.5 g (MED), and 3.7 g (HIGH)) was added dropwise into the solution while continuously stirring for 10 min. Following this, formaldehyde (F) was slowly added such that the molar ratio of F/R is 1.5, followed by the addition of the NaCO₃(C) to catalyze the reactions. The final ratios between F/R/C/Ti was 1.5/52/0.6. Next, 2 N HNO₃ aqueous solution was added to adjust the solution pH to 3, which was then stirred for 1 h. Afterward, the solution mixture was poured and sealed in cylindrical glass vials and placed in an oven for aging for 7 d at 80 °C. Following this, the gels were washed using acetone (3 times), where fresh acetone was exchanged every 24 h, to remove any remaining unreacted species or unwanted by-products. Next, after the solvent exchange procedure, the wet gels were dried by supercritical extraction with CO₂ at 60 °C and 11 MPa. Finally, the obtained organic aerogels were carbonized in a tube furnace (alumina tube) in a controlled Ar atmosphere (75 NL h⁻¹) at 800 °C with a heating ramp of 60 °C h⁻¹, and a dwell time of 2 h. Upon cooling at room temperature, monolithic carbon spherogels were obtained. Post-synthetic heat treatment was followed by one of the following methods: (1) Physical activation with carbon dioxide (quality 4.5) in a tube furnace (800 °C, 600 °C h⁻¹, 30 min, 1 mL min⁻¹ CO₂ flow) or (2) annealing under argon atmosphere at 1100 °C for 120 min (Ar quality 5.0).

5.4.3 Photocatalytic experiments

The hydrogen evolution experiments were carried out using a side-illumination slurry type reactor (total volume of 9 mL) equipped with a monochromatic UV LED light source with an incident light intensity of 0.49 W centered at 365 ± 6 nm (196 mW cm⁻², SOLIS, Thorlabs). The experiments were performed either in a batch-type or a flow-type mode. The temperature of the reactor solution was maintained at 15 °C using a water-cooling system (Lauda). The reaction solution was stirred at 650 rpm throughout the experiment. In a single run, 1 mg of the powdered photocatalyst was first dispersed in 2 mL of 1:1 by volume MeOH:H₂O mixture by ultrasonication for 180 s. The mixture was transferred to the reactor; 125 µL of aqueous H₂PtCl₆ solution was added, corresponding to 10 µg (1 mass%) Pt employed here as H₂ evolution co-catalyst. The solution was purged with Ar (flow rate of 15 mL min⁻¹, controlled with a mass flow controller from MCC-Instruments) to remove dissolved oxygen before starting the illumination. In a batch-type mode, products of the photocatalytic reaction accumulated in the reactor volume; the amount of evolved H₂ was analyzed with a GC-2030 (Shimadzu) instrument using a Micropacked-ST Column (ShinCarbon) and a barrier discharge ionization detector (BID). Sampling was done using a gas-tight syringe (Hamilton).

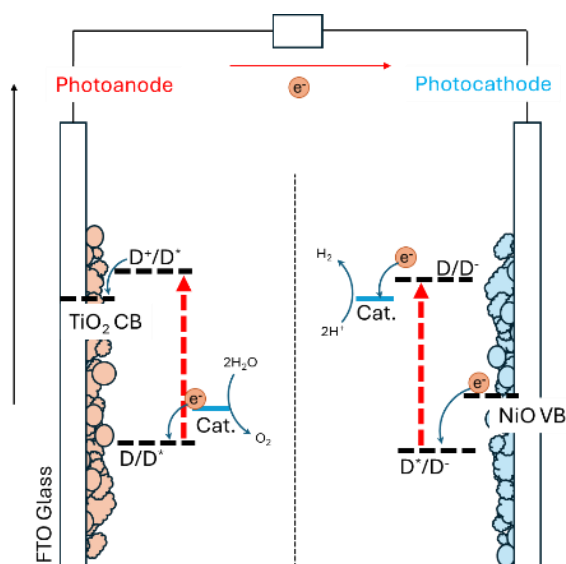
In the online detection flow-type mode, to deliver the products of the photocatalytic reaction to the detector, the reactor was continuously purged with Ar carrier gas at a flow rate of 15 mL min⁻¹. The gaseous H₂ was detected directly in the stream by an online gas analyzer (X-stream, Emerson Process Management) equipped with a thermal conductivity detector. For both detectors, H₂ concentrations were deduced based on a multilevel calibration. A typical H₂ evolution profile was obtained in flow-mode which includes an induction period (increasing H₂ evolution rate during the first 10 min) that corresponds to the time required by H₂ gas to fill the dead volume (e.g., reactor volume, tubing volume) to reach the detector. After this induction, H₂ evolution reached a stable rate, which speaks for stable HER performance. In contrast, when the rate changes over time, (de)activation of the photocatalytic system can be deduced. When the illumination stopped, the signal returned to the baseline.

Chapter 6: NiO-based OIAs: Dye sensitized photocathodes for photoelectrocatalytic H₂ production

This chapter explores the H₂ production potential of a 3-component photocathode as an OIA prepared using inorganic mesoporous NiO, visible light absorbing organic dyes, and inorganic molecular catalysts. This work was carried out as part of a 3-month research stay in collaboration with the group of Dr. Vincent Artero and Dr. Murielle Chavarot at the CEA research center, Grenoble. Since the present work is still in progress, the results discussed in this chapter are predominantly from the catalytic experiments carried out at CEA and are focused on electrode preparation, followed by testing their photoelectrocatalytic performance as feedback for improvement in the construction/electrode preparation phase. Overall, the work aims to demonstrate the advantage of constructing such an organic-inorganic architecture for applications outside of pure photocatalysis as well.

6.1 Introduction

During photocatalytic water splitting, the direct conversion of solar energy into chemical energy is the most desirable outcome. Developing catalyst materials for this process, which are efficient, robust, sustainable and most importantly economically scalable, is still a major challenge. Meanwhile photoelectrocatalytic (PEC) water splitting coupled with PV cells (as an electricity source), provides an immediate and scalable solution due to two reasons, first, a PEC cell often requires a lower applied potential bias than most electrolysis cells and; second, it improves charge separation and isolates the individual reactions on different electrodes thereby reducing any side or back reactions resulting in a significant improvement in the overall catalytic performance. However, in order to realize this, it is crucial to develop and optimize photosystems that require the least amount of external bias providing maximum possible performance. In 1972, Fujishima and Honda were the first to demonstrate this concept using a chemically and structurally stable TiO_2 electrode for photoelectrocatalytic water splitting, however, the wide bandgap of TiO_2 strongly limited its potential. As we have seen in Chapter 2, organic linkers can be used as visible light absorbing centers in MOFs. A similar approach for decorating TiO_2 electrodes with light absorbing molecules creating an organic-inorganic architecture can overcome its downside of poor visible light absorption. For example, the pioneering research of O'Regan and Grätzel on dye sensitized solar cells (DSSCs) made using nanocrystalline TiO_2 , not only showed such an architecture to work but also led to new developments in the field leading to dye-sensitized photoelectrocatalytic cells (PECs). Building on this, in 1999, Meyer et al. were the first to use a nanoporous TiO_2 photoanode functionalized with a molecular dye catalyst reporting a visible light photocurrent response of a titania-based electrode.¹³² Consequently, in the same year, Lindquist et al. also reported a dye-sensitized photocathode using NiO with excellent visible light photocurrent response showing the electron transfer from the NiO valence band to the visible light excited dye molecule.¹³³ Building on this, over a decade later, Sun et al. demonstrated the first earth abundant photosystem, using NiO, an organic dye, and cobalt catalyst, for the photoelectrocatalytic production of hydrogen.¹³⁴



Scheme 6.1 Illustration showing the individual steps of photoexcitation of electrons and interfacial charge transfer at different solid-solid interfaces in a photoelectric cell under illumination.

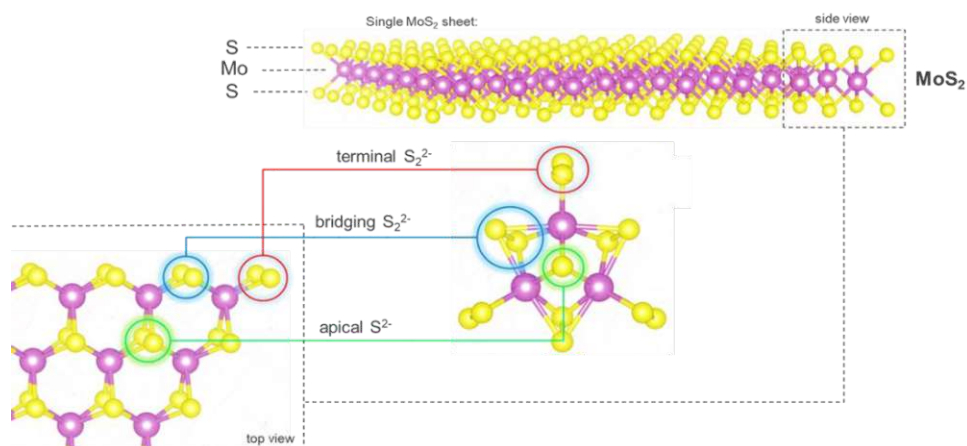
These studies and developments substantiate the advantages of using organic-inorganic architectures for PEC water splitting, isolating the role of (I) light absorption, (II) charge separation, and (III) catalysis on different components. Scheme 6.1 shows the general setup

of such an organic-inorganic architecture based photoelectrodes making a dye-sensitized PEC (DS-PEC) cell. In this type of cell the photocathode and the photoanode are made out of metal oxides (for chemical stability) as inorganic substrates functionalized with organic dye molecules (for visible light absorption) and molecular catalysts (for water splitting). Typically, light absorption happens in the dye molecule (D) forming an excited state (D^*). This excited state generally has its highest occupied molecular orbital (HOMO) level more positive than the valence band of the metal oxide used as the photocathode (reduction side), like NiO in the present work, thereby readily accepting an electron and leaving behind a hole in the semiconductor. Similarly, the dye molecule anchored onto the metal oxide surface of the photoanode, has its lowest unoccupied molecular orbital (LUMO) level more negative than the valence band (VB) of metal oxide like TiO_2 . This allows electron transfer from D^* to the CB of TiO_2 . This process is responsible for the improved electron hole separation creating the $D^-/\text{NiO}(h^+)$ state on the photocathode. These holes then diffuse through the NiO to the back contact, typically a FTO glass substrate, towards the photoanode completing the circuit. Finally, the excited electron on D^- is transferred to a catalyst either dissolved in the electrolyte or anchored onto the surface via adsorption and/or covalent linkage to the dye.

Depending on the type of majority charge carriers and defect nature, metal oxides can be classified as either n-type or p-type semiconductors. For instance, the oxygen vacancies in a TiO_2 crystal result in an excess of electrons in the Ti 3d orbitals that make up the conduction band thereby turning it into an n-type semiconductor, whereas Ni vacancies in a NiO particles increase the number of holes in the VB making it a p-type semiconductor. Since n-type semiconductors have an excess of electrons which are mobile opposite to the direction of the applied field, they typically form the photoanode (oxidation site) whereas p-type semiconductors form the photocathode (reduction site) in a DS-PEC. While there are many stable n-type semiconductors like TiO_2 , WO_3 , BiVO_4 , etc., there are only a few stable p-type semiconductors like NiO and Cu_2O . Due to this, there have been many more advancements in the development of photoanodes in comparison to photocathodes which are currently the limiting factor towards achieving a high-performance PEC cell. Among the materials used to construct photocathodes, NiO is the most stable and widely studied material since its synthesis does not require high temperatures and therefore can be produced in an economically scalable approach. Additionally, since it is a wide bandgap semiconductor it does not compete with the dye molecules for light absorption. Based on these properties, NiO is an attractive choice for the photocathode material.

Another important component in the photocathode construction using NiO is the dye molecule used for sensitization. In order to achieve an efficient charge transfer from NiO to the dye, its most important property is that the HOMO level which should be lower (more positive) than the valence band edge of NiO. For example, organic dyes like PB6 or metal organic dyes like $\text{RuP}_4^{\text{OEt}}\text{-bpy}$ have their HOMO level at 1.03 V and 0.81 V, respectively, both more positive than the valence band edge of NiO (0.4-0.5 V) making them a suitable match.^{135,136} Secondly, the dye molecules should also have a high extinction coefficient in order to maximize light harvesting. Typically, organic dyes have a much larger absorption coefficient compared to organometallic dyes such as $[\text{Ru}(\text{bpy})_3]^{2+}$, predominantly due to the more favorable $\pi-\pi^*$ transitions in the former case as compared to the metal-to-ligand charge transfer (MLCT) mechanism responsible for the main absorption in the latter. Therefore, organic photosensitizers can be seen as more promising candidates when constructing photocathodes due to our ability to fine tune their light absorption and charge delocalization, making them a suitable fit.

Finally, the last important component for an efficient visible light absorbing NiO photocathode is the catalyst which is responsible for enhancing the kinetics of the desired reaction. It can either be dissolved in the electrolyte solution or immobilized onto the electrode surface. While the first option is a practically easier approach, the electron transfer from the dye to the catalyst is often slow since its diffusion controlled, and it further limits the pool of potential catalysts to materials which are soluble in aqueous solutions. In the case of catalyst immobilization, they can be either attached on the surface of the metal oxide (NiO) or anchored onto the dye molecules. Here, the latter provides a direct pathway for the photogenerated electron to the catalyst molecule, and the former requires the catalysts molecule to be immobilized in proximity of the dye for efficient electron transfer. In both cases, it is advantageous to anchor the catalysts directly onto the photocathode as opposed to dissolved in the solution. Presently, noble metal catalysts such as Pt and Au, either in the form of molecular complexes or nanoparticles, have shown the highest performance towards PEC hydrogen production.^{137–139} However, their limited availability, and high extraction costs make them expensive and



Scheme 6.2 Illustration showing comparison between the edge sites of a MoS₂ sheet and a molecular analogue [Mo₃S₁₃]²⁻ cluster

unsustainable. In this regard, earth abundant transition metal chalcogenides, especially MoS₂, have emerged as an attractive alternative, since it is chemically and structurally stable under a wide range of operating conditions. While inactive towards catalyzing the HER in its bulk form, nanoparticulate or exfoliated MoS₂ has been reported as efficient electrocatalysts for hydrogen production.^{112,140,141} In 2007, Jaramillo et al. for the first time explored the active sites responsible for this electrocatalytic behaviour using exfoliated MoS₂ revealing the MoS₂ edges to be the active sites.¹⁴² Following this, several reports showed that molecular analogues of the general formula of MoS_x (like [Mo₃S₁₃]²⁻, [Mo₂S₁₂]²⁻) clusters representing similar Mo-S coordination (Scheme 6.2) as that of a MoS₂ edges also showed excellent performance towards electro- and photo-catalytic hydrogen evolution.^{143–145}

In this chapter, we construct an OIA as a photocathode, built using mesoporous NiO functionalized with either of two visible light absorbing dyes, [Ru(bpy)₃]²⁺ and P1, and a MoS_x catalyst. While both dyes were anchored using phosphonate groups, we employ wet impregnation and electrodeposition techniques to deposit the MoS_x catalyst, using (NH₄)₂Mo₃S₁₃ as a precursor. We then explore this OIA for the photoelectrocatalytic hydrogen evolution reaction.

6.2 Results and discussion

6.2.1 Photocathode optimization

All photocathodes were prepared on conductive FTO glass (4x2 cm) which was coated with NiO using NiCl₂ solution as a precursor based on a previously reported solvothermal process as described in the experimental section 6.4. Next, two dyes, namely [Ru(bpy)₃]²⁺ and P1, were separately grafted onto the NiO film, via wet impregnation by soaking the electrode in a dye solution overnight. The catalyst MoS_x was deposited in two different ways – via drop casting and electrodeposition in order to optimize an anchoring technique for efficient charge transfer and thereby achieve the best performance. Finally, each of these OIA films were tested using two electrochemical techniques, namely linear sweep voltammetry (LSV) and chronoamperometry (CA), both under illumination and dark conditions. The LSVs were used to determine the lowest potential bias required such that the photocurrent response is the highest, under illumination, by comparing the photocurrent response of each electrode. Based on this, a fixed potential bias was applied during PEC tests.

Before diving into the electrochemical tests, each of the synthesized films was characterized using XRD to confirm the formation of NiO on the electrode and XPS to understand the chemical environment on the surface of the electrode. Figure 6.1a shows the XRD diffractograms of the NiO film on FTO. We observed all peaks corresponding to NiO

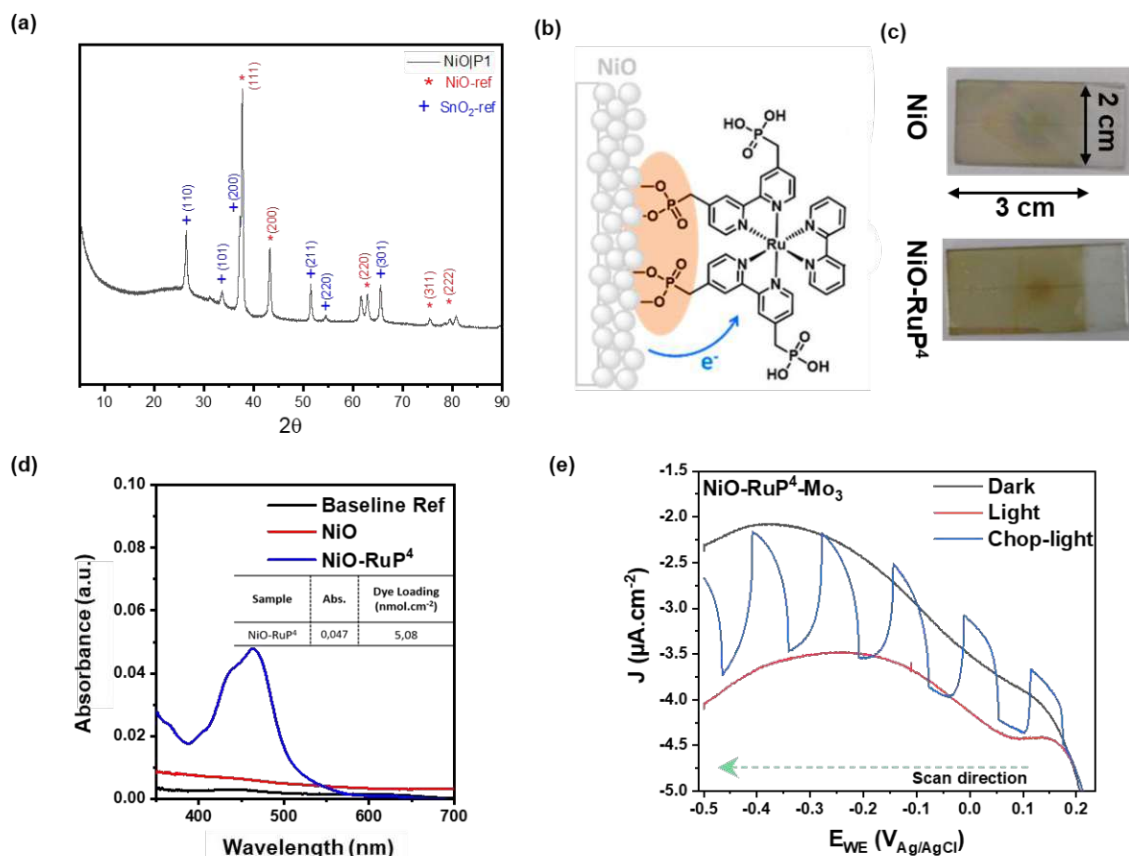


Figure 6.1 (a) XRD pattern of pristine NiO film prepared on FTO (b) schematic depicting the photocathode construction using NiO substrate grafted with Ru-based dye via phosphonate linkage. (c) optical images of the electrodes before and after grafting with the dye. (d) UV-Vis absorption spectra of the dye dissolved in methanolic solution of phenyl phosphonic acid (inset table shows the absorption intensity and the corresponding dye loading). (e) LSV scans of the NiO|RuP₄|Mo₃(drop casted) electrode in dark, light, and chopped light illumination using a solar simulator set to 0.65 sun

(ICDD: 04-002-0950) along with several major peaks from SnO₂ (ICDD: 04-003-5853), which confirms successful formation of the desired NiO/FTO architectures.

6.2.1.1 Photoelectrocatalysis using Ru-based dye

Following the successful synthesis of NiO, we first grafted it with a widely used visible light absorbing [Ru(bpy)₃]²⁺ dye modified with 4 phosphonate groups that act as anchor points via covalent linkage to the NiO film, as shown in Figure 6.1b. Figure 6.1c shows the image of the film before and after grafting the dye onto the NiO film, which appeared darker and more opaque as compared to the pristine NiO film. Since the organic dye molecules can be hard to visualize in their molecular form and even more difficult to quantify, we employed an indirect approach for the quantification of the adsorbed dye. First, we dissolved the dye by dipping the electrode in a 0.1 M phenyl phosphonic acid solution for 6 h which caused the dye molecules to desorb from the surface of the film. The solution was then measured using UV-Vis spectroscopy focused on the dye absorption at ~455 nm. Subsequently, five solutions of known dye concentrations were prepared, and their absorption intensities were used to prepare a calibration curve. This curve was then used to calculate the amount of leached (and thus grafted) dye on our NiO electrodes. Figure 6.1d shows the UV-Vis spectrum of the phosphonated-[Ru(bpy)₃]²⁺ (RuP⁴) desorbed from the electrode into the methanolic solution of phenyl-phosphonic acid, corresponding to a dye grafting value of ~ 5.08 nmol cm⁻². Once we confirmed the successful anchoring of the dye, we used a drop casting approach to graft the catalytic MoS_x clusters on the NiO|RuP⁴ electrodes using a methanolic solution of (NH₄)₂Mo₃S₁₃ precursor along with a small amount of Nafion to stabilize the drop casted film. In this case, 10 nmol of the catalyst was drop casted onto the electrode aiming to keep a ratio of 2:1 between the catalyst and dye species. Figure 6.1e shows the XRD pattern of the film after drop casting the clusters. We observed no changes in the peaks corresponding to NiO, neither were any new peaks corresponding to the clusters observed. This could be either due to low loading of the clusters onto the film or due to the molecular nature of the deposition as compared to agglomeration of the clusters into small crystals. Once the photocathode was prepared, we tested its dark and light current response via LSV in 0.1M Britton Robinson buffer solution at pH 3. Figure 6.1e shows the LSV curve obtained in dark, light, and under chopped light illumination. While the photocathode shows a clear photocurrent response, it was only able to achieve a maximum of 1.5 μA cm⁻² at -0.4 V vs Ag/AgCl. Such behavior is most likely due to inefficient electron transfer from the photoexcited dye molecule to the MoS_x cluster that leads to a higher number of charge recombinations. This problem can be tackled via two pathways, first, improving the charge carrier lifetime within the dye molecules and second, improving the interaction between the dye molecules and MoS_x clusters. The following sections explore both these solutions in a stepwise manner.

6.2.1.2 Photoelectrocatalysis using P1-dye

Next we explored a commercially available metal-free organic dye P1 which upon excitation has a better charge separation due to a push-pull effect. Briefly, a P1-dye molecule consists of a triphenylamine which acts as an electron donor moiety while the malononitrile present is an electron withdrawing group separated by thiophene units in the conjugated chain, as shown in Figure 6.2a. When excited under visible light illumination, the presence of these moieties aids with the electron flow from the donor to the acceptor part of the dye, which not only improves charge separation but separates the electrons from the interface with the p-type NiO. These properties make it an excellent choice for efficient charge separation and reduce the recombination rate, and thereby also allowing in theory the MoS_x clusters to effectively extract the photogenerated electron. Like in the previous procedure, NiO electrodes were dip coated

in a methanolic solution of P1 overnight to achieve an adsorption-desorption equilibrium. Figure 6.2b shows the optical images of the electrodes before and after dye-grafting. We clearly see a strong coloration of the film due to the dye presence, which was further confirmed and quantified using UV-vis spectroscopy. In comparison to $[\text{Ru}(\text{bpy})_3]^{2+}$, we observed almost 50% higher amount of dye grafted onto the NiO surface (Figure 6.2c). Next, $[\text{Mo}_3\text{S}_{13}]^{2-}$ was drop casted onto the prepared NiO|P1 electrode. XRD analysis of the NiO electrodes after grafting with P1 and subsequent catalyst deposition showed no changes in the pattern (Figure 6.2d). Due to the low catalyst loading no characteristic peaks were observed from the hybrid electrode. Nonetheless, LSVs of the NiO|P1| MoS_x electrodes showed a photoresponse of $\sim 10 \mu\text{A cm}^{-2}$ at an applied potential of $-0.5 \text{ V vs Ag/AgCl}$ ($\text{pH} = 3$), as shown in Figure 6.2e. This increase in the photoresponse is a clear indication of the improvement in the charge separation and charge consumption likely attributable to the push-pull nature of the dye. The performance of the prepared electrodes for their photoelectrocatalytic H_2 production was characterized using chronoamperometry measurements under visible light illumination using a solar simulator (0.65 sun , $400 < \lambda < 700 \text{ nm}$). Based on the LSV results, we chose -0.4 V (vs Ag/AgCl) as the applied potential since it gave the highest photocurrent response, with negligible increase in the current density with higher voltage. Figure 6.2f shows the

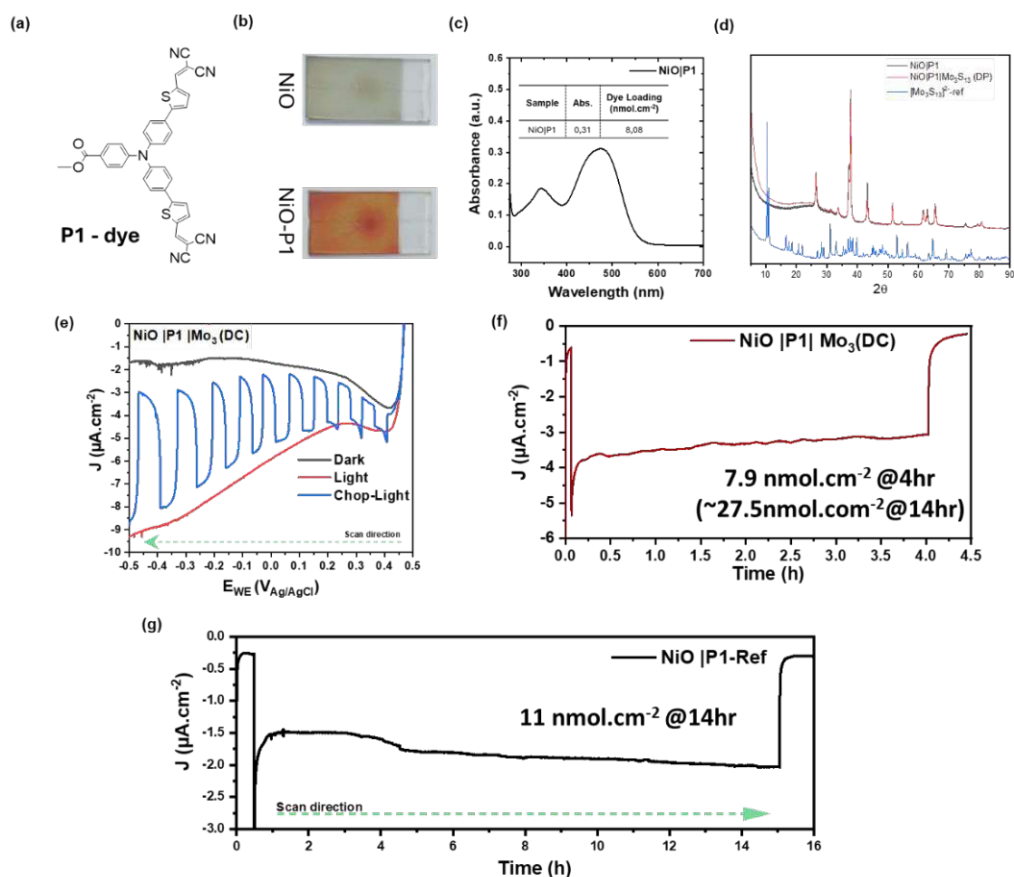


Figure 6.2 (a) Structural representation of P1 dye (b) optical images of the NiO electrodes before and after the grafting of P1-dye (c) UV-Vis spectrum of P1-dye dissolved in methanol (inset table showing the absorption intensity and the corresponding dye loading) (d) XRD pattern of the electrodes before and after dye grafting along with reference spectra of pristine $(\text{NH}_4)_2\text{Mo}_3\text{S}_{13}$ precursor powder (e) LSV curves of NiO|P1| Mo_3S_{13} (drop casted) in light, dark, and chopped light illumination (f) chronoamperometric curves of NiO|P1| $\text{MoS}_x(\text{DP})$ and (g) NiO|P1-ref over a period of 4 and 14 h, respectively.

chronoamperometric curves revealing a sharp photoresponse in the first minute of illumination while reaching a steady photocurrent of $\sim 4 \mu\text{A cm}^{-2}$ after 30 min.

The photocathode was illuminated for a period of 4 h, followed by sampling the headspace using a GC, to quantify the amount of hydrogen produced. Firstly, the electrode shows negligible change in the photoresponse producing a total of $\sim 8 \text{ nmol cm}^{-2}$ after 4 h of illumination. In comparison to this, reference experiments carried out in the absence of any MoS_x catalyst showed a $\sim 50\%$ lower photocurrent producing only 11 nmol cm^{-2} after 14 h of illumination (Figure 6.2g). Therefore, these results demonstrate that firstly, the dye is efficiently able to separate the photogenerated charges and secondly, these charges can be transferred to the catalytic active sites in the MoS_x cluster to promote H_2 generation.

While the overall amount of H_2 produced was ~ 3 times higher when using P1 and MoS_x , the majority of the improvement can be clearly attributed to better charge separation in the P1 molecule, which brings us to the second step of improving the MoS_x -dye interaction. Therefore, we explored an alternative immobilization strategy of electrodepositing the clusters onto the dye-sensitized NiO electrode. Recent studies on the electrodeposition of various MoS_x clusters such as $[\text{Mo}_3\text{S}_{13}]^{2-}$, $[\text{Mo}_2\text{S}_{12}]^{2-}$, and $[\text{MoS}_4]^{2-}$ have shown them to have excellent electrocatalytic performance for hydrogen evolution. For instance, Moutet et al. were the first to employ this approach where they electrodeposited amorphous MoS_x onto a photocathode made using

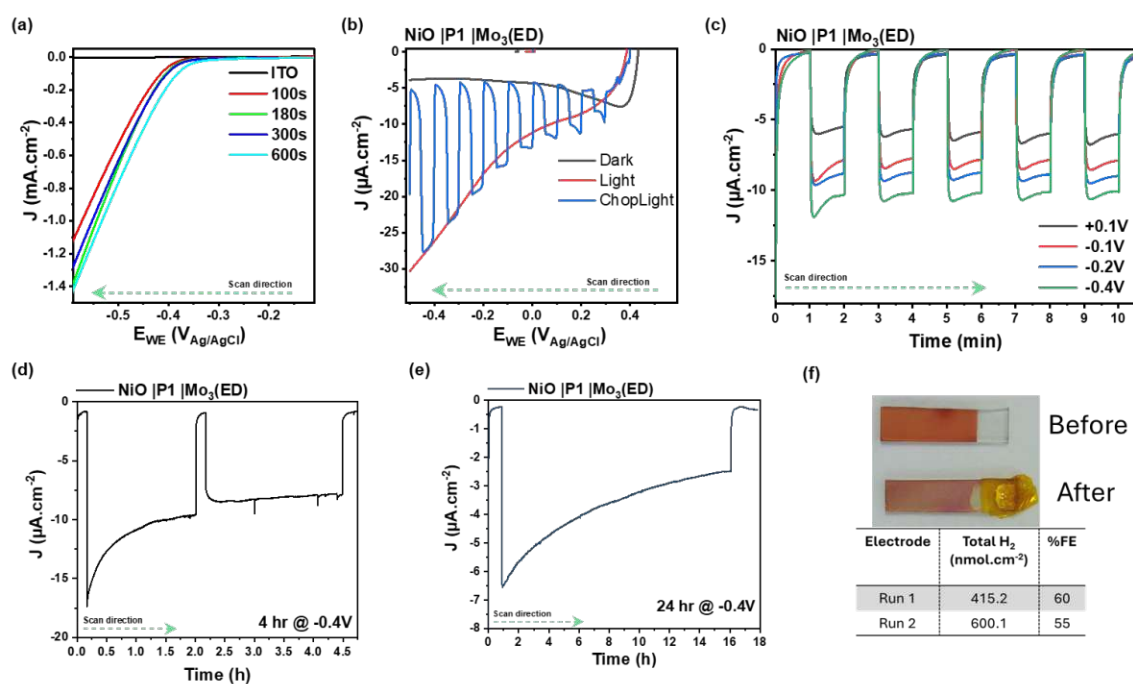


Figure 6.3 (a) LSV curves of MoS_x on ITO glass deposited using four different electrodeposition times (b) LSV curve of photocathodes prepared via electrodeposited MoS_x in light, dark, and chopped light illumination (c) chopped light chronoamperometric measurements recorded using of NiO|P1| $\text{Mo}_3(\text{ED})$ at different voltages vs Ag/AgCl (d) chronoamperometry curve of the first run for the PEC test using NiO|P1| $\text{Mo}_3(\text{ED})$, (e) second chronoamperometric test showing the second cycle of the electrode testing and (f) optical images of the photocathode before and after 24 h PEC test along with table showing the amount of H_2 produced in each cycle.

glassy carbon and polypyrrole- $\text{Ru}(\text{bpy})_3^{2+}$ and tested it for electrocatalytic HER. They observed a strong photocurrent of over $40 \mu\text{A cm}^{-2}$ at low pH.¹⁴⁶ In a similar approach, Li et al. demonstrated control over the ratio of the deposited Mo:S via electrodeposition, which they further showed to play a key role in the number active adsorption sites and the overall

electrocatalytic performance.¹⁴⁴ They observed that depending on the type of electrodeposition, cathodic, anodic, or via cyclic voltammetry, the resultant MoS_x had a different Mo:S ratio and also different type of S coordination. Based on these studies we explored and optimized the electrodeposition approach to anchor MoS_x onto the NiO|P1 electrode using $(\text{NH}_4)_2\text{Mo}_3\text{S}_{13}$ as a precursor salt.

6.2.2 Electrodeposition optimization and PEC tests

Electrodeposition was carried out using a standard 3 electrode system using ITO glass as a working electrode, Pt mesh as a counter electrode, and Ag/AgCl (3M KCl) as a reference electrode. Four electrodes were prepared using different electrodeposition time from 100 s to 600 s at an applied bias of +0.19 V vs Ag/AgCl (pH 5) using 1mM solutions of $[\text{Mo}_3\text{S}_{13}]^{2-}$ precursor dissolved in 0.1M NaClO_4 . Figure 6.3a shows the LSV curves of the prepared electrodes in 0.5 M H_2SO_4 without any illumination. We observe a similar HER onset potential in all of the samples with the lowest onset values in the case of MoS_x deposited for 600 s. However, a similar current density is achieved by the electrode prepared via deposition for 180 s. Therefore, since the lowering of the onset potential is negligible as compared to the photocurrent difference between 180 and 600 s, we decided the optimized electrodeposition time of 180s at +0.19 V vs Ag/AgCl (pH 5). This protocol also ensures that we prevent formation of a thicker MoS_x layer which might later start leaching into the reaction solution. Figure 6.3b shows the LSV curves of photocathodes prepared by electrodepositing MoS_x onto NiO|P1 electrodes denoted as NiO|P1| $\text{Mo}_3(\text{ED})$ representing the $[\text{Mo}_3\text{S}_{13}]^{2-}$ precursor. In comparison to the drop casted electrodes, which were able to achieve a photocurrent response of $10 \mu\text{A cm}^{-2}$, the electrodeposited electrodes were able to achieve over double the photocurrent of as much as $\sim 25 \mu\text{A cm}^{-2}$, which is over 20 times higher than that of pristine NiO|P1 electrodes. While one of the main factors for this improvement in performance is due to enhanced charge transfer, the electrodeposited MoS_x would also have a different Mo:S ratio as compared to drop casted ones resulting in different number of active sites, which will be elucidated via XPS analysis in future studies. Figure 6.3d shows the chronoamperometric curves of this electrode. Over a period of 4 h of illumination, the sample produced $\sim 415 \text{ nmol cm}^{-2}$ of H_2 with a faradaic efficiency of 60%, which is 50 times higher than the amount of H_2 produced via drop casting approach. However, recycling the same electrode for another 16 h of illumination was only able to produce an additional 600 nmol cm^{-2} in this time with the photocurrent dropping to almost $3 \mu\text{A cm}^{-2}$ (Figure 6.3e). Furthermore, the optical image of the electrode before and after testing showed a clear change in colour suggesting a change in the structural and chemical properties of the electrodeposited clusters, leaving room for further improvement.

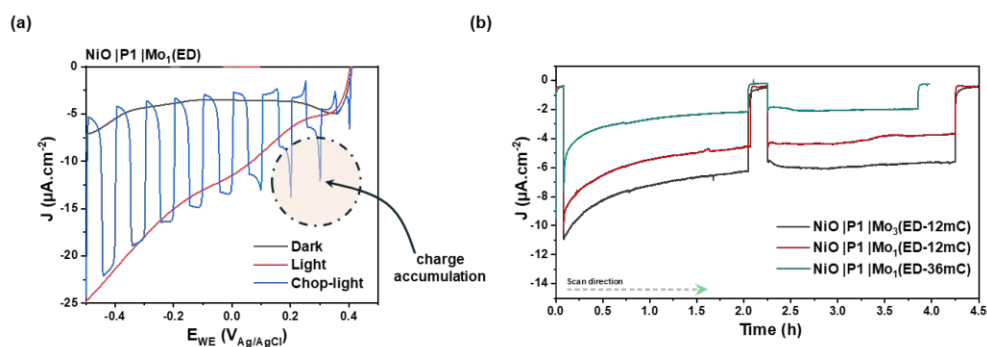


Figure 6.4 (a) LSV curves of NiO|P1| $\text{Mo}_1(\text{ED})$ in the dark, light, and chopped light illumination using a solar simulator (b) chronoamperometry curves recorded on NiO|P1| Mo_3 and Mo_1 photocathodes in a Britton-Robinson buffer at pH 3 at -0.4 V (vs Ag/AgCl)

Table 6.1 Summary of all the values corresponding to the dye loading on each of the best performing electrode, the amount of H₂ produced in the headspace and the solution along with the charge passed during PEC test; and the faradaic efficiency (FE) and turn over number (TON) in each case

	E _{dep} -charge (mC)	Time(h)	Dye loading (nmol.cm ⁻²)	H ₂ in the headspace (nmol)	H ₂ in the solution (nmol)	Total H ₂ (nmol.cm ⁻²)	charge passed (mC.cm ⁻²)	FE(%)	TON
NiO P1	-	14	8,7	30	0	10	96,6	2,3	1,5
NiO P1 Mo ₃	11,3	4	8,5	570	60	211,28	95,6	43	24
NiO P1 Mo ₁	12	4	8,5	630	70	231,46	70,6	61	27
NiO P1 Mo ₁	36	3.8	8,5	150	30	60,37	31,6	37	7

Before exploring strategies to improve the photocathode stability, we compare it with a similarly prepared photocathode using [MoS₄]²⁻ which is another widely studied molecular analogue of active edge sites of MoS₂. Figure 6.4a shows the LSV curves obtained from NiO|P1|MoS_x photocathodes in dark and light, which were prepared via MoS₄ electrodeposition and denoted as NiO|P1|Mo₁(ED). It is important to note that in order to keep the electrodes comparable, the amount of charge consumed was kept the same during the deposition process using both [Mo₃S₁₃]²⁻ and [MoS₄]²⁻. Interestingly, we observe a similar photocurrent density from Mo₁(ED) photocathodes and Mo₃(ED), however, at lower (reductive) potential bias's we observe a sudden spike in the peak current due to charge accumulation in the chopped light LSV scan (Figure 6.4a), while no such photocurrent response was observed in the case of Mo₁(ED) electrodes. This behaviour could be explained by the polymerization of the [Mo₃S₁₃]²⁻ cluster via the loss of terminal sulphides in the initial stage of applying potential which uses the photogenerated charges at lower potential bias. This could explain the low faradaic efficiency of the Mo₃(ED) photocathodes since part of the electrons are in this case used in the cluster transformation and MoS_x formation. Figure 6.4b shows the chronoamperometric tests of NiO|P1 electrodeposited from Mo₃ and Mo₁ precursors. We observe a slightly higher photocurrent response from the Mo₁ deposited sample which could be either due to lower amount of MoS_x deposited on the surface thereby avoiding any agglomeration or leaching effects; or could be that the MoS_x deposited from [MoS₄]²⁻ presents a higher number of Mo active sites as compared to the MoS_x deposited using [Mo₃S₁₃]²⁻. Interestingly, Mo₁ deposited using 3 times higher charge, i.e. 36 mC, resulted in a worse performance, confirming that oversaturation of the surface may have negative effect on the performance. Table 6.1 shows that both best performing electrodes produce similar amounts of H₂ and similar turnover numbers (TONs) of 24 and 27 recorded for each of these photocathodes with NiO|P1|Mo₁ and NiO|P1|Mo₃, respectively. These results suggest that irrespective of the precursor used for electrodeposition, the final form of MoS_x strongly depends on the charge consumed during the deposition, which seems to play an important role in the overall PEC performance (Table 6.1).

6.3 Conclusion

To summarize, this chapter explores an OIA photocathode prepared using NiO, an organic light-sensitizer, and an inorganic catalyst (MoS_x), and reports its performance for the photoelectrocatalytic H₂ production. Two different visible light absorbing sensitizers were used, first a Ru-based dye, and second a fully organic dye called P1. The photocathodes prepared using P1 showed a higher photocurrent response due to better charge separation of the photogenerated carriers due to the push-pull effect from the different electron donor and acceptor groups in the dye molecule. Using the NiO|P1 architecture, catalyst MoS_x was

deposited onto the photocathode using two approaches, namely drop casting and electrodeposition. In comparison, photocathodes prepared using optimized electrodeposition conditions resulted in a 1.5 times higher photocurrent response which can be attributed to improved charge transfer to the MoS_x cluster. Furthermore, they also show a 30 times higher H_2 production rate with a relatively stable performance for over 4 h of testing with a faradaic efficiency of 45%. Further modifying the OIA by depositing a thin layer of Al_2O_3 , via ALD, onto the photocathode resulted in a doubling of the faradaic efficiency with similar H_2 production values. Overall, these results show that preparing a OIA photocathode via this approach can provide a stable and efficient photocatalyst system. However, further characterization is required to fully understand the chemical and structural changes in the electrodeposited MoS_x , and the interfacial interactions between each component of the OIA photocathode.

6.4 Experimental section

6.4.1 Synthesis of NiO films on FTO

NiO films were prepared via a sol-gel process and deposited onto FTO substrates by spin coating. Briefly, 2 g of anhydrous NiCl_2 , 2 g of F108 triblock co-polymer were added to a solution mixture containing 6 g DI water and 12 g ethanol. The powders were dissolved by ultrasonication for 12 h to obtain a homogeneous solution. Following this the solution was centrifuged at 4500 rpm for 20 min, followed by filtering the supernatant using a syringe filter to remove an undissolved precursor in the solution. The filtered solution was spin coated onto FTO coated glass substrates ($7 \Omega \text{ cm}^{-1}$) at 5000 rpm for 1 min. These films were sintered at $450 \text{ }^\circ\text{C}$ for 30 min with a heating ramp of $\sim 15 \text{ }^\circ\text{C min}^{-1}$. The spin coating and annealing was repeated 4 times per electrode.

6.4.2 Dye-anchoring onto NiO films

Dye molecules were anchored onto the NiO films via a wet impregnation method. Each film was dipped in 10 ml of methanolic dye solution (0.1 mM) and kept on an orbital stage 4 h to evenly saturate the NiO film with the dye molecules. Following this, the film was washed by dipping in fresh methanol solution and stirring on the orbital spinner for 30 mins and dried naturally.

6.4.3 Synthesis of $(\text{NH}_4)_2\text{Mo}_3\text{S}_{13}$

The ammonium thiomolybdate clusters were prepared using a modified synthetic approach using microwave heating. Briefly, 250 mg of ammonium molybdate tetrahydrate ($(\text{NH}_4)_6[\text{Mo}_7\text{O}_{24}]\cdot 4\text{H}_2\text{O}$) and 187.5 mg hydroxylamine hydrochloride ($\text{NH}_2\text{OH}\cdot\text{HCl}$) were added to 5 mL of ammonium sulphide solution in a 30 mL microwave vial. This mixture was stirred for 30 minutes followed by heating at $150 \text{ }^\circ\text{C}$ for 20 min at a stirring rate of 600 rpm in a microwave (Anton parr monowave 300). The bright red product was filtered, washed with 50 mL of water, ethanol, CS_2 and ether and dried in air at $60 \text{ }^\circ\text{C}$.

6.4.4 Electrodeposition and photoelectrocatalytic setup

All experiments were carried out in a home-made 3-electrode reactor setup, using NiO photocathode, Pt wire/mesh, and Ag/AgCl (3 M KCl) as the working, counter, and reference electrodes, respectively. All measurements were done using a BioLogic SP300 potentiostat controlled via EC-Lab V10 software.

In the case of electrodeposition, 0.5 M aqueous solution of $(\text{NH}_4)_2\text{Mo}_3\text{S}_{13}$ dissolved in 0.1 M NaClO_4 was used as the deposition solution, at pH ~ 6 . MoS_x was electrodeposited onto the NiO|dye electrodes by applying a potential of +0.01V vs Ag/AgCl for various time periods of

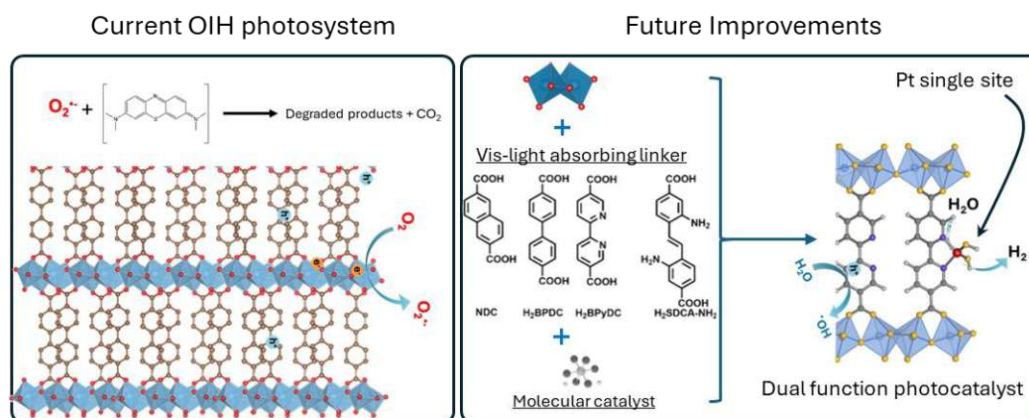
100, 180, 300, and 600 s. These electrodes were then characterized by LSVs in 0.5 M H₂SO₄ to identify their onset potential for HER.

PEC testing was carried out in the home-made reactor using a Britton-robinson buffer solution (pH = 3) and a 300 W ozone-free Xe lamp (Newport) equipped with a IR (> 800 nm) and UV (< 400 nm) cut-off filter, operated at 280 W set to the intensity power of 0.65 sun as a light source. Before each run, the reactor was purged with N₂ for 30 mins to get rid of any dissolved oxygen, which was further confirmed by sampling 50 μL of headspace using a gas chromatograph (GC, Perkin Elmer Clarus 580). After purging, 3 LSV measurements were carried between +0.5 and -0.5 V vs Ag/AgCl at a scan rate of 10 mV s⁻¹ under dark, light, and chopped light conditions to record the initial photocurrent response from the electrode. PEC tests were done using chronoamperometry at -0.4 V vs Ag/AgCl (3M at pH = 3) with an initial 10 min in the dark followed by illumination for 4 h. After this, 50 μL of gas was removed from the headspace and injected into the GC to quantify the amount of H₂ produced.

Chapter 7: Conclusions and outlook

This thesis aimed at exploring the advantages of using organic-inorganic hybrid materials as efficient photocatalysts for dye degradation and H₂ production. As introduced in Section 1.3, these hybrid materials can be prepared in different ways and further classified based on the dimensions (molecular or bulk) of its individual components. Overall, four hybrid photosystems were tested: one each from class A (TiO₂@C spherogels) and class C (NiO|P1 photocathodes), and two from class D (Ti-MOF, Ag-MOCHA) type hybrids.

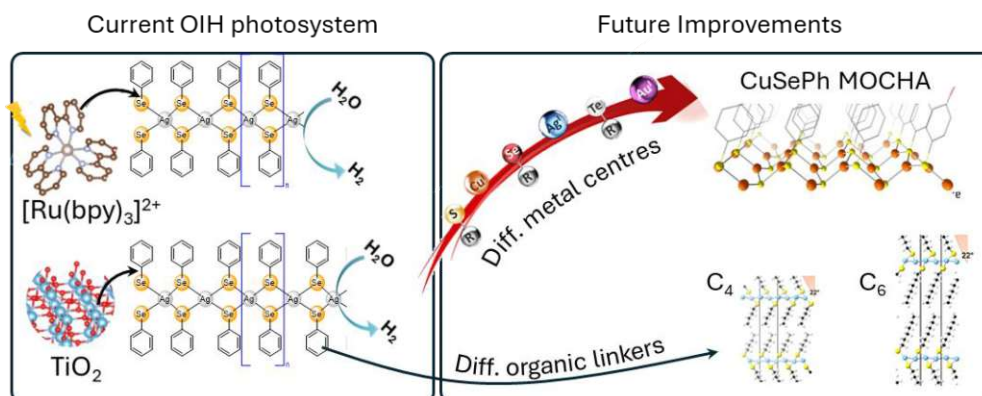
In Chapter 3, we studied a Ti-based MOF as a hybrid comprised of Ti-oxo clusters linked together via organic linker molecules. The hybrid showed a higher surface area and visible light absorption as compared to inorganic pristine TiO₂. Moreover, it also showed excellent photocatalytic performance towards selectively degrading positively charged dye pollutants such as MB, CV, and TB under visible light irradiation. This behavior was mainly attributed to the negative surface charge due to surface terminating organic ligands, specifically, the dangling COO⁻ groups present in the linker. The higher surface area and the strong electrostatic interactions also allowed the hybrid to have a higher dye adsorption capacity as compared to TiO₂. Therefore, the improvement in several physical and optoelectronic properties of the hybrid demonstrate some of its advantages as compared to pristine inorganic materials (such as TiO₂). However, further studies aimed at functionalizing the linker molecules to achieve higher visible light absorption and also provide anchor points for co-catalytic species could drastically improve the potential of such a hybrid yielding a photosystem capable of simultaneous water treatment and H₂ production, as shown in Scheme 7.1.



Scheme 7.1 Left showing the illustration of using COK-47 as a photocatalyst for visible light driven dye degradation and right showing the further potential to modify the organic linker molecule to incorporate inorganic catalysts atoms or molecules for simultaneous dye degradation and hydrogen evolution

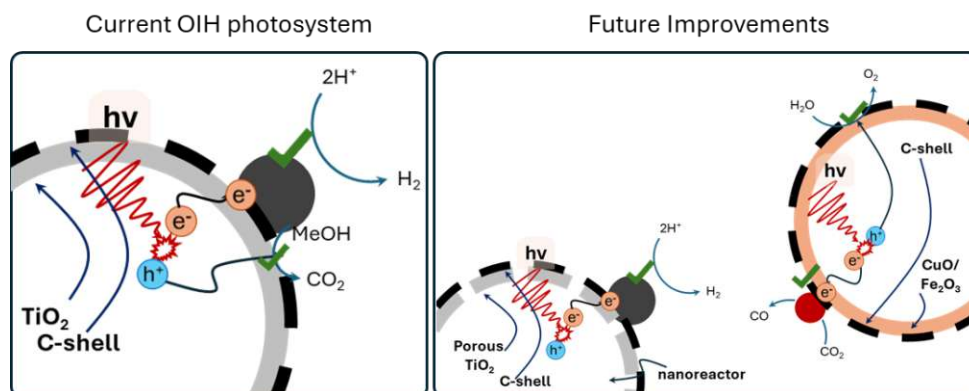
In Chapter 4, as another class-D hybrid, a set of Ag-based MOCHAs were prepared and tested as co-catalysts for the hydrogen evolution reaction. The layered nature of the hybrid allows for a higher surface area and all three MOCHAs, namely, AgSePh, AgSPh, and AgTePh (Ph = C₆H₅), showed excellent H₂ production under UV and visible light irradiation, using TiO₂ and [Ru(bpy)₃]²⁺ as photosensitizers. While the interaction with TiO₂ resulted in an initial transformation to a MOCHA/Ag⁰/TiO₂ sandwich like structure, the dynamic interaction with [Ru(bpy)₃]²⁺ resulted in a more stable sensitization process yielding relatively stable H₂ production rates without any structural or chemical transformation. These results combined show the photocatalytic performance of the hybrid co-catalyst comprised of a layered structure

of 2D-[Ag-Se-C₆H₅] network, and potentially other similar OIHs. Building on these results, similar strategies can be used to prepare MOCHAs using other metal centers such as Cu, Au, etc., which could be active for the CO₂ reduction reaction. Moreover, the structural and optoelectronic properties of these class of OIHs can also be improved by using other organic functional groups which facilitate better reactant anchoring sites, while also fine tuning the optical absorption properties, as shown in Scheme 7.2.



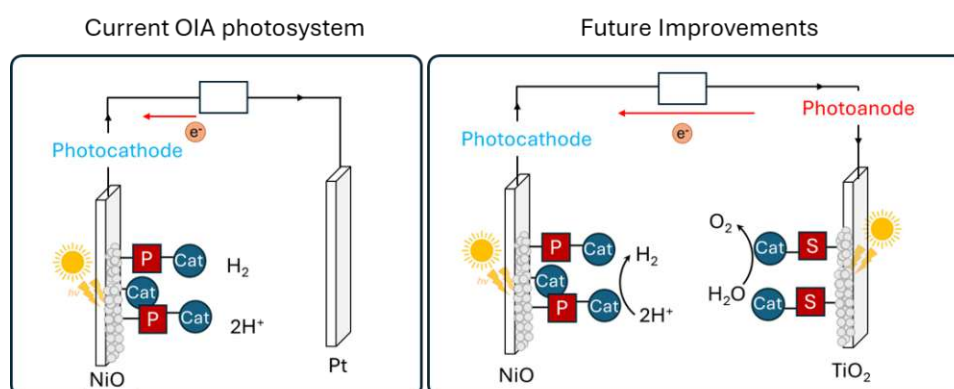
Scheme 7.2 Left showing the current Ag-MOCHA photosystem for H₂ production using [Ru(bpy)₃]²⁺ and TiO₂ as photosensitizers and right showing the potential alternatives of using longer organic linkers for tuning the optoelectronic properties or changing the core metal from Ag to Cu based MOCHA for other applications like CO₂ reduction

In Chapter 5, a simple core-shell TiO₂@C OIA was shown as an excellent photocatalyst for stable H₂ production without any structural or chemical changes after long periods of testing. Most importantly, the post synthetic treatment of the carbon shell in different inert or reactive atmospheres resulted in a different surface morphology and porosity which played a key role in the final photocatalytic performance. Overall, the study provides a important results which can be further extended to prepare core-shell architectures using other metal oxide/sulfides for various photocatalytic applications. Furthermore, based on these outcomes, the TiO₂@C OIA can also be further improved via two major modifications, as shown in Scheme 7.3. First, improving the graphitic nature of the carbon shell, presuming that it will result in a major improvement in the charge extraction from TiO₂ and have better conductivity overall, and second, modifying the synthetic precursor which can result in a porous TiO₂ core as well, thereby allowing the use of the hollow TiO₂ core as a nano/micro-reactor, which is known to improve the reaction kinetics.



Scheme 7.3 Left showing the core-shell TiO₂@Carbon architecture for hydrogen evolution and right showing a schematic for extending the approach to other metals like CuO and Fe₂O₃ for application in CO₂ reduction reactions or oxygen evolution reaction, respectively.

In Chapter 6, a three-component OIA photocathode was prepared using NiO, P1 dye, and MoS_x cluster-based catalyst, which showed promising performance towards photoelectrocatalytic H₂ production. The study discussed the importance of different optoelectronic properties of the organic dyes and the key role of the catalyst anchoring strategy and their effect on the final performance. For instance, P1-dye outperformed [Ru(bpy)₃]²⁺ in terms of charge separation/extraction from NiO due to the push-pull effect, which combined with the electrodeposition (as opposed to drop casting) approach of molecular MoS_x clusters showed the highest performance for stable H₂ production. However, the best performing architecture still could only achieve a faradaic efficiency of 43%, leaving room for further improvement. Literature reports on the use of thin amorphous film such as Al₂O₃ have shown to further improve the charge separation and avoid any back charge transfer. Such a film can be deposited using atomic layer deposition providing fine control over the thickness and the homogeneity of the film. Overall, these results strongly highlight the versatility and advantages of organic-inorganic hybrids, which can be further extended to both improving the photocathode performance and also be extended for the construction of photoanodes, thereby resulting efficient photoelectrocatalytic cells for solar driven water splitting, as shown in Scheme 7.4.



Scheme 7.4 left showing the photocathode prepared using NiO|P1-dye| electrodeposited MoS_x clusters for photoelectrocatalytic hydrogen production and right showing a improved photocathode (with additional Al₂O₃ layer) coupled with a similarly constructed photoanode for visible light driven overall water splitting

References

- (1) Boretti, A.; Rosa, L. Reassessing the Projections of the World Water Development Report. *Npj Clean Water* **2019**, *2* (1), 1–6. <https://doi.org/10.1038/s41545-019-0039-9>.
- (2) Wada, Y.; Flörke, M.; Hanasaki, N.; Eisner, S.; Fischer, G.; Tramberend, S.; Satoh, Y.; van Vliet, M. T. H.; Yillia, P.; Ringler, C.; Burek, P.; Wiberg, D. Modeling Global Water Use for the 21st Century: The Water Futures and Solutions (WFaS) Initiative and Its Approaches. *Geosci. Model Dev.* **2016**, *9* (1), 175–222. <https://doi.org/10.5194/gmd-9-175-2016>.
- (3) *Wastewater Pollution: Turning a Critical Problem into Opportunity*. The Nature Conservancy. <https://www.nature.org/en-us/what-we-do/our-priorities/protect-water-and-land/land-and-water-stories/wastewater-pollution/> (accessed 2024-06-04).
- (4) Hassan, J.; Rajib, M. M. R.; Sarker, U.; Akter, M.; Khan, M. N.-E.-A.; Khandaker, S.; Khalid, F.; Rahman, G. K. M. M.; Ercisli, S.; Muresan, C. C.; Marc, R. A. Optimizing Textile Dyeing Wastewater for Tomato Irrigation through Physiochemical, Plant Nutrient Uses and Pollution Load Index of Irrigated Soil. *Sci. Rep.* **2022**, *12* (1), 10088. <https://doi.org/10.1038/s41598-022-11558-1>.
- (5) Sarker, S. K. *Wastewater Recycling in Textile Industries*. Earth.Org. <https://earth.org/wastewater-recycling-in-textile-industries/> (accessed 2024-06-04).
- (6) Singh, R. P.; Singh, P. K.; Gupta, R.; Singh, R. L. Treatment and Recycling of Wastewater from Textile Industry. In *Advances in Biological Treatment of Industrial Waste Water and their Recycling for a Sustainable Future*; Singh, R. L., Singh, R. P., Eds.; Springer: Singapore, 2019; pp 225–266. https://doi.org/10.1007/978-981-13-1468-1_8.
- (7) Agarwala, R.; Mulky, L. Adsorption of Dyes from Wastewater: A Comprehensive Review. *ChemBioEng Rev.* **2023**, *10* (3), 326–335. <https://doi.org/10.1002/cben.202200011>.
- (8) Jiang, M.; Ye, K.; Deng, J.; Lin, J.; Ye, W.; Zhao, S.; Van der Bruggen, B. Conventional Ultrafiltration As Effective Strategy for Dye/Salt Fractionation in Textile Wastewater Treatment. *Environ. Sci. Technol.* **2018**, *52* (18), 10698–10708. <https://doi.org/10.1021/acs.est.8b02984>.
- (9) Oyarce, E.; Roa, K.; Boulett, A.; Sotelo, S.; Cantero-López, P.; Sánchez, J.; Rivas, B. L. Removal of Dyes by Polymer-Enhanced Ultrafiltration: An Overview. *Polymers* **2021**, *13* (19), 3450. <https://doi.org/10.3390/polym13193450>.
- (10) Bunani, S.; Yörükoğlu, E.; Yüksel, Ü.; Kabay, N.; Yüksel, M.; Sert, G. Application of Reverse Osmosis for Reuse of Secondary Treated Urban Wastewater in Agricultural Irrigation. *Desalination* **2015**, *364*, 68–74. <https://doi.org/10.1016/j.desal.2014.07.030>.
- (11) Abid, M. F.; Zablouk, M. A.; Abid-Alameer, A. M. Experimental Study of Dye Removal from Industrial Wastewater by Membrane Technologies of Reverse Osmosis and Nanofiltration. *Iran. J. Environ. Health Sci. Eng.* **2012**, *9* (1), 17. <https://doi.org/10.1186/1735-2746-9-17>.
- (12) *World Energy Outlook 2012*; Internationale Energieagentur, Ed.; World Energy Outlook; Paris, 2012.
- (13) *The Paris Agreement* | UNFCCC. <https://unfccc.int/process-and-meetings/the-paris-agreement> (accessed 2023-05-02).
- (14) *Renewables – Global Energy Review 2021 – Analysis*. IEA. <https://www.iea.org/reports/global-energy-review-2021/renewables> (accessed 2024-06-04).
- (15) *Renewables - Energy System*. IEA. <https://www.iea.org/energy-system/renewables> (accessed 2024-05-29).
- (16) *Steam reforming of hydrocarbons. A historical perspective - ScienceDirect*. <https://www.sciencedirect.com/science/article/pii/S0167299104800387?via%3Dihub> (accessed 2024-06-04).
- (17) Abubakar, A.; Almeida, C. F. M.; Gemignani, M. A Review of Solar Photovoltaic System Maintenance Strategies. In *2021 14th IEEE International Conference on Industry Applications (INDUSCON)*; 2021; pp 1400–1407. <https://doi.org/10.1109/INDUSCON51756.2021.9529669>.

- (18) Wang, L.; Yu, J. Chapter 1 - Principles of Photocatalysis. In *Interface Science and Technology*; Yu, J., Zhang, L., Wang, L., Zhu, B., Eds.; S-scheme Heterojunction Photocatalysts; Elsevier, 2023; Vol. 35, pp 1–52. <https://doi.org/10.1016/B978-0-443-18786-5.00002-0>.
- (19) Kanchana, T. S.; Sivakumar, T.; Venkateswari, P. Enhanced Photocatalytic Properties of ZnS/CdS/ZnCdS Catalysts under Visible Light Irradiation. *J. Mol. Struct.* **2022**, *1265*, 133375. <https://doi.org/10.1016/j.molstruc.2022.133375>.
- (20) Kannan, S.; Subiramaniyam, N. P.; Sathishkumar, M. Investigation on the Structural, Optical and Photocatalytic Degradation Properties of ZnS/Mn:ZnS Thin Films under Visible Light Irradiation. *Mater. Today Proc.* **2021**, *38*, 907–912. <https://doi.org/10.1016/j.matpr.2020.05.311>.
- (21) Basera, P.; Saini, S.; Arora, E.; Singh, A.; Kumar, M.; Bhattacharya, S. Stability of Non-Metal Dopants to Tune the Photo-Absorption of TiO₂ at Realistic Temperatures and Oxygen Partial Pressures: A Hybrid DFT Study. *Sci. Rep.* **2019**, *9* (1), 11427. <https://doi.org/10.1038/s41598-019-47710-7>.
- (22) Gharaei, S. K.; Abbasnejad, M.; Maezono, R. Bandgap Reduction of Photocatalytic TiO₂ Nanotube by Cu Doping. *Sci. Rep.* **2018**, *8* (1), 14192. <https://doi.org/10.1038/s41598-018-32130-w>.
- (23) Pareek, S.; Quamara, J. K. Dielectric and Optical Properties of Graphitic Carbon Nitride–Titanium Dioxide Nanocomposite with Enhanced Charge Separation. *J. Mater. Sci.* **2018**, *53* (1), 604–612. <https://doi.org/10.1007/s10853-017-1506-7>.
- (24) Goodman, E. D.; Zhou, C.; Cargnello, M. Design of Organic/Inorganic Hybrid Catalysts for Energy and Environmental Applications. *ACS Cent. Sci.* **2020**, *6* (11), 1916–1937. <https://doi.org/10.1021/acscentsci.0c01046>.
- (25) Judeinstein, P.; Sanchez, C. Hybrid Organic–Inorganic Materials: A Land of Multidisciplinarity. *J. Mater. Chem.* **1996**, *6* (4), 511–525. <https://doi.org/10.1039/JM9960600511>.
- (26) Ren, B.; Wang, T.; Qu, G.; Deng, F.; Liang, D.; Yang, W.; Liu, M. In Situ Synthesis of G-C₃N₄/TiO₂ Heterojunction Nanocomposites as a Highly Active Photocatalyst for the Degradation of Orange II under Visible Light Irradiation. *Environ. Sci. Pollut. Res.* **2018**, *25* (19), 19122–19133. <https://doi.org/10.1007/s11356-018-2114-z>.
- (27) Yan, S. C.; Lv, S. B.; Li, Z. S.; Zou, Z. G. Organic–Inorganic Composite Photocatalyst of g-C₃N₄ and TaON with Improved Visible Light Photocatalytic Activities. *Dalton Trans.* **2010**, *39* (6), 1488–1491. <https://doi.org/10.1039/B914110C>.
- (28) Shin, J.; Lee, J.; Xiao, X.; Yu, T. Enhancing Catalytic Activity of TiO₂ Nanoparticles through Acid Treatment in Eosin-Y Sensitized Photohydrogen Evolution Reaction System. *Heliyon* **2024**, *10* (9), e30765. <https://doi.org/10.1016/j.heliyon.2024.e30765>.
- (29) Abe, R.; Hara, K.; Sayama, K.; Domen, K.; Arakawa, H. Steady Hydrogen Evolution from Water on Eosin Y-Fixed TiO₂ Photocatalyst Using a Silane-Coupling Reagent under Visible Light Irradiation. *J. Photochem. Photobiol. Chem.* **2000**, *137* (1), 63–69. [https://doi.org/10.1016/S1010-6030\(00\)00351-8](https://doi.org/10.1016/S1010-6030(00)00351-8).
- (30) Zhang, G.; Lan, Z.-A.; Lin, L.; Lin, S.; Wang, X. Overall Water Splitting by Pt/g-C₃N₄ Photocatalysts without Using Sacrificial Agents. *Chem. Sci.* **2016**, *7* (5), 3062–3066. <https://doi.org/10.1039/C5SC04572J>.
- (31) Zhou, X.; Li, Y.; Xing, Y.; Li, J.; Jiang, X. Effects of the Preparation Method of Pt/g-C₃N₄ Photocatalysts on Their Efficiency for Visible-Light Hydrogen Production. *Dalton Trans.* **2019**, *48* (40), 15068–15073. <https://doi.org/10.1039/C9DT02938A>.
- (32) Nandan, S. P.; Gumerova, N. I.; Schubert, J. S.; Saito, H.; Rompel, A.; Cherevan, A.; Eder, D. Immobilization of a [CoIIIColl(H₂O)W₁₁O₃₉]⁷⁻ Polyoxoanion for the Photocatalytic Oxygen Evolution Reaction. *ACS Mater. Au* **2022**, *2* (4), 505–515. <https://doi.org/10.1021/acsmaterialsau.2c00025>.
- (33) Massin, J.; Bräutigam, M.; Bold, S.; Wächtler, M.; Pavone, M.; Muñoz-García, A. B.; Dietzek, B.; Artero, V.; Chavarot-Kerlidou, M. Investigating Light-Driven Hole Injection and Hydrogen Evolution Catalysis at Dye-Sensitized NiO Photocathodes: A Combined Experimental–Theoretical Study. *J. Phys. Chem. C* **2019**, *123* (28), 17176–17184. <https://doi.org/10.1021/acs.jpcc.9b04715>.

- (34) *Photoelectrochemical Hydrogen Production by a Cobalt Tetrapyrrolyl Catalyst Using Push–Pull Dye-Sensitized NiO Photocathodes - Bourguignon - 2023 - Advanced Energy and Sustainability Research - Wiley Online Library.*
<https://onlinelibrary.wiley.com/doi/full/10.1002/aesr.202300095> (accessed 2024-06-04).
- (35) Luna, A. L.; Dragoe, D.; Wang, K.; Beaunier, P.; Kowalska, E.; Ohtani, B.; Bahena Uribe, D.; Valenzuela, M. A.; Remita, H.; Colbeau-Justin, C. Photocatalytic Hydrogen Evolution Using Ni–Pd/TiO₂: Correlation of Light Absorption, Charge-Carrier Dynamics, and Quantum Efficiency. *J. Phys. Chem. C* **2017**, *121* (26), 14302–14311.
<https://doi.org/10.1021/acs.jpcc.7b01167>.
- (36) Al-Azri, Z. H. N.; Chen, W.-T.; Chan, A.; Jovic, V.; Ina, T.; Idriss, H.; Waterhouse, G. I. N. The Roles of Metal Co-Catalysts and Reaction Media in Photocatalytic Hydrogen Production: Performance Evaluation of M/TiO₂ Photocatalysts (M = Pd, Pt, Au) in Different Alcohol–Water Mixtures. *J. Catal.* **2015**, *329*, 355–367.
<https://doi.org/10.1016/j.jcat.2015.06.005>.
- (37) Haselmann, G. M.; Eder, D. Early-Stage Deactivation of Platinum-Loaded TiO₂ Using In Situ Photodeposition during Photocatalytic Hydrogen Evolution. *ACS Catal.* **2017**, *7* (7), 4668–4675. <https://doi.org/10.1021/acscatal.7b00845>.
- (38) Alvaro, M.; Carbonell, E.; Ferrer, B.; Llabrés i Xamena, F. X.; Garcia, H. Semiconductor Behavior of a Metal-Organic Framework (MOF). *Chem. – Eur. J.* **2007**, *13* (18), 5106–5112. <https://doi.org/10.1002/chem.200601003>.
- (39) Zhang, M.; Wang, L.; Zeng, T.; Shang, Q.; Zhou, H.; Pan, Z.; Cheng, Q. Two Pure MOF-Photocatalysts Readily Prepared for the Degradation of Methylene Blue Dye under Visible Light. *Dalton Trans.* **2018**, *47* (12), 4251–4258.
<https://doi.org/10.1039/C8DT00156A>.
- (40) Bhuyan, A.; Ahmaruzzaman, Md. Recent Advances in MOF-5-Based Photocatalysts for Efficient Degradation of Toxic Organic Dyes in Aqueous Medium. *Sustain.* **2024**, *3*, 100016. <https://doi.org/10.1016/j.nxsust.2023.100016>.
- (41) Yao, T.; Tan, Y.; Zhou, Y.; Chen, Y.; Xiang, M. Preparation of Core-Shell MOF-5/Bi₂WO₆ Composite for the Enhanced Photocatalytic Degradation of Pollutants. *J. Solid State Chem.* **2022**, *308*, 122882. <https://doi.org/10.1016/j.jssc.2022.122882>.
- (42) Veselska, O.; Demessence, A. D10 Coinage Metal Organic Chalcogenolates: From Oligomers to Coordination Polymers. *Coord. Chem. Rev.* **2018**, *355*, 240–270.
<https://doi.org/10.1016/j.ccr.2017.08.014>.
- (43) Che, C.-M.; Li, C.-H.; Chui, S. S.-Y.; Roy, V. a. L.; Low, K.-H. Homoleptic Copper(I) Arylthiolates as a New Class of p-Type Charge Carriers: Structures and Charge Mobility Studies. *Chem. – Eur. J.* **2008**, *14* (10), 2965–2975.
<https://doi.org/10.1002/chem.200700723>.
- (44) Rabl, H.; Myakala, S. N.; Rath, J.; Fickl, B.; Schubert, J. S.; Apaydin, D. H.; Eder, D. Microwave-Assisted Synthesis of Metal-Organic Chalcogenolate Assemblies as Electrocatalysts for Syngas Production. *Commun. Chem.* **2023**, *6* (1), 1–8.
<https://doi.org/10.1038/s42004-023-00843-3>.
- (45) Fujishima, A.; Honda, K. Electrochemical Photolysis of Water at a Semiconductor Electrode. *Nature* **1972**, *238* (5358), 37–38. <https://doi.org/10.1038/238037a0>.
- (46) Mayyahi, A. A.; M. Everhart, B.; B. Shrestha, T.; C. Back, T.; B. Amama, P. Enhanced Charge Separation in TiO₂/Nanocarbon Hybrid Photocatalysts through Coupling with Short Carbon Nanotubes. *RSC Adv.* **2021**, *11* (19), 11702–11713.
<https://doi.org/10.1039/D1RA00045D>.
- (47) Wang, W.; Xu, D.; Cheng, B.; Yu, J.; Jiang, C. Hybrid carbon@TiO₂ Hollow Spheres with Enhanced Photocatalytic CO₂ Reduction Activity. *J. Mater. Chem. A* **2017**, *5* (10), 5020–5029. <https://doi.org/10.1039/C6TA11121A>.
- (48) Lee, T.; Bui, H. T.; Yoo, J.; Ra, M.; Han, S. H.; Kim, W.; Kwon, W. Formation of TiO₂@Carbon Core/Shell Nanocomposites from a Single Molecular Layer of Aromatic Compounds for Photocatalytic Hydrogen Peroxide Generation. *ACS Appl. Mater. Interfaces* **2019**, *11* (44), 41196–41203. <https://doi.org/10.1021/acsami.9b10015>.
- (49) Li, Y.; Zhang, H.; Hu, X.; Zhao, X.; Han, M. Efficient Visible-Light-Induced Photocatalytic Activity of a 3D-Ordered Titania Hybrid Photocatalyst with a Core/Shell

- Structure of Dye-Containing Polymer/Titania. *J. Phys. Chem. C* **2008**, *112* (38), 14973–14979. <https://doi.org/10.1021/jp8055152>.
- (50) Moustakas, N. G.; Kontos, A. G.; Likodimos, V.; Katsaros, F.; Boukos, N.; Tsoutsou, D.; Dimoulas, A.; Romanos, G. E.; Dionysiou, D. D.; Falaras, P. Inorganic–Organic Core–Shell Titania Nanoparticles for Efficient Visible Light Activated Photocatalysis. *Appl. Catal. B Environ.* **2013**, *130–131*, 14–24. <https://doi.org/10.1016/j.apcatb.2012.10.007>.
- (51) Tu, W.; Zhou, Y.; Liu, Q.; Yan, S.; Bao, S.; Wang, X.; Xiao, M.; Zou, Z. An In Situ Simultaneous Reduction-Hydrolysis Technique for Fabrication of TiO₂-Graphene 2D Sandwich-Like Hybrid Nanosheets: Graphene-Promoted Selectivity of Photocatalytic-Driven Hydrogenation and Coupling of CO₂ into Methane and Ethane. *Adv. Funct. Mater.* **2013**, *23* (14), 1743–1749. <https://doi.org/10.1002/adfm.201202349>.
- (52) Xu, Y.; Schoonen, M. A. A. The Absolute Energy Positions of Conduction and Valence Bands of Selected Semiconducting Minerals. *Am. Mineral.* **2000**, *85* (3–4), 543–556. <https://doi.org/10.2138/am-2000-0416>.
- (53) Czerw, R.; Foley, B.; Tekleab, D.; Rubio, A.; Ajayan, P. M.; Carroll, D. L. Substrate-Interface Interactions between Carbon Nanotubes and the Supporting Substrate. *Phys. Rev. B* **2002**, *66* (3), 033408. <https://doi.org/10.1103/PhysRevB.66.033408>.
- (54) Trenczek-Zajac, A.; Kusior, A.; Mazurków, J.; Michalec, K.; Synowiec, M.; Radecka, M. Chapter Eleven - Interface Design, Surface-Related Properties, and Their Role in Interfacial Electron Transfer. Part II: Photochemistry-Related Topics. In *Advances in Inorganic Chemistry*; van Eldik, R., Hubbard, C. D., Eds.; Recent Highlights II; Academic Press, 2022; Vol. 79, pp 415–447. <https://doi.org/10.1016/bs.adioch.2021.12.010>.
- (55) *Wiley-VCH - Modern Spectroscopy*. <https://www.wiley-vch.de/de/fachgebiete/naturwissenschaften/modern-spectroscopy-978-0-470-84416-8> (accessed 2024-08-03).
- (56) Beyssac, O.; Lazzeri, M. Application of Raman Spectroscopy to the Study of Graphitic Carbons in the Earth Sciences. In *Raman spectroscopy applied to Earth sciences and cultural heritage*; Dubessy, J., Caumon, M.-C., Rull, F., Eds.; European Mineralogical Union, 2012; Vol. 12, p 0. <https://doi.org/10.1180/EMU-notes.12.12>.
- (57) Vibrational Raman Scattering. In *The Raman Effect*; John Wiley & Sons, Ltd, 2002; pp 85–152. <https://doi.org/10.1002/0470845767.ch5>.
- (58) Serre, C.; Férey, G. Hybrid Open Frameworks. 8. Hydrothermal Synthesis, Crystal Structure, and Thermal Behavior of the First Three-Dimensional Titanium(IV) Diphosphonate with an Open Structure: Ti₃O₂(H₂O)₂(O₃P–(CH₂)–PO₃)₂·(H₂O)₂, or MIL-22. *Inorg. Chem.* **1999**, *38* (23), 5370–5373. <https://doi.org/10.1021/ic990345m>.
- (59) Dan-Hardi, M.; Serre, C.; Frot, T.; Rozes, L.; Maurin, G.; Sanchez, C.; Férey, G. A New Photoactive Crystalline Highly Porous Titanium(IV) Dicarboxylate. *J. Am. Chem. Soc.* **2009**, *131* (31), 10857–10859. <https://doi.org/10.1021/ja903726m>.
- (60) Fang, W.-H.; Zhang, L.; Zhang, J. Synthetic Strategies, Diverse Structures and Tuneable Properties of Polyoxo-Titanium Clusters. *Chem. Soc. Rev.* **2018**, *47* (2), 404–421. <https://doi.org/10.1039/C7CS00511C>.
- (61) Pearson, R. G. Hard and Soft Acids and Bases, HSAB, Part 1: Fundamental Principles. *J. Chem. Educ.* **1968**, *45* (9), 581. <https://doi.org/10.1021/ed045p581>.
- (62) Yuan, S.; Feng, L.; Wang, K.; Pang, J.; Bosch, M.; Lollar, C.; Sun, Y.; Qin, J.; Yang, X.; Zhang, P.; Wang, Q.; Zou, L.; Zhang, Y.; Zhang, L.; Fang, Y.; Li, J.; Zhou, H.-C. Stable Metal–Organic Frameworks: Design, Synthesis, and Applications. *Adv. Mater.* **2018**, *30* (37), 1704303. <https://doi.org/10.1002/adma.201704303>.
- (63) Yuan, S.; Qin, J.-S.; Lollar, C. T.; Zhou, H.-C. Stable Metal–Organic Frameworks with Group 4 Metals: Current Status and Trends. *ACS Cent. Sci.* **2018**, *4* (4), 440–450. <https://doi.org/10.1021/acscentsci.8b00073>.
- (64) Kavun, V.; Uslamin, E.; van der Linden, B.; Canossa, S.; Goryachev, A.; Bos, E. E.; Garcia Santaclara, J.; Smolentsev, G.; Repo, E.; van der Veen, M. A. Promoting Photocatalytic Activity of NH₂-MIL-125(Ti) for H₂ Evolution Reaction through Creation of TiIII- and CoI-Based Proton Reduction Sites. *ACS Appl. Mater. Interfaces* **2023**, *15* (47), 54590–54601. <https://doi.org/10.1021/acsami.3c15490>.

- (65) Pukdeejorhor, L.; Wannapaiboon, S.; Berger, J.; Rodewald, K.; Thongratkaew, S.; Impeng, S.; Warnan, J.; Bureekaew, S.; Fischer, R. A. Defect Engineering in MIL-125-(Ti)-NH₂ for Enhanced Photocatalytic H₂ Generation. *J. Mater. Chem. A* **2023**, *11* (16), 9143–9151. <https://doi.org/10.1039/D2TA09963B>.
- (66) He, Y.; Lv, T.; Xiao, B.; Liu, B.; Zhou, T.; Zhang, J.; Zhang, Y.; Zhang, G.; Liu, Q. Research Progress of MIL-125 and Its Modifications in Photocatalytic Hydrogen Evolution. *J. Mater. Chem. C* **2023**, *11* (21), 6800–6818. <https://doi.org/10.1039/D3TC00757J>.
- (67) Qing, Y.; Gao, W.; Long, Y.; Kang, Y.; Xu, C. Functionalized Titanium-Based MOF for Cr(VI) Removal from Wastewater. *Inorg. Chem.* **2023**, *62* (18), 6909–6919. <https://doi.org/10.1021/acs.inorgchem.2c04501>.
- (68) Xie, L.; Yang, H.; Wu, X.; Wang, L.; Zhu, B.; Tang, Y.; Bai, M.; Li, L.; Cheng, C.; Ma, T. Ti-MOF-Based Biosafety Materials for Efficient and Long-Life Disinfection via Synergistic Photodynamic and Photothermal Effects. *Biosaf. Health* **2022**, *04* (02), 135–146. <https://doi.org/10.1016/j.bshealth.2022.02.001>.
- (69) Li, J.; Lin, G.; Zhong, Z.; Wang, Z.; Wang, S.; Fu, L.; Hu, T. A Novel Magnetic Ti-MOF/Chitosan Composite for Efficient Adsorption of Pb(II) from Aqueous Solutions: Synthesis and Investigation. *Int. J. Biol. Macromol.* **2024**, *258*, 129170. <https://doi.org/10.1016/j.ijbiomac.2023.129170>.
- (70) Abdelhameed, R. M.; El-Shahat, M.; Abd El-Ghaffar, M. A. Boosting the Photocatalytic Activity of Ti-MOF via Emerging with Metal Phthalocyanine to Degrade Hazard Textile Pigments. *J. Alloys Compd.* **2022**, *896*, 162992. <https://doi.org/10.1016/j.jallcom.2021.162992>.
- (71) Yao, P.; Liu, Y.; Tang, X.; Lu, S.; Li, Z.; Yao, Y. Synthesis of Reusable NH₂-MIL-125(Ti)@polymer Monolith as Efficient Adsorbents for Dyes Wastewater Remediation. *Green Chem. Eng.* **2023**, *4* (4), 439–447. <https://doi.org/10.1016/j.gce.2022.06.004>.
- (72) Hendon, C. H.; Tiana, D.; Walsh, A. Conductive Metal–Organic Frameworks and Networks: Fact or Fantasy? *Phys. Chem. Chem. Phys.* **2012**, *14* (38), 13120–13132. <https://doi.org/10.1039/C2CP41099K>.
- (73) Sun, L.; Campbell, M. G.; Dincă, M. Electrically Conductive Porous Metal–Organic Frameworks. *Angew. Chem. Int. Ed.* **2016**, *55* (11), 3566–3579. <https://doi.org/10.1002/anie.201506219>.
- (74) Castner, A. T.; Su, H.; Svensson Grape, E.; Inge, A. K.; Johnson, B. A.; Ahlquist, M. S. G.; Ott, S. Microscopic Insights into Cation-Coupled Electron Hopping Transport in a Metal–Organic Framework. *J. Am. Chem. Soc.* **2022**, *144* (13), 5910–5920. <https://doi.org/10.1021/jacs.1c13377>.
- (75) Calvo, J. J.; Angel, S. M.; So, M. C. Charge Transport in Metal–Organic Frameworks for Electronics Applications. *APL Mater.* **2020**, *8* (5), 050901. <https://doi.org/10.1063/1.5143590>.
- (76) Wang, S.; Kitao, T.; Guillou, N.; Wahiduzzaman, M.; Martineau-Corcoc, C.; Nouar, F.; Tissot, A.; Binet, L.; Ramsahye, N.; Devautour-Vinot, S.; Kitagawa, S.; Seki, S.; Tsutsui, Y.; Briois, V.; Steunou, N.; Maurin, G.; Uemura, T.; Serre, C. A Phase Transformable Ultrastable Titanium-Carboxylate Framework for Photoconduction. *Nat. Commun.* **2018**, *9* (1), 1660. <https://doi.org/10.1038/s41467-018-04034-w>.
- (77) Li, C.; Xu, H.; Gao, J.; Du, W.; Shangguan, L.; Zhang, X.; Lin, R.-B.; Wu, H.; Zhou, W.; Liu, X.; Yao, J.; Chen, B. Tunable Titanium Metal–Organic Frameworks with Infinite 1D Ti–O Rods for Efficient Visible-Light-Driven Photocatalytic H₂ Evolution. *J. Mater. Chem. A* **2019**, *7* (19), 11928–11933. <https://doi.org/10.1039/C9TA01942A>.
- (78) Cadiou, A.; Kolobov, N.; Srinivasan, S.; Goesten, M. G.; Haspel, H.; Bavykina, A. V.; Tchalala, M. R.; Maity, P.; Goryachev, A.; Poryvaev, A. S.; Eddaoudi, M.; Fedin, M. V.; Mohammed, O. F.; Gascon, J. A Titanium Metal–Organic Framework with Visible-Light-Responsive Photocatalytic Activity. *Angew. Chem. Int. Ed.* **2020**, *59* (32), 13468–13472. <https://doi.org/10.1002/anie.202000158>.
- (79) Wang, S.; Cabrero-Antonino, M.; Navalón, S.; Cao, C.; Tissot, A.; Dovgaliuk, I.; Marrot, J.; Martineau-Corcoc, C.; Yu, L.; Wang, H.; Shepard, W.; García, H.; Serre, C. A Robust Titanium Isophthalate Metal–Organic Framework for Visible-Light Photocatalytic

CO₂ Methanation. *Chem* **2020**, *6* (12), 3409–3427.
<https://doi.org/10.1016/j.chempr.2020.10.017>.

- (80) Salcedo-Abraira, P.; Babaryk, A. A.; Montero-Lanzuela, E.; Contreras-Almengor, O. R.; Cabrero-Antonino, M.; Grape, E. S.; Willhammar, T.; Navalón, S.; Elkäim, E.; García, H.; Horcajada, P. A Novel Porous Ti-Squarate as Efficient Photocatalyst in the Overall Water Splitting Reaction under Simulated Sunlight Irradiation. *Adv. Mater.* **2021**, *33* (52), 2106627. <https://doi.org/10.1002/adma.202106627>.
- (81) Smolders, S.; Willhammar, T.; Krajnc, A.; Sentosun, K.; Wharmby, M. T.; Lomachenko, K. A.; Bals, S.; Mali, G.; Roeyffers, M. B. J.; De Vos, D. E.; Bueken, B. A Titanium(IV)-Based Metal–Organic Framework Featuring Defect-Rich Ti-O Sheets as an Oxidative Desulfurization Catalyst. *Angew. Chem.* **2019**, *131* (27), 9258–9263.
<https://doi.org/10.1002/ange.201904347>.
- (82) Ayala, P.; Naghdi, S.; Nandan, S. P.; Myakala, S. N.; Rath, J.; Saito, H.; Guggenberger, P.; Lakhlanlal, L.; Kleitz, F.; Toroker, M. C.; Cherevan, A.; Eder, D. The Emergence of 2D Building Units in Metal-Organic Frameworks for Photocatalytic Hydrogen Evolution: A Case Study with COK-47. *Adv. Energy Mater.* *n/a* (n/a), 2300961.
<https://doi.org/10.1002/aenm.202300961>.
- (83) Wi, D. H.; Park, S. Y.; Lee, S.; Sung, J.; Hong, J. W.; Han, S. W. Metal–Semiconductor Ternary Hybrids for Efficient Visible-Light Photocatalytic Hydrogen Evolution. *J. Mater. Chem. A* **2018**, *6* (27), 13225–13235.
<https://doi.org/10.1039/C8TA03462A>.
- (84) Arias, M.; López, E.; Nuñez, A.; Rubinos, D.; Soto, B.; Barral, M. T.; Díaz-Fierros, F. Adsorption of Methylene Blue by Red Mud, An Oxide- Rich Byproduct of Bauxite Refining. In *Effect of Mineral-Organic-Microorganism Interactions on Soil and Freshwater Environments*; Berthelin, J., Huang, P. M., Bollag, J.-M., Andreux, F., Eds.; Springer US: Boston, MA, 1999; pp 361–365. https://doi.org/10.1007/978-1-4615-4683-2_39.
- (85) Ali, A.; Muslim, M.; Neogi, I.; Afzal, M.; Alarifi, A.; Ahmad, M. Construction of a 3D Metal–Organic Framework and Its Composite for Water Remediation via Selective Adsorption and Photocatalytic Degradation of Hazardous Dye. *ACS Omega* **2022**, *7* (28), 24438–24451. <https://doi.org/10.1021/acsomega.2c01869>.
- (86) Chiu, Y.-H.; Chang, T.-F. M.; Chen, C.-Y.; Sone, M.; Hsu, Y.-J. Mechanistic Insights into Photodegradation of Organic Dyes Using Heterostructure Photocatalysts. *Catalysts* **2019**, *9* (5), 430. <https://doi.org/10.3390/catal9050430>.
- (87) Dean, J. C.; Oblinsky, D. G.; Rather, S. R.; Scholes, G. D. Methylene Blue Exciton States Steer Nonradiative Relaxation: Ultrafast Spectroscopy of Methylene Blue Dimer. *J. Phys. Chem. B* **2016**, *120* (3), 440–454. <https://doi.org/10.1021/acs.jpcc.5b11847>.
- (88) Michaelis, L.; Granick, S. Metachromasy of Basic Dyestuffs. *J. Am. Chem. Soc.* **1945**, *67* (7), 1212–1219. <https://doi.org/10.1021/ja01223a055>.
- (89) Shil, A.; Saha, M.; Debnath, C.; Hussain, S. A.; Bhattacharjee, D. Matrix Dependent Changes in Metachromasy of Crystal Violet in Langmuir-Blodgett Films. *Chem. Phys. Lett.* **2016**, *665*, 76–84. <https://doi.org/10.1016/j.cplett.2016.10.027>.
- (90) Salvesson, P. J.; Haerianardakani, S.; Thuy-Boun, A.; Yoo, S.; Kreutzer, A. G.; Demeler, B.; Nowick, J. S. Repurposing Triphenylmethane Dyes to Bind to Trimers Derived from Aβ. *J. Am. Chem. Soc.* **2018**, *140* (37), 11745–11754.
<https://doi.org/10.1021/jacs.8b06568>.
- (91) Shanmugaratnam, S.; Selvaratnam, B.; Baride, A.; Koodali, R.; Ravirajan, P.; Velauthapillai, D.; Shivatharsiny, Y. SnS₂/TiO₂ Nanocomposites for Hydrogen Production and Photodegradation under Extended Solar Irradiation. *Catalysts* **2021**, *11* (5), 589.
<https://doi.org/10.3390/catal11050589>.
- (92) Matsunami, D.; Yamanaka, K.; Mizoguchi, T.; Kojima, K. Comparison of Photodegradation of Methylene Blue Using Various TiO₂ Films and WO₃ Powders under Ultraviolet and Visible-Light Irradiation. *J. Photochem. Photobiol. Chem.* **2019**, *369*, 106–114. <https://doi.org/10.1016/j.jphotochem.2018.10.020>.
- (93) Wolski, L.; Walkowiak, A.; Ziolk, M. Formation of Reactive Oxygen Species upon Interaction of Au/ZnO with H₂O₂ and Their Activity in Methylene Blue Degradation. *Catal. Today* **2019**, *333*, 54–62. <https://doi.org/10.1016/j.cattod.2018.04.004>.

- (94) Wolski, L.; Ziolek, M. Insight into Pathways of Methylene Blue Degradation with H₂O₂ over Mono and Bimetallic Nb, Zn Oxides. *Appl. Catal. B Environ.* **2018**, *224*, 634–647. <https://doi.org/10.1016/j.apcatb.2017.11.008>.
- (95) *Photochemical reactions between 1,4-benzoquinone and O₂^{•-}* | *Environmental Science and Pollution Research*. <https://link.springer.com/article/10.1007/s11356-020-09422-8> (accessed 2024-02-16).
- (96) Huang, W.; Brigante, M.; Wu, F.; Mousty, C.; Hanna, K.; Mailhot, G. Assessment of the Fe(III)–EDDS Complex in Fenton-Like Processes: From the Radical Formation to the Degradation of Bisphenol A. *Environ. Sci. Technol.* **2013**, *47* (4), 1952–1959. <https://doi.org/10.1021/es304502y>.
- (97) Xu, H.-Y.; Li, B.; Shi, T.-N.; Wang, Y.; Komarneni, S. Nanoparticles of Magnetite Anchored onto Few-Layer Graphene: A Highly Efficient Fenton-like Nanocomposite Catalyst. *J. Colloid Interface Sci.* **2018**, *532*, 161–170. <https://doi.org/10.1016/j.jcis.2018.07.128>.
- (98) Seliverstov, A. F.; Ershov, B. G.; Lagunova, Yu. O.; Morozov, P. A.; Kamrukov, A. S.; Shashkovskii, S. G. Oxidative Degradation of EDTA in Aqueous Solutions under UV Irradiation. *Radiochemistry* **2008**, *50* (1), 70–74. <https://doi.org/10.1134/S1066362208010116>.
- (99) Wang, L.; Lan, X.; Peng, W.; Wang, Z. Uncertainty and Misinterpretation over Identification, Quantification and Transformation of Reactive Species Generated in Catalytic Oxidation Processes: A Review. *J. Hazard. Mater.* **2021**, *408*, 124436. <https://doi.org/10.1016/j.jhazmat.2020.124436>.
- (100) Naghdi, S.; Cherevan, A.; Giesriegl, A.; Guillet-Nicolas, R.; Biswas, S.; Gupta, T.; Wang, J.; Haunold, T.; Bayer, B. C.; Ruppachter, G.; Toroker, M. C.; Kleitz, F.; Eder, D. Selective Ligand Removal to Improve Accessibility of Active Sites in Hierarchical MOFs for Heterogeneous Photocatalysis. *Nat. Commun.* **2022**, *13* (1), 282. <https://doi.org/10.1038/s41467-021-27775-7>.
- (101) Zhang, R.; Ma, Y.; Lan, W.; Sameen, D. E.; Ahmed, S.; Dai, J.; Qin, W.; Li, S.; Liu, Y. Enhanced Photocatalytic Degradation of Organic Dyes by Ultrasonic-Assisted Electro spray TiO₂/Graphene Oxide on Polyacrylonitrile/β-Cyclodextrin Nanofibrous Membranes. *Ultrason. Sonochem.* **2021**, *70*, 105343. <https://doi.org/10.1016/j.ultsonch.2020.105343>.
- (102) Wedler, G.; Freund, H.-J. *Lehr- und Arbeitsbuch physikalische Chemie, Siebte, wesentlich überarbeitete und erweiterte Auflage.*; Wiley-VCH Verlag GmbH & Co. KGaA: Weinheim, Germany, 2018.
- (103) Hussain, S.; Chae, J.; Akbar, K.; Vikraman, D.; Truong, L.; Naqvi, B. A.; Abbas, Y.; Kim, H.-S.; Chun, S.-H.; Kim, G.; Jung, J. Fabrication of Robust Hydrogen Evolution Reaction Electrocatalyst Using Ag₂Se by Vacuum Evaporation. *Nanomaterials* **2019**, *9* (10), 1460. <https://doi.org/10.3390/nano9101460>.
- (104) Xie, Z.; Liu, Q.; Zhao, H.; Chen, H.; Jia, G.; Lei, E.; Wang, C.; Zhou, Y. Efficient Hydrogen Evolution from G-C₃N₄ under Visible Light by in Situ Loading Ag₂Se Nanoparticles as Co-Catalysts. *Catal. Commun.* **2024**, *186*, 106837. <https://doi.org/10.1016/j.catcom.2023.106837>.
- (105) *ZnO/TiO₂/Ag₂Se nanostructures as photoelectrocatalysts for the degradation of oxytetracycline in water - ScienceDirect*. <https://www.sciencedirect.com/science/article/pii/S0013468619320651?via%3Dihub> (accessed 2024-05-23).
- (106) Wood, A.; Giersig, M.; Mulvaney, P. Fermi Level Equilibration in Quantum Dot–Metal Nanojunctions. *J. Phys. Chem. B* **2001**, *105* (37), 8810–8815. <https://doi.org/10.1021/jp011576t>.
- (107) Walter, M. G.; Warren, E. L.; McKone, J. R.; Boettcher, S. W.; Mi, Q.; Santori, E. A.; Lewis, N. S. Correction to Solar Water Splitting Cells. *Chem. Rev.* **2011**, *111* (9), 5815–5815. <https://doi.org/10.1021/cr200102n>.
- (108) Choi, Y.; Kim, H.; Moon, G.; Jo, S.; Choi, W. Boosting up the Low Catalytic Activity of Silver for H₂ Production on Ag/TiO₂ Photocatalyst: Thiocyanate as a Selective Modifier. *ACS Catal.* **2016**, *6* (2), 821–828. <https://doi.org/10.1021/acscatal.5b02376>.

- (109) Cuthbert, H. L.; Wallbank, A. I.; Taylor, N. J.; Corrigan, J. F. Synthesis and Structural Characterization of $[\text{Cu}_{20}\text{Se}_4(\text{M}_3\text{-SePh})_{12}(\text{PPh}_3)_6]$ and $[\text{Ag}(\text{SePh})]^\infty$. *Z. Für Anorg. Allg. Chem.* **2002**, *628* (11), 2483–2488. [https://doi.org/10.1002/1521-3749\(200211\)628:11<2483::AID-ZAAC2483>3.0.CO;2-U](https://doi.org/10.1002/1521-3749(200211)628:11<2483::AID-ZAAC2483>3.0.CO;2-U).
- (110) Trang, B.; Yeung, M.; Popple, D. C.; Schriber, E. A.; Brady, M. A.; Kuykendall, T. R.; Hohman, J. N. Tarnishing Silver Metal into Mithrene. *J. Am. Chem. Soc.* **2018**, *140* (42), 13892–13903. <https://doi.org/10.1021/jacs.8b08878>.
- (111) Schriber, E. A.; Popple, D. C.; Yeung, M.; Brady, M. A.; Corlett, S. A.; Hohman, J. N. Mithrene Is a Self-Assembling Robustly Blue Luminescent Metal–Organic Chalcogenolate Assembly for 2D Optoelectronic Applications. *ACS Appl. Nano Mater.* **2018**, *1* (7), 3498–3508. <https://doi.org/10.1021/acsanm.8b00662>.
- (112) Li, S.; Zang, W.; Liu, X.; Pennycook, S. J.; Kou, Z.; Yang, C.; Guan, C.; Wang, J. Heterojunction Engineering of $\text{MoSe}_2/\text{MoS}_2$ with Electronic Modulation towards Synergetic Hydrogen Evolution Reaction and Supercapacitance Performance. *Chem. Eng. J.* **2019**, *359*, 1419–1426. <https://doi.org/10.1016/j.cej.2018.11.036>.
- (113) Schriber, E. A.; Paley, D. W.; Bolotovskiy, R.; Rosenberg, D. J.; Sierra, R. G.; Aquila, A.; Mendez, D.; Poitevin, F.; Blaschke, J. P.; Bhowmick, A.; Kelly, R. P.; Hunter, M.; Hayes, B.; Popple, D. C.; Yeung, M.; Pareja-Rivera, C.; Lisova, S.; Tono, K.; Sugahara, M.; Owada, S.; Kuykendall, T.; Yao, K.; Schuck, P. J.; Solis-Ibarra, D.; Sauter, N. K.; Brewster, A. S.; Hohman, J. N. Chemical Crystallography by Serial Femtosecond X-Ray Diffraction. *Nature* **2022**, *601* (7893), 360–365. <https://doi.org/10.1038/s41586-021-04218-3>.
- (114) Maserati, L.; Prato, M.; Pecorario, S.; Passarella, B.; Perinot, A.; Thomas, A. A.; Melloni, F.; Natali, D.; Caironi, M. Photo-Electrical Properties of 2D Quantum Confined Metal–Organic Chalcogenide Nanocrystal Films. *Nanoscale* **2021**, *13* (1), 233–241. <https://doi.org/10.1039/D0NR07409H>.
- (115) *Understanding the Synthetic Pathway to Large-Area, High-Quality $[\text{AgSePh}]^\infty$ Nanocrystal Films | The Journal of Physical Chemistry C.* <https://pubs.acs.org/doi/10.1021/acs.jpcc.0c07330> (accessed 2023-11-19).
- (116) Lee, W. S.; Cho, Y.; Powers, E. R.; Paritmongkol, W.; Sakurada, T.; Kulik, H. J.; Tisdale, W. A. Light Emission in 2D Silver Phenylchalcogenolates. *ACS Nano* **2022**, *16* (12), 20318–20328. <https://doi.org/10.1021/acsnano.2c06204>.
- (117) Villani, E.; Sakanoue, K.; Einaga, Y.; Inagi, S.; Fiorani, A. Photophysics and Electrochemistry of Ruthenium Complexes for Electrogenenerated Chemiluminescence. *J. Electroanal. Chem.* **2022**, *921*, 116677. <https://doi.org/10.1016/j.jelechem.2022.116677>.
- (118) Pellegrin, Y.; Odobel, F. Sacrificial Electron Donor Reagents for Solar Fuel Production. *Comptes Rendus Chim.* **2017**, *20* (3), 283–295. <https://doi.org/10.1016/j.crci.2015.11.026>.
- (119) Chemistry of Ascorbic Acid. *Wikipedia*; 2024.
- (120) Popple, D. C.; Schriber, E. A.; Yeung, M.; Hohman, J. N. Competing Roles of Crystallization and Degradation of a Metal–Organic Chalcogenolate Assembly under Biphasic Solvothermal Conditions. *Langmuir* **2018**, *34* (47), 14265–14273. <https://doi.org/10.1021/acs.langmuir.8b03282>.
- (121) Tanuhadi, E.; Cano, J.; Batool, S.; Cherevan, A.; Eder, D.; Rompel, A. Ni₁₂ Tetracubane Cores with Slow Relaxation of Magnetization and Efficient Charge Utilization for Photocatalytic Hydrogen Evolution. *J. Mater. Chem. C* **2022**, *10* (45), 17048–17052. <https://doi.org/10.1039/D2TC03508A>.
- (122) Gaarenstroom, S. W.; Winograd, N. Initial and Final State Effects in the ESCA Spectra of Cadmium and Silver Oxides. *J. Chem. Phys.* **2008**, *67* (8), 3500–3506. <https://doi.org/10.1063/1.435347>.
- (123) Ferraria, A. M.; Carapeto, A. P.; Botelho do Rego, A. M. X-Ray Photoelectron Spectroscopy: Silver Salts Revisited. *Vacuum* **2012**, *86* (12), 1988–1991. <https://doi.org/10.1016/j.vacuum.2012.05.031>.
- (124) Kuang-liang, X. U.; Jing, L. I. U.; Zhao-xiong, Y. a. N.; Mei, J. I. N.; Zhi-hua, X. U. Synthesis and Use of Hollow Carbon Spheres for Electric Double-Layer Capacitors. *New Carbon Mater* **2021**, *36* (4), 794–809. [https://doi.org/10.1016/S1872-5805\(20\)60517-0](https://doi.org/10.1016/S1872-5805(20)60517-0).

- (125) Li, S.; Pasc, A.; Fierro, V.; Celzard, A. Hollow Carbon Spheres, Synthesis and Applications – a Review. *J. Mater. Chem. A* **2016**, *4* (33), 12686–12713. <https://doi.org/10.1039/C6TA03802F>.
- (126) Anderson, A.-L.; Binions, R. A Preferential Precursor for Photocatalytically Active Titanium Dioxide Thin Films: Titanium Bis-Ammonium Lactato Dihydroxide as an Alternative to Titanium Tetra Iso-Propoxide. *Polyhedron* **2016**, *118*, 81–90. <https://doi.org/10.1016/j.poly.2016.07.020>.
- (127) Zhai, Z.; Wang, S.; Xu, Y.; Zhang, L.; Yan, M.; Liu, Z. Carbon Aerogels with Modified Pore Structures as Electrode Materials for Supercapacitors. *J. Solid State Electrochem.* **2017**, *21* (12), 3545–3555. <https://doi.org/10.1007/s10008-017-3699-8>.
- (128) Frank, O.; Zukulova, M.; Laskova, B.; Kürti, J.; Koltai, J.; Kavan, L. Raman Spectra of Titanium Dioxide (Anatase, Rutile) with Identified Oxygen Isotopes (16, 17, 18). *Phys. Chem. Chem. Phys.* **2012**, *14* (42), 14567–14572. <https://doi.org/10.1039/C2CP42763J>.
- (129) Schubert, J. S.; Popovic, J.; Haselmann, G. M.; Nandan, S. P.; Wang, J.; Giesriegl, A.; Cherevan, A. S.; Eder, D. Immobilization of Co, Mn, Ni and Fe Oxide Co-Catalysts on TiO₂ for Photocatalytic Water Splitting Reactions. *J. Mater. Chem. A* **2019**, *7* (31), 18568–18579.
- (130) Yang, C.; Zhang, X.; Qin, J.; Shen, X.; Yu, R.; Ma, M.; Liu, R. Porous Carbon-Doped TiO₂ on TiC Nanostructures for Enhanced Photocatalytic Hydrogen Production under Visible Light. *J. Catal.* **2017**, *347*, 36–44. <https://doi.org/10.1016/j.jcat.2016.11.041>.
- (131) Du, X.; He, J. Facile Size-Controllable Syntheses of Highly Monodisperse Polystyrene Nano- and Microspheres by Polyvinylpyrrolidone-Mediated Emulsifier-Free Emulsion Polymerization. *J. Appl. Polym. Sci.* **2008**, *108* (3), 1755–1760. <https://doi.org/10.1002/app.27774>.
- (132) Treadway, J. A.; Moss, J. A.; Meyer, T. J. Visible Region Photooxidation on TiO₂ with a Chromophore–Catalyst Molecular Assembly. *Inorg. Chem.* **1999**, *38* (20), 4386–4387. <https://doi.org/10.1021/ic990466m>.
- (133) He, J.; Lindström, H.; Hagfeldt, A.; Lindquist, S.-E. Dye-Sensitized Nanostructured p-Type Nickel Oxide Film as a Photocathode for a Solar Cell. *J. Phys. Chem. B* **1999**, *103* (42), 8940–8943. <https://doi.org/10.1021/jp991681r>.
- (134) Li, L.; Duan, L.; Wen, F.; Li, C.; Wang, M.; Hagfeldt, A.; Sun, L. Visible Light Driven Hydrogen Production from a Photo-Active Cathode Based on a Molecular Catalyst and Organic Dye -Sensitized p-Type Nanostructured NiO. *Chem. Commun.* **2012**, *48* (7), 988–990. <https://doi.org/10.1039/C2CC16101J>.
- (135) Giannoudis, E.; Bold, S.; Müller, C.; Schwab, A.; Bruhnke, J.; Queyriaux, N.; Gablin, C.; Leonard, D.; Saint-Pierre, C.; Gasparutto, D.; Aldakov, D.; Kupfer, S.; Artero, V.; Dietzek, B.; Chavarot-Kerlidou, M. Hydrogen Production at a NiO Photocathode Based on a Ruthenium Dye–Cobalt Diimine Dioxime Catalyst Assembly: Insights from Advanced Spectroscopy and Post-Operando Characterization. *ACS Appl. Mater. Interfaces* **2021**, *13* (42), 49802–49815. <https://doi.org/10.1021/acsami.1c12138>.
- (136) Cai, B.; Wrede, S.; Wang, S.; Kloo, L.; Boschloo, G.; Tian, H. An Indacenodithieno[3,2-b]Thiophene-Based Organic Dye for P-Type Dye-Sensitized Solar Cells and Photoelectrochemical H₂O₂ Production. *ChemPhotoChem* *n/a* (n/a), e202300297. <https://doi.org/10.1002/cptc.202300297>.
- (137) Kemppainen, E.; Bodin, A.; Sebok, B.; Pedersen, T.; Seger, B.; Mei, B.; Bae, D.; K. Vesborg, P. C.; Halme, J.; Hansen, O.; D. Lund, P.; Chorkendorff, I. Scalability and Feasibility of Photoelectrochemical H₂ Evolution: The Ultimate Limit of Pt Nanoparticle as an HER Catalyst. *Energy Environ. Sci.* **2015**, *8* (10), 2991–2999. <https://doi.org/10.1039/C5EE02188J>.
- (138) Chen, X.; Zheng, X.; Qi, L.; Xue, Y.; Li, Y. Conversion of Interfacial Chemical Bonds for Inducing Efficient Photoelectrocatalytic Water Splitting. *ACS Mater. Au* **2022**, *2* (3), 321–329. <https://doi.org/10.1021/acsmaterialsau.1c00071>.
- (139) Kawawaki, T.; Negishi, Y.; Kawasaki, H. Photo/Electrocatalysis and Photosensitization Using Metal Nanoclusters for Green Energy and Medical Applications. *Nanoscale Adv.* **2020**, *2* (1), 17–36. <https://doi.org/10.1039/C9NA00583H>.

- (140) Lin, T.; Xu, R.; Hu, Y.; Wang, J.; Liu, Y.; Zhou, W. The Electrocatalytic HER Activity of MoS₂ Decorated with Adjustable-Size Ruthenium Nanoparticles. *Int. J. Hydrog. Energy* **2024**, *68*, 688–695. <https://doi.org/10.1016/j.ijhydene.2024.04.311>.
- (141) Wang, D.; Zhang, X.; Shen, Y.; Wu, Z. Ni-Doped MoS₂ Nanoparticles as Highly Active Hydrogen Evolution Electrocatalysts. *RSC Adv.* **2016**, *6* (20), 16656–16661. <https://doi.org/10.1039/C6RA02610A>.
- (142) Jaramillo, T. F.; Jørgensen, K. P.; Bonde, J.; Nielsen, J. H.; Horch, S.; Chorkendorff, I. Identification of Active Edge Sites for Electrochemical H₂ Evolution from MoS₂ Nanocatalysts. *Science* **2007**, *317* (5834), 100–102. <https://doi.org/10.1126/science.1141483>.
- (143) Huang, Z.; Luo, W.; Ma, L.; Yu, M.; Ren, X.; He, M.; Polen, S.; Click, K.; Garrett, B.; Lu, J.; Amine, K.; Hadad, C.; Chen, W.; Asthagiri, A.; Wu, Y. Dimeric [Mo₂S₁₂]²⁻ Cluster: A Molecular Analogue of MoS₂ Edges for Superior Hydrogen-Evolution Electrocatalysis. *Angew. Chem. Int. Ed.* **2015**, *54* (50), 15181–15185. <https://doi.org/10.1002/anie.201507529>.
- (144) Du, K.; Zheng, L.; Wang, T.; Zhuo, J.; Zhu, Z.; Shao, Y.; Li, M. Electrodeposited Mo₃S₁₃ Films from (NH₄)₂Mo₃S₁₃·2H₂O for Electrocatalysis of Hydrogen Evolution Reaction. *ACS Appl. Mater. Interfaces* **2017**, *9* (22), 18675–18681. <https://doi.org/10.1021/acsami.7b01333>.
- (145) Gu, J.; He, J.; Zheng, H.; Sun, C. Morphology Control in the Synthesis of [Mo₃S₁₃]²⁻/Co-MOF-74 Composite Catalysts and Their Application in the Oxygen Evolution Reaction. *New J. Chem.* **2023**, *47* (18), 8507–8514. <https://doi.org/10.1039/D3NJ00887H>.
- (146) Polypyrrole-Ru(2,2'-bipyridine)₃²⁺/MoS_x Structured Composite Film As a Photocathode for the Hydrogen Evolution Reaction | *ACS Applied Materials & Interfaces*. <https://pubs.acs.org/doi/full/10.1021/acsami.5b00401> (accessed 2023-05-02).

Appendix

Chemical Formula	Name	CAS number	Purity (%)	Brand
$C_{12}H_{28}O_4Ti$	Titanium tetraisopropoxide	546-68-9	97 %	Sigma Aldrich
$C_{14}H_{10}O_4$	Biphenyl-4,4'-dicarboxylic acid	787-70-2	0.98 %	abcr GMBH
$C_{12}H_8N_2O_4$	2,2'-Bipyridine-5,5'-dicarboxylic acid	1802-30-8	98%	Tokyo chemical industries
$C_8H_6O_4$	Terephthalic acid	100-21-0	>99%	Fluka Chamika
CH_4O	Methanol	67-56-1	HPLC-grade	VWR Chemicals
C_3H_7NO	Dimethylformamide	68-12-2	0.998 %	Thermo scientific
$C_{16}H_{18}ClN_3S$	Methylene blue	61-73-4		Merck
TiO_2	Titanium(IV) Oxide anatase	13463-67-7	0.997 %	Sigma aldrich
$C_6H_4O_2$	1,4-Benzuquinone	106-51-4	0.99 %	Acros Organics
C_3H_8O	Isopropanol	67-63-0		Donauchem
$C_6H_{15}NO_3$	Triethanolamine	102-71-6	0.98 %	Sigma Aldrich
$C_{14}H_{14}N_3NaO_3S$	Methyl orange	547-58-0		
$NaOH$	Sodium hydroxide	1310-73-2	unknown	Carl Roth GMBH
$CHCl_3$	Chloroform	67-66-3	>99.0 %	Loba Feinchemie
$C_2H_4O_2$	Acetic Acid	64-19-7 98	100 %	Fisher scientific UK limited
$AgNO_3$	Silver nitrate		99.9%	abcr
$C_{12}H_{10}Se_2$	Diphenyl diselenide	1666-13-3	99%	Acros Organics
$C_{12}H_{10}S_2$	Diphenyl disulphide	882-33-7	99%	Acros Organics
$C_{12}H_{10}Te_2$	Diphenyl ditelluride	32294-60-3	99%	Sigma Aldrich
$C_{30}H_{24}F_{12}N_6P_2Ru$	Tris(2,2'-bipyridine) ruthenium(II) hexafluorophosphate	60804-74-2	99%	Merck
$(NH_4)_2S_x$	ammonium sulphide solution (20 wt% in water)	12135-76-1	20%	Sigma Aldrich
$((NH_4)_6[Mo_7O_{24}]\cdot 4H_2O)$	ammonium molybdate tetrahydrate	12054-85-2	99.8%	Sigma Aldrich
$NH_2OH\cdot HCl$	hydroxylamine hydrochloride	5470-11-1	98%	Sigma Aldrich

Chemical Formula	Name	CAS number	Purity (%)	Brand
C_8H_8	Styrene	100-42-5	99%	Merck
$[CH_3CH(O)CO_2NH_4]_2Ti(OH)_2$	Titanium(IV) bis(ammonium lactate) dihydroxide solution	65104-06-5	50% in water	Sigma Aldrich
$C_6H_6O_2$	Resorcinol	108-46-3	-	-
$NiCl_2$	Nickel chloride	7718-54-9	99%	Merck

List of publications

Publications

- 14 Stephen Nagaraju Myakala, Magdalena Ladisich, Pablo Ayala, Hannah Rabl, Samar Batool, Michael S. Elsaesser, Alexey Cherevan, Dominik Eder,
Harnessing a Ti-based MOF for selective adsorption and visible-light-driven water remediation, *JMCA*, **12**, **2024**,
Contributions - Main Lead - Formulating the idea, experiments and writing
- 13 Naduvile Purayil Dileep, Mithun C Madhusudhanan, Lakshmi K. Puthenveetil, Vipin Yadav, Stephen Nagaraju Myakala, Sooraj Kunnikuruvanc,d, and M. M. Shaijumon,
Nanostructured Ternary Bismuth-Antimony Trichalcogenide/Au heterostructure Boosts Electrocatalytic Hydrogen Evolution Reaction, *ACS Applied Energy Materials*, **2024**,
Contributions - Development of synthetic procedure
- 12 Stephen Nagaraju Myakala, Hannah Rabl, Jasmin S. Schubert, Samar Batool, Pablo Ayala, Dogukan H. Apaydin, Alexey Cherevan, Dominik Eder,
MOCHAs: An Emerging Class of Materials for Photocatalytic H₂ Production, *SMALL*, **2024**,
Contributions - Main Lead - Formulating the idea, experiments and writing
- 11 Sujana Chandrappa, Stephen Nagaraju Myakala, Namitha Anna Koshi, Simon Joyson Galbao, Seung-Cheol Lee, Satadeep Bhattacharjee, Dominik Eder, Alexey Cherevan, and Dharmapura H. K. Murthy,
Unveiling Valence State-Dependent Photocatalytic Water Splitting Activity and Photocathodic Behavior in Visible Light-Active Iridium-Doped BaTiO₃, *ACS Applied Materials Today*, **27**, **2024**,
Contributions - Development of synthetic procedure and electrocatalytic measurements
- 10 Samar Batool, Marcel Langer, Stephen Nagaraju Myakala, Magdalena Heiland, Dominik Eder, Carsten Streb, Alexey Cherevan,
Thiomolybdate clusters: from homogeneous catalysis to heterogenization and active sites, *Advanced Materials*, **2024**,
Contributions - Summarizing works on the electrocatalytic studies on thiomolybdates
- 09 Jasmin S. Schubert, Eva Doloszeski, Pablo Ayala, Stephen Nagaraju Myakala, Jakob Rath, Bernhard Fickl, Ariane Giesriegl, Dogukan H. Apaydin, Bernhard C. Bayer, Shun Kashiwaya, Alexey Cherevan, Dominik Eder,
Nature of the Active Ni State for Photocatalytic Hydrogen Generation, *Advanced Materials Interfaces*, **2023**,
Contributions - Development of photocatalytic setup and stability measurements
- 08 Pablo Ayala, Shaghayegh Naghdi, Sreejith P. Nandan, Stephen Nagaraju Myakala, Jakob Rath, Hikaru Saito, Lakhani Lal, Maytal Caspary Toroker, Patrick Guggenbergerd, Freddy Kleitz, Alexey Cherevan, Dominik Eder,
The Emergence of 2D Building Units in Metal-Organic Frameworks for Photocatalytic Hydrogen Evolution: a Case Study with COK-47, *Advanced Energy Materials*, **2023**,
Contributions - Development of synthetic procedure and photocatalytic measurements
- 07 Sujana Chandrappa, Simon Joyson Galbao, P. S. Sankara Rama Krishnan, Namitha Anna Koshi, Sreewashi Das, Stephen Nagaraju Myakala, Seung-Cheol Lee, Arnab Dutta, Alexey Cherevan, Satadeep Bhattacharjee and Dharmapura H. K. Murthy,
Iridium-doping as a strategy to realize visible light absorption and p-type behavior in BaTiO₃, *The Journal of Physical Chemistry C*, **2023**,
Contributions - Photocatalytic investigations

- 06 Hannah Rabl, Stephen Nagaraju Myakala, Jakob Rath, Bernhard Fickl, Jasmin S. Schubert, Dogukan H. Apaydin, Dominik Eder, **Microwave-assisted synthesis of metal-organic chalcogenolate assemblies as electrocatalysts for syngas production**, *Communications Chemistry* 6, 43, **2023**, *Contributions - Development of synthetic procedure*
- 05 Stephen Nagaraju Myakala, Jorge Torres-Rodríguez, Miralem Salihovic, Maurizio Musso, Nicola Hüsing, Dominik Eder, Volker Presser, Alexey Cherevan, Michael S. Elsaesser, **Titania hybrid carbon spherogels for photocatalytic hydrogen evolution**, *Carbon* 202, 487, **2023**, *Contributions - Photocatalytic measurements and Post catalytic analytics*
- 04 Naduvile Purayil Dileep, Lakshmi Kollenchery Puthenveetil, Stephen Nagaraju Myakala, Manikoth M. Shaijumon, **Electrophoretically-deposited BiSbSe₃ nanoparticles as highly efficient electrocatalysts for hydrogen evolution reaction**, *Applied Materials Today*, 27, **2022**, *Contributions - Development of synthetic procedure and electrocatalytic measurements*
- 03 Samar Batool, Sreejith P. Nandan, Stephen Nagaraju Myakala, Ashwene Rajagopal, Jasmin S. Schubert, Pablo Ayala, Shaghayegh Naghdi, Hikaru Saito, Johannes Bernardi, Carsten Streb, Alexey Cherevan, and Dominik Eder, **Surface Anchoring and Active Sites of [Mo₃S₁₃]²⁻ Clusters as Co-Catalysts for Photocatalytic Hydrogen Evolution**, *ACS Catalysis*, 12, **2022**, *Contributions - Various characterizations, Photocatalytic measurements and post-catalytic analysis*
- 02 Pablo Ayala, Ariane Giesriegl, Sreejith P. Nandan, Stephen Nagaraju Myakala, Peter Wobrauschek, Alexey Cherevan, **Isolation Strategy towards Earth-Abundant Single-Site Co-Catalysts for Photocatalytic Hydrogen Evolution Reaction**, *Catalysts*, 11, **2021**, *Contributions - Characterization and results analysis*
- 01 Anto James, Chris John, Cheriya cheruvakkara Owais, Stephen Nagaraju Myakala, Sarap ChandraShekar, Jyoti Roy Choudhuri, Rotti Srinivasamurthy Swathi, **Graphynes: indispensable nanoporous architectures in carbon flatland**, *RSC Advances*, 8, **2018**, *Contributions - Literature collection and writing an overview on the synthesis of graphynes*
- Journal Cover Designs
- 10 **Front cover**, Harnessing a Ti-based MOF for selective adsorption and visible-light-driven water remediation, *J. Mater. Chem. A*, **2024**
- 09 **Front cover**, Nature of the Active Ni State for Photocatalytic Hydrogen Generation, *Adv. Mater. Interfaces*, **2024**
- 08 **Front cover**, A thiomolybdate cluster for visible-light-driven hydrogen evolution: comparison of homogeneous and heterogeneous approaches, *Sus. Ener. Fuels*, **2024**
- 07 **Front cover**, Thiomolybdate Clusters: From Homogeneous Catalysis to Heterogenization and Active Sites, *Adv. Mat.*, **2024**
- 06 **Front cover**, Engineering Configuration Compatibility and Electronic Structure in Axially Assembled Metal–Organic Framework Nanowires for High-Performance Lithium Sulfur Batteries, *ACS Energy letters*, **2023**
- 05 **Back cover**, CdS-TiO₂ nanostructures synthesized via the SILAR method for enhanced photocatalytic glucose conversion and simultaneous hydrogen production under UV and simulated solar irradiation, *Catal. Sci. Technol.*, **2023**
- 04 **Back cover**, The Emergence of 2D Building Units in Metal-Organic Frameworks for Photocatalytic Hydrogen Evolution: A Case Study with COK-47, *Adv. Energy Mater.* **2023**
- 03 **Front cover (inside)**, Ni₁₂ tetracubane cores with slow relaxation of magnetization and efficient charge utilization for photocatalytic hydrogen evolution, *J. Mater. Chem. C*, **2022**
- 02 **Front cover**, Immobilization of a [Co^{III}Co^{II}(H₂O)W₁₁O₃₉]⁷⁻ Polyoxoanion for the Photocatalytic Oxygen Evolution Reaction, *ACS Mater. Au*, **2022**
- 01 **Front cover**, Surface Anchoring and Active Sites of [Mo₃S₁₃]²⁻ Clusters as Co-Catalysts for Photocatalytic Hydrogen Evolution, *ACS Catalysis*, **2022**

Curriculum vitae

Stephen Nagaraju Myakala

Curriculum Vitae

Technical University of Vienna, TU Wien

Date of Birth - 23.08.1996

✉ stephen.myakala@gmail.com

Research Interests

My initial research during MSc. focussed on the synthesis and exfoliation of binary and ternary semi-metal chalcogenides (BiSbSe_3 , Bi_2Se_3) for electrocatalytic CO_2RR , later I expanded my work to solvothermal and microwave-assisted synthesis of thin films and nanomaterials (Metal-organic-frameworks (MOFs), Metal-organic-chalcogenolates (MOCHAs)). Building on this foundation, I am currently working on testing these hybrid materials (MOCHAs, MOFs) and hybrid architectures (molecular catalysts (MoS_x) anchored on NiO-organic-dye-sensitized substrates) to explore their potential for electro- and photo-catalytic energy and environmental applications such as solar fuel generation.

Education

- 2020–2024 Research assistant (PhD. student), Technical University of Vienna
- 2019–2020 Research assistant, IISER, Thiruvananthapuram
- 2014–2019 Integrated Bachelor and master (BS-MS) Program, Indian Institute of Science Education and Research, Thiruvananthapuram, *IISER-TVM*
Major - PHYSICS, Minor - CHEMISTRY
Overall GPA: 7.34/10.0

Research Experience

Doctoral Thesis

- Title **Design and study of organic-inorganic hybrids as photocatalysts for energy and environmental applications**
- Supervisor Asst.Prof. Alexey Cherevan, Prof. Dominik Eder, *Institute of Materials Chemistry*, TU Wien
- Duration June 2020– Current

Master Thesis

- Title **Electro-chemical Exfoliation of Semi-metals and probing their performance for the carbondioxide reduction reaction**
- Supervisor Assoc.Prof. M. M. Shaijumon, *School of Physics*, IISER Thiruvananthapuram, India
- Duration June 2018– April 2019

Research Collaborations & Internships

- Title **Mo_3S_{13} sensitized photocathodes for efficient visible light H_2 production**
- Supervisor Dr. Vincent Artero and Dr. Murielle Chavarot, *CEA*, Grenoble, France
- Title **Study of facet dependent deposition of novel MXenes for photocatalytic hydrogen evolution reaction**
- Supervisor Asst. Prof. Dr. Shun Kashiwaya, *Linköping University*, Sweden

- Title **Investigating the photocatalytic performance of Pt/Zn intermetallics for H₂ production**
 Supervisor Prof. Dr. Klaus Richter, Linköping University, Sweden
- Title **Iridium doped BaTiO₃ for visible photocatalytic hydrogen evolution reaction**
 Supervisor Assoc. Prof. Dr. Murthy Dharmapura, Manipal Institute of Technology, India
- Title **Detail study of graphitic carbon nitride (g-C₃N₄) photocatalysts for visible light driven hydrogen evolution reaction**
 Supervisor Assoc. Prof. Dr. Murthy Dharmapura, Manipal Institute of Technology, India
- Title **Electrochemical synthesis of Ni₂P for the oxygen evolution reaction**
 Supervisor Assoc. Prof. Dr. M M Shaijumon, *School of Physics, IISER Thiruvananthapuram, India*

Awards and Fellowships

- 2023 **Chemical Monthly Fellowship**, by Vienna and the Austrian Chemical Society (GÖCH)
 10,000 euros
- 2023 **Best Poster Award at EUROMOF23**, by Royal Society of Chemistry (RSC)
 150 euros
- 2022 **International Communication funding program**, by Austrian Research Foundation(ÖFG)
 1800 euros
- 2022 **Christiana Hörbiger Prize**, by TU Wien
 2400 euros
- 2020 **FWF Project funding** - Selected for a 4-year fully-funded PhD position according to the stand-alone FWF project N32801-N, by TU Wien
 40k euros/yr
- 2014 **Innovation in Science Pursuit for Inspired Research (INSPIRE) scholarship**, Second highest undergraduate fellowship awarded in India in Science and Technology
 3750 euros - 5 yr

Conferences and Seminars

- 2024 **8th Annual Nanotechnology Conference (NANOMAT2024)**, August 25-28, Vienna, *Austria*
- 2024 **18th International Congress on Catalysis (ICC2024)**, July 14-17, Lyon, *France*
- 2023 **5th European Conference on Metal Organic Frameworks and Porous Polymers (EUROMOF2023)**, Sept. 24-27, Granada, *Spain*
- 2023 **8th International Conference on Semiconductor Photochemistry (SP8)**, Sept. 11-15, Strasbourg, *France*
- 2022 **23th International Conference on Photochemical Conversion and Storage of Solar Energy (IPS23 - Poster)**, Aug. 02 - 05, Lausanne, *Switzerland*
- 2022 **44th International Conference on Co-ordination Chemistry (ICCC2022)**- Poster presentation, Aug 28 - Sept 02, Rimini, *Italy*
- 2021 **European Congress and Exhibition on Advanced Materials and Processes (EUROMAT2021)** - (Online - Sept. 13 - 17), Graz, *Austria*
- 2021 **CataLight Young Scientist Symposium (CYSS2021)**- Poster presentation (Online - Sept. 21-30), *Austria*
- 2019 **International Workshop on Advances in 2D Materials (IW2DM)**, July 22-23, *India*

Research skills

Instrumentation	Scanning Electron Microscope(SEM) with EDAX analysis, Bragg brentano and grazing incidence X-ray Diffraction, UV-Vis Spectrophotometer, Thermogravimetric analysis, Gas chromatography(GC-Nexis 2030), Attenuated Total Reflectance-Fourier Transform Infrared Spectroscopy(ATR-FTIR)
Softwares	Gaussian computing software, HTML, MS Office,Python, C++, Origin, ImageJ, Chem-Draw, Origin, Adobe Illustrator, Blender - Scientific Illustrations
Math Packages	Mathematica, Matlab

Acknowledgements

First and foremost, I would like to thank Asst.Prof. Alexey Cherevan and Prof. Dominik Eder for their immense support and guidance throughout the 4+ years. I am extremely grateful for selecting me based on my potential and placing their faith in my work. I am also thankful for providing me with all the necessary resources and more importantly their time that helped me to grow as a researcher. Lastly, I would also like to thank them for building a diverse and supportive team of researchers and colleagues, ready to always help. I am grateful to TU Wien for building an excellent research institution providing diverse opportunities for students.

I would like to specially thank Jakob Blaschke, Hannah Rabl, and Adrian Ertl, who reviewed and proofread my thesis providing valuable feedback and comments improving the overall quality in the presentation of the work. I would like to thank all the members of the group who helped me with their time and efforts to measure all the different characterization techniques and experiments.

A heartfelt thanks to my office colleagues, both old and new, for always providing a fun and relaxed environment. I am grateful to Dr. Ariane G. and Dr. Paolo R. for helping me get started during the initial period, in the group. My gratitude specially extends to Maddie W, Adrian E., Pablo A, Hannah R, Jakob B, Dr. Dogukan A, Dr. Jasmin S., Dr. Sreejith P, and Dr. Samar Batool for making the rest of my PhD an amazing journey. I am very grateful for the excellent secretaries of the group, who have often gone the extra mile to provide help. I would also like to thank other members of the group who constantly supported me when I needed their help.

I would like to thank all my collaborators, Pablo Ayala, Hannah Rabl, Dr. Michael Elsasser, Dr. Vincent Artero, Dr. Murielle Chavarot and many more, for providing me with the opportunity and their expertise resulting in several of the publications mentioned before. I am extremely grateful of Dr. Vincent Artero and Dr. Murielle Chavarot for hosting me their research group. I have genuinely learned quite a lot from them and each of their lab members.

Lastly and most importantly, I would like to thank my parents for their constant support in all forms and means. I would not be here without their hard work and efforts to provide me with the best of education and opportunities.